Studies of hadronic decays of high transverse momentum W and Z bosons with the ATLAS detector at the LHC

Rebecca Thalatta Chislett
University College London

Submitted to University College London in fulfilment
of the requirements for the award of the
degree of **Doctor of Philosophy**

August 21, 2014

Declaration

I, Rebecca Thalatta Chislett confirm that the work presented in this thesis is my own. Where information has been derived from other sources, I confirm that this has been indicated in the thesis.

Rebecca Chislett _____

Abstract

This work is based on data recorded by the ATLAS experiment at the LHC in 2011 at a centre of mass energy of 7 TeV and in 2012 at 8 TeV. The work predominantly focusses on searches for hadronically decaying W and Z bosons in the high p_T regime such that both the decay products are contained within a single jet. Firstly, a selection using jet shapes boosted back into the centre of mass frame of the jet is used to locate a W and Z boson peak above the large QCD background in 2011 data and from this a cross section is extracted. This peak is then used to study a variety of grooming techniques designed to reduce the effects of pileup and leave only the components of jet related to the hard scatter. The effect of these techniques on a sample already containing strongly signal-like jets is assessed in terms of terms of data-Monte Carlo agreement, signal to background ratio and pileup dependence. They are found to perform well to a level that will be useful in future measurements at the LHC.

Secondly an analysis designed to search for heavy diboson resonances in the hadronic channel is described. This search is based on a optimised version of a splitting and filtering technique investigated in the W and Z boson analysis with some additional substructure cuts. The analysis is run on 2012 data and the preliminary results and limits are presented. An excess corresponding to about 3.4σ local significance is observed and this peak is currently undergoing a series of cross checks.

This thesis also contains some performance studies of the ATLAS forward jet trigger in 2011 in terms of efficiency plots and work

done to investigate applying calibration to the jet triggers. The calibration was seen to improve the jet trigger and was subsequently used in 2012 running.

Acknowledgements

I would like to thank everyone who has helped me over the past three and a half years. Firstly, I would like to thank my supervisor, Mario Campanelli, who has guided me through all the work I have done providing help when I needed it. During her two years at UCL, Pauline Bernat helped me endlessly, always being there and willing to help when I needed her, providing both emotional support and answering my many questions about physics and coding. And since she left I have Alex Martynuik to thank for working with me towards the search for heavy resonances, about which we have had many interesting and useful discussions.

I would also like to express my gratitude for everyone in the various analysis groups I have been part of, without whom this would not have been possible. In particular I would like to thank Francesco de Lorenzi for his invaluable contribution towards the boosted hadronically decaying W and Z boson cross section measurement. I would also like to thank Enrique Kajomovitz, who leads the search for heavy resonances and has been a joy to work with as well as the other member of the analysis group, Attilio Picazio, Lei Li, Angel Campoverde, Ayana Arce, Robert McCarthy and Chris Malena Delitzsch. I also cannot forget the work of David Adams who initially started the search.

Thank you also to all my friends who are so important to me. I would like to thank all the friends I made at CERN for making my time there so enjoyable and my friends who have supported me since I have been back in the UK. Especially my flat mate Lizzie, for putting up with all my moaning and generally always being there for me. I would also like to thank everyone in the UCL HEP group for a fun few years. Lastly, I have to mention Mum, Dad and Sam who have been a great support to me always.

Contents

List of Figures

List of Tables

Chapter 1.

Introduction

The Standard Model of particle physics has thus far been very successful at describing a wide range of experimental data, hence increasingly more powerful and technologically advanced machines have been built to carry out precision tests of the theory and search for potential disagreements or evidence for new physics. The Large Hadron Collider (LHC) is currently the largest collider built to do this reaching the highest energies ever studied in an accelerator. It is designed to collide protons at a centre of mass energy of 14 TeV delivering luminosities up to $10^{34}\text{cm}^{-2}\text{s}^{-1}$.

This thesis will present work carried out using ATLAS, one of the detectors around the LHC ring, using data collected in 2011 at a centre of mass energy of 7 TeV and data collected in 2012 at a centre of mass energy of 8 TeV. The first chapters explain the necessary background information with a theoretical overview in Chapter 2, a description of the detector in Chapter 3 and a discussion of techniques used in data analysis in Chapter 4. The ATLAS trigger system is described in Chapter 5 followed by studies on the performance of the jet trigger in Chapter 6 and some work on improvements to the jet trigger in terms of applying calibration in Chapter 7. Following this an analysis looking for hadronically decaying W and Z bosons in the high p_T regime based on 2011 data is presented in Chapter 8, firstly obtaining a cross section measurement then looking at the application of jet grooming techniques and their effect on the signal and the background. Lastly an analysis searching for potential new physics in 2012 data by looking for heavy resonances decaying to W and Z bosons in the hadronic channel is presented in Chapter 9 which draws on similar techniques to those investigated in the analysis presented in Chapter 8.

As is the nature of working in a large collaboration the analysis work was done as part of a team and not solely by me. I have focussed mostly on my contributions to the analyses but at certain points it is necessary to describe work that was not carried out by myself. The work on the trigger efficiencies and the application of calibration to the trigger in Chapters 6 and 7 was done solely by me. In the study about boosted hadronically decaying W and Z bosons in Chapter 8 the main focus of my work was in the study of the various grooming techniques on the peak and in Chapter 9 I carried out the signal interpolation, background cross checks and calculated the systematics due to the parton shower. The plots that I have not made myself have been credited to the appropriate people.

Chapter 2.

Theoretical Framework

Our current understanding of the fundamental particles in the visible universe and how they interact is described by the Standard Model. Mathematically it is a Quantum Field Theory (QFT) based on an $SU(3) \times SU(2)_L \times U(1)$ gauge symmetry. The basis of the theory is that the fundamental particles can be represented by quantised fields which must obey a set of symmetries. This results in a Langrangian, which describes the behaviour of these fields and hence the interactions of the particles. The symmetries within the theory, by Noether's theorem, result in the conservation of various observable quantities, such as the electric charge.

The elementary particles described by the standard model consist of fermions, with half integer spin, and bosons, with integer spin, which are all considered to be point-like with no internal structure. The fermions form two groups, quarks, which carry colour charge and leptons, which don't. These are in turn are divided into three families each interacting in the same way. These are summarised in Table 2.1. Each of these particles has a corresponding antiparticle with the same mass but opposite charge.

The exchange of bosons between these fermions is used to describe three of the four fundamental forces - the strong, weak and electromagnetic interactions, but gravity is not included in the theory. The strong force, which binds the quarks into protons and neutrons, is mediated by gluons which arise from the $SU(3)$ gauge symmetry. This interaction is between particles with colour charge, hence affects quarks but not leptons. The remaining bosons - $W^{\pm}$, Z^0, which mediate the weak interaction and the photon, γ, for the electromagnetic interaction arise from the

	Particle		charge	spin	mass [GeV]
Quarks	up	u	$\frac{2}{3}$	$\frac{1}{2}$	0.003
	down	d	$-\frac{1}{3}$	$\frac{1}{2}$	0.006
	charm	c	$\frac{2}{3}$	$\frac{1}{2}$	1.3
	strange	s	$-\frac{1}{3}$	$\frac{1}{2}$	0.1
	top	t	$\frac{2}{3}$	$\frac{1}{2}$	173
	bottom	b	$-\frac{1}{3}$	$\frac{1}{2}$	4.2
Leptons	electron	e	-1	$\frac{1}{2}$	0.0005
	electron neutrino	ν_e	0	$\frac{1}{2}$	$< 2 \times 10^{-9}$
	muon	μ	-1	$\frac{1}{2}$	0.1
	muon neutrino	ν_μ	0	$\frac{1}{2}$	$< 1.7 \times 10^{-4}$
	tau	τ	-1	$\frac{1}{2}$	1.8
	tau neutrino	ν_τ	0	$\frac{1}{2}$	$< 1.55 \times 10^{-2}$
Bosons	photon	γ	0	1	0
	gluon	g	0	1	0
	weak bosons	$W^\pm$	± 1	1	80.4
		Z^0	0	1	91.2
	higgs boson	H^0	0	0	125.9

Table 2.1.: The elementary particles in the Standard Model

$SU(2)_L \times U(1)$ gauge symmetry. The electromagnetic force is responsible for the formation of atoms, holding electrons in place around the nucleus and the weak force explains decays, such as radioactive decays.

The Standard Model has been tested to high precision and thus far successfully describes the data, with the exception of neutrino masses, and was further confirmed by the discovery of the Higgs boson in 2012 [4, 5]. It does, however, have some flaws, most obviously that it does not include a description of gravity and also that it has many parameters which are not predicted, rather have been determined by experiment.

2.1. QCD

Quantum Chromodynamics (QCD) is the theory that governs the strong force in the Standard Model, which binds quarks into hadrons. It arises like the other forces from the requirement of local gauge invariance, in this case under rotations in colour space. Thus all particles which interact via the strong force carry colour charge. It is a non-Abelian SU(3) gauge theory which is governed by the Lagrangian

$$\mathcal{L}_{QCD} = -\frac{1}{4}F_a^{\mu\nu}F_{\mu\nu a} + \sum_{f=1}^{n_f}\bar{q}_f(i\gamma^\mu D_\mu - m_f)q_f \tag{2.1}$$

where the covariant derivative is defined as

$$D_\mu q_f = \partial_\mu q_f + ig_s G_{\mu a}\frac{1}{2}\lambda_a q_f \tag{2.2}$$

and the field strength tensor for the gluon field, $G_{\mu a}$, is

$$F_{\mu\nu a} = \partial_\mu G_{\nu a} - \partial_\nu G_{\mu a} - g_s f^{abc} G_{\mu b} G_{\nu c}$$

Here the q_f are the quarks with the sum over the flavours, up, down, strange, charm, bottom and top with their corresponding masses represented by m_f. The γ^μ are the Dirac γ matrices and, according to the Einstein summation convention, have repeated indices summed over. The λ_a are the Gell-Mann matrices which allow for the rotation in colour space. g_s is related to the strong coupling constant α_s by the relation $\alpha_s = g_s^2/4\pi^2$. Lastly, f^{abc} are the structure functions of the SU(3) colour group.

From this Lagrangian it can be seen that there are terms in which the gluon couples to quark-antiquark pairs, in an analagous way to the photon couplings in QED. However, here, due to the non abelian third term in the field strength tensor, there are also triplet and quartic gluon-gluon interactions. This is an important difference from QED, in which the photons have no charge and hence don't self-interact. In QCD the gluon carries colour charge (one colour unit and one anti-colour unit) and hence self-interacts. This leads to many more possible diagrams in QCD interactions and also leads to the concepts of colour confinement and asymptotic freedom.

2.2. Asymptotic Freedom and Renormalisation

When calculating particle interactions, diagrams at all orders must be summed over, resulting in a perturbation series in terms of the coupling as additional loop corrections are added. In a similar way a correction to the quark-gluon and gluon-gluon interactions can be obtained through diagrams such as those in Figure 2.1. However, in these loops the momentum is unconstrained and hence results in an infinite integral. This is known as an ultraviolet divergence and to cope with this an ultraviolet cutoff is introduced, Q_0, the scale at which QCD is no longer considered to be reliable. It is also necessary to introduce a renormalisation scale Q which is generally the scale of the interaction. These divergences are then absorbed into the definition of the parameters producing renormalised parameters, which can be done at all orders and hence finite predictions for physical quantites can be made.

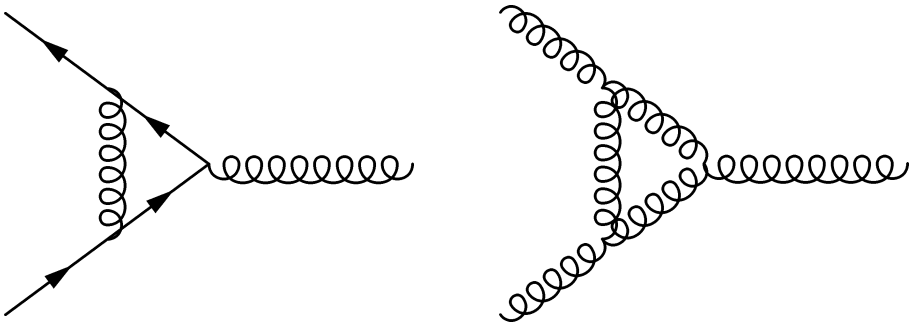

Figure 2.1.: Loop diagrams showing the modification to the gluon-gluon and quark-gluon interactions from higher order QCD terms

Absorbing these extra diagrams into the definition of the strong coupling constant results in it "running"; the value changes with the energy scale of the process. In the case of the strong coupling constant:

$$\alpha_{\mathrm{S}}\left(Q^2\right) \simeq \frac{\alpha_{\mathrm{S}}\left(Q_0^2\right)}{1 + B\alpha_{\mathrm{S}}\left(Q_0^2\right)\ln\left(\frac{Q^2}{Q_0^2}\right)} \tag{2.3}$$

where for N_c colours and N_f quark flavours, the constant, B, is given by

$$B = \frac{11N_c - 2N_f}{12\pi}$$

This results in α_s decreasing with increasing Q^2, the opposite of QED where the coupling increases as the energy scale increases. In QED, this can be understood

because vacuum polarisation will screen a charge as the distance from it is increased. In QCD the fact that the gluons are themselves charged and can self-interact produces a competing effect and actually results in the opposite observation of the strength increasing with distance. This leads to asymptotic freedom, where at very high energies or very short distances the strength of the colour field decreases and the quarks behave more like free fields. Analagously in QED a similar thing happens at low energies, or large distances. Hence for QED pertubation theory can be used in the low energy regime, whereas for QCD it is only valid in the high energy regime and so this must be used to test the theoretical predictions.

2.3. Colour Confinement

Another consequence of the running of the couplings is at low energies, where the strong coupling becomes very large. This increase means that the quarks and gluons cannot be observed in isolation, rather they must combine to form colourless hadrons. The gluon-gluon interactions that form part of QCD and aren't present in QED explain this.

In QCD virtual gluons can interact between the two separating quarks, which in effect forces the field lines closer together. So the cross sectional area containing the field lines remains roughly constant as the distance increases, as does the number of field lines, but the energy increases with the volume and hence an infinite amount of energy would be required to separate them. In fact, when the energy between two separating quarks is sufficient, a new pair of quarks is increasingly likely to be produced.

2.4. Factorisation and Parton Distribution Functions

The running of the coupling constant in QCD means that perturbation theory can only be used in the regime where the energy scale of a process is much larger than the scale of non-pertubative physics, $Q_0^2 \gg Q^2$ ($\sim$0.3 GeV). This makes analytic calculations of hadronic processes very difficult and hence the factorization theorem

is used. This separates a process into a perturbative coefficient function which is calculable, and a non-perturbative parton distribution determined from experiment, describing the structure of the proton. Expressed mathematically the cross section of a process is given by

$$\sigma(ep \to eX) = \sum_i C_i^P(x, \alpha_s(Q^2)) \otimes f_i(x, Q^2, \alpha_s(Q^2)) \tag{2.4}$$

where $C_i^P(x, \alpha_s(Q^2))$ represents the perturbative, calculable coefficient function, $f_i(x, Q^2, \alpha_s(Q^2))$ are the Parton Distribution Functions (PDFs) and the sum is over the partons in the interacting hadron. The PDFs represent the probability of finding a parton carrying a fraction x of the hadron's momentum. These are not process dependent but need to be measured by experiment. On the other hand the coefficient functions are characteristic of a given process and are calculable as a series in terms of the coupling constant.

A factorisation scale, μ_f must be chosen, such that below it the emissions are included as part of the PDFs and above it the emissions are included in the coefficient function calculation. In many cases this is chosen to be the same as the scale of the physics which is used as the renormalisation scale i.e. $\mu_f^2 = Q^2$.

In the absence of QCD scaling the PDFs are simply a function of x, but the effects of higher order QCD means that they also scale with Q^2. This can be explained as at higher energies, smaller distances are being probed and so the resolution of the proton is improved. Alternatively, there is more time for a quark or gluon to radiate and smaller x partons can be seen. This is observed as a dependence of the PDFs on the scale of the process being considered. Although the PDFs themselves cannot be calculated analytically and have to be measured, their evolution with x and Q^2 can be determined using splitting functions, formally written down in the DGLAP-equations [6–8]. This means that the PDFs can be measured in Deep Inelastic Scattering (DIS) experiments [9–11] and their subsequent evolution can be measured and compared to the theory.

2.5. Hadronisation and Jets

Colour confinement means that coloured quarks cannot be observed in isolation, they must be observed as part of a colourless hadron. This means that although coloured quarks can be produced in an interaction they will ultimately form themselves into hadrons.

As two coloured objects separate, the force between them increases and hence they are more likely to radiate and lose some energy. This means that a single quark produced in the hard scatter will result in a whole shower of partons, this part of the process being known as parton showering. As the energy of the shower falls the coloured partons group themselves into hadrons, known as hadronisation. This means a coloured parton produced in the hard interaction will be seen as a spray of hadrons.

In practice the resulting hadrons are detected, but the measurement of these individually is not very relevant. Usually they are combined into jets, ideally such that a jet contains all the hadrons arising from one parton. This means the jet can be used to investigate the hard process that produced it. In reality this is not exactly possible, but using a well defined jet algorithm allows for meaningful measurements to be performed which can be predicted theoretically, using Monte Carlo (MC) simulation.

2.6. Jet Algorithms

A jet algorithm is a set of rules used to combine objects into jets which approximate the partons that produced them. It needs to decide which objects should be included in the jet and how to combine their momenta in a useful and meaningful way. It is important that the data collected by a detector can be compared to MC predictions, so the algorithm should be able to run both using the final state particles produced in MC and the detectors object, such as the energy in calorimeter towers. A jet algorithm must also be infrared and collinear safe. Namely it must not be affected if a soft parton is added or if one parton is replaced by two partons very close in direction. These properties ensure that the jets are well-behaved theoretically, as if this is not the case calculations of physical quantities, above leading order, are

unstable. This also reflects the experimental limits in the resolution of the detector, where very soft or very collinear particles cannot be resolved.

The simplest form of jet algorithm that could be imagined is just to take a cone around a particle with a fixed radius, R chosen such that the energy contained in the cone is maximised. This is done iteratively, by taking a seed particle, combining the momenta of all the particles in a cone around it to define a new axis and repeating until the axis remains stable. This clearly means that the resulting jets can be dependent on the choice of seed. It also falls into difficultly when two cones overlap and a decision must be made whether to merge the jets or which particles should be assigned to each one. As a result cone algorithms are generally affected by additional soft emissions and hence are not infrared safe, with the exception of SIScone [12], the algorithm which accounts for all possible cones. It is because of this that, cone algorithms are not often used in analyses currently.

Successive recombination algorithms are the current preferred method of forming jets. These are based on attempting to work backwards through the branchings that occur in the parton shower by merging two particles together at each step. The particles that are chosen to be merged are those that are closest according to a distance measure defined as

$$d_{ij}^2 = min(p_{T_i}^{2p}, p_{T_j}^{2p})\frac{\Delta R_{ij}^2}{R^2}$$
$$d_{iB} = p_{T_i}^{2p}$$

where d_{ij} is the distance between two particles i and j and d_{iB} is the distance between a particle, i and the beam B and $\Delta R_{ij}^2 = (y_i - y_j)^2 + (\phi_i - \phi_j)^2$ and R is a parameter of the algorithm connected to the jet size. The distances, d_{ij} and d_{iB} are calculated for all particles. If one of the d_{ij} is smallest, the two particles i and j are merged by summing their four-momenta. If the distance d_{iB} is the closest distance then i is defined as a jet and removed from the clustering. The process is then repeated until all particles are merged into jets. Different values of p can be used, resulting in different algorithms.

The Cambridge-Aachen algorithm [13] uses $p = 0$ which results in the distance measure only having angular dependence. The lack of dependence on p_T generally produces irregularly shaped jets, but is useful when looking a the substructure of

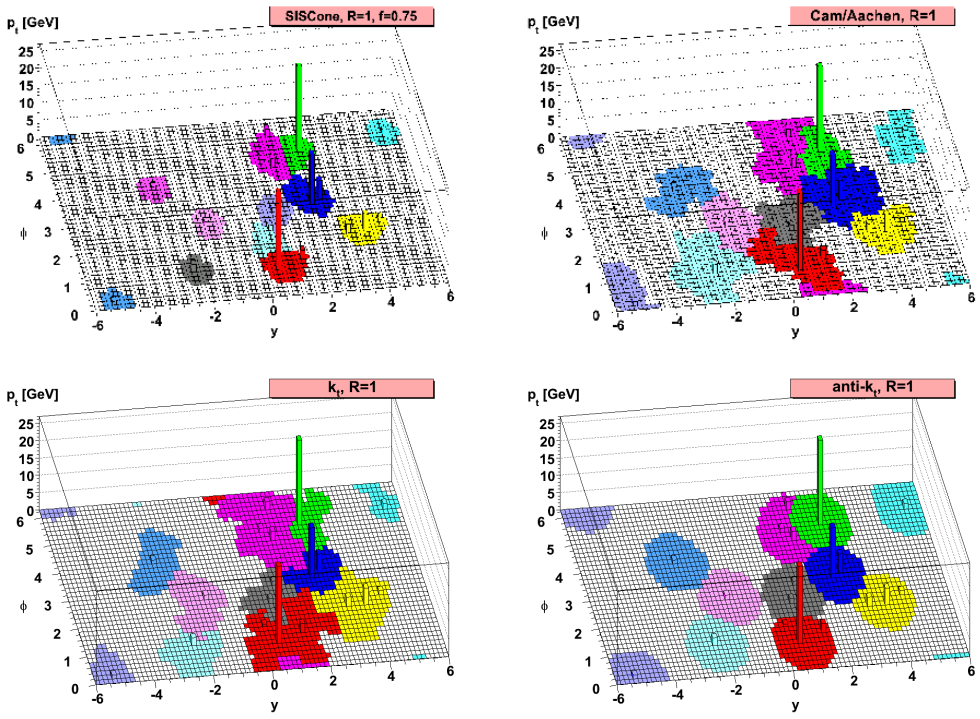

Figure 2.2.: The same events clustered using different jet clustering algorithms, SiSCone (top left), Cambridge-Aachen (top right), k_T (bottom left) and anti-k_T (bottom right) in η-ϕ space [1].

a jet, allowing studies on a range of angular scales based on the jet itself. The k_T algorithm [14] takes $p = 1$ which leads to the softer particles being clustered first and again results in irregularly shaped jets. This makes the jets harder to deal with in terms of trying to reduce the effects of pileup. Lastly, choosing $p = -1$ is known as the anti-k_T algorithm [1], which is the most commonly used in ATLAS. This tends to cluster lower p_T objects around a hard centre resulting in more circular jets.

The result of applying these different jet algorithms to cluster the same event in $\eta - \phi$ space is shown in Figure 2.2 for the Cambridge-Aachen, anti-k_T, k_T and SIScone algorithms. It can be seen in these that the four algorithms generally agree about the hardest jets, although combine different soft constituents into them. The p_T ordering of the smaller jets is slightly different between the different clusterings though. The circular nature of the anti-k_T algorithm is clear.

2.7. Electroweak Interactions

The dominant interactions at the LHC are described by QCD, but, as quarks can also participate in electroweak interactions, the electroweak sector is unavoidably involved, which is crucial for the studies later in this thesis. As for QCD it is governed by a Lagrangian, this time based on an $SU(2)_L \times U(1)$ gauge symmetry, which through electroweak symmetry breaking [15–17] describes the heavy $W^{\pm}$ and Z^0 bosons that govern the weak interaction and the massless photon from electromagnetism. The symmetry breaking also results in the prediction of the Higgs boson that was finally discovered in 2012.

Both quarks and leptons interact via the weak interaction and both $W^{\pm}$ and Z^0 bosons can be produced in the proton-proton collisions. As the weak force is governed by massive vector bosons, they have a short lifetime and hence the interaction is only short range. An example weak current interaction which could occur at the LHC is shown in Figure 2.3, in this case the vector bosons decay to quarks, the hadronic channel, as is most appropriate for the work done here. As charge is conserved the quarks produced in charged current interactions are of different types, such as $u\bar{d}$ and those in neutral current interactions are a quark and its antiquark, such as $u\bar{u}$.

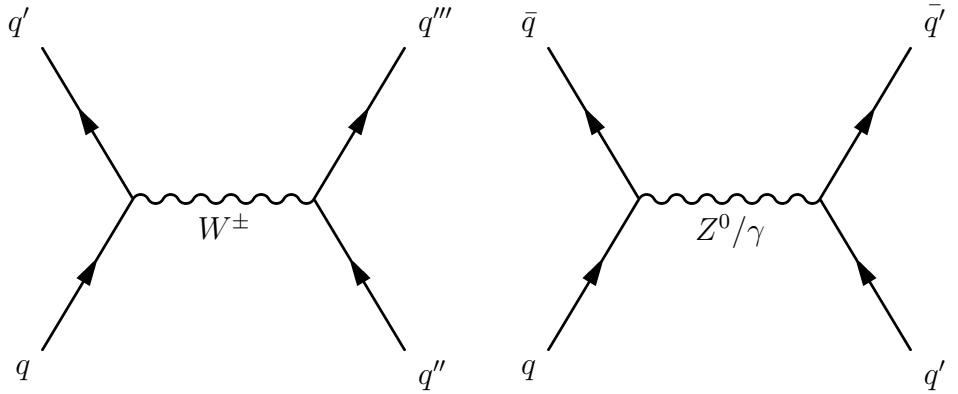

Figure 2.3.: Diagrams showing the modification to the gluon-gluon and quark-gluon interactions

2.8. Beyond the Standard Model

Despite its success, the Standard Model is unsatisfactory in many ways, such as gravity not being included, the many unpredicted parameters, that the couplings don't meet at high energies and its lack of an explanation for dark matter. At some point its predictions are no longer valid, as represented by the necessary inclusion of the renormalisation scale. As such, there are many possible theories for beyond the standard model physics and constant searches for new physics, both at the LHC and elsewhere.

Supersymmetry [18] offers one popular theory for physics beyond the standard model and searches at the LHC look for decay channels predicted by these processes. Another way to search for new physics processes is by looking for potential new high mass particles which interact in similar ways to the Standard Model. This can be done by looking for potential decay modes and reconstructing the invariant mass spectrum of these decay products. A new particle would appear as a bump in this spectrum. A simple example of a hypothesised new particle is a W' [19], which is essentially the same as a W boson but with a larger mass. The couplings are predicted to be the same, but are scaled by the mass, resulting in a weak interaction on an even shorter range.

2.9. Monte Carlo

Monte Carlo (MC) methods simulate physical processes using a computer algorithm based on random sampling leading to a numerical result. In the case of particle physics, these methods are used to simulate particle collisions based on theory such that the results can be compared to the data obtained. This is broadly composed of two main steps: event generation which predicts the particles produced in a process and detector simulation during which these particles are passed through a full simulation of the detector, including digitisation and reconstruction, producing an output that can be directly compared to the data.

The event generation is done by first calculating the hard process, based on the theoretical matrix elements. Final state and initial state radiation is added, and parton radiation produces the parton shower. Finally the partons are hadronised

and the decays of these are simulated. Lastly the remants of the proton and the underlying event is added. It is possible to simulate each of these steps using different codes, each one making use of a different matrix element, PDF set, parton shower model or hadronization model. For this reason it is helpful to compare the data to a variety of different MC simulations such that the various models can be tested and better understood.

The detector simulation is usually performed by GEANT [20], which simulates the interaction of the final hadrons predicted in the event generation with the material in the detector, such as ionisation in the trackers, the energy deposition in the calorimeters and the decays and radiation along the way. This outputs a result in the same form as the data so that the two can easily be compared.

The various MC generators used here are PYTHIA (versions 6 [21] and 8 [22, 23]), HERWIG [24], HERWIG++ [25] and POWHEG [26–28]. These generators and the differences between them will now be discussed.

2.9.1. PYTHIA

Both PYTHIA 6 and PYTHIA 8 use perturbative QCD at leading order to compute matrix elements for $2 \to 2$ processes. The parton shower is p_T ordered and interleaved with multiple interactions. Finally the hadronisation is done with the Lund string model. PYTHIA 8 is slightly more advanced than PYTHIA 6, developed in the C++ programming language which is now most commonly used for analysis. The main difference is that mulitple interactions are interleaved with both initial-state and final-state radiation in PYTHIA 8, whereas PYTHIA 6 doesn't include the final-state radiation. PYTHIA 8 also simulates more processes for the underlying event.

The non-perturbative physics processes, such as initial- and final-state radiation, hadronisation, the underlying event and colour connections, can be tuned to different data. The Perugia 2011 tune [29] is based on minimum bias and Drell Yan data from the Tevatron and Z^0 decays at LEP. The AMBT tunes adapt the tunes for the LHC developed using tevatron data by changing the parameters of the non diffractive models based on ATLAS minimum bias data at $\sqrt{s} = 900$ GeV and $\sqrt{s} = 7$ TeV. AMBT1 [30] uses the Martin-Roberts-Stirling-Thorne (MRST) LO* PDFs [31–33] and AMBT2B [34] uses MRST LO** PDFs [31–33], the main difference between

the two being the scaling of α_s is with p_T, rather than Q^2. Unless otherwise stated PYTHIA 8 uses the LO CTEQ6L1 [35] PDF set.

2.9.2. HERWIG

HERWIG also uses leading order matrix elements in perturbative QCD, but the parton shower in this case is angular ordered and then cluster hadronisation is used. For multiple parton interactions it is linked to JIMMY [36, 37]. The generator is also available in an updated form, HERWIG++, which is similar, except the multiple parton interactions are included, rather than having to link to JIMMY. HERWIG doesn't interleave the multiple parton interactions with the parton showers as PYTHIA does. As HERWIG and PYTHIA use very different parton shower and hadronisation models it is useful to compare the two. The differences are also useful in assessing systematic uncertainties.

2.9.3. POWHEG

POWHEG interfaces NLO calculations with a parton shower generator, such as PYTHIA or HERWIG. This essentially means that the emission of an additional hard parton is included in the matrix element calculation, rather than only occurring as part of the parton shower. As a result the modelling of a potential third jet in an event should be more accurate while keeping the flexibility to have more than three jets in the event which would not be possible with just an NLO calculation.

Chapter 3.

The ATLAS Detector

The Large Hadron Collider (LHC) [38] is a proton-proton collider, housed in a 27 km ring under France and Switzerland. It is the highest energy accelerator ever built, designed to run at centre of mass energies up to 14 TeV, reaching a luminosity of over $10^{34}\text{cm}^{-2}\text{s}^{-1}$. This intense environment requires a detector which is both robust and precise, such that it can withstand the high radiation doses as well as distinguish and measure the large numbers of particles, both in terms of position and energy.

3.1. The LHC

The protons, produced from hydrogen gas, are passed through a series of accelerators, each one boosting the energy and then passing the protons on to the next machine. The first accelerator is Linac 2, a linear accelerator which increases the energy to 50 MeV. The beam is then passes to the Proton Synchrotron Booster (PSB), which accelerates the protons to 1.4 GeV. They reach energies of 25 GeV in the Proton Synchrotron and then finally are passed to the Super Proton Synchrotron (SPS) which gets the beam to 450 GeV before it enters the LHC ring. This is demonstrated in Figure 3.1.

Two beams enter the LHC going in opposite directions around the ring, the energy is gradually increased during each rotation until the desired energy is reached. They are then forced to collide at the interaction points, where the detectors are placed, by quadrupole magnets. There are 4 large detectors around the ring, two general purpose detectors, ATLAS (A Torroidal LHC ApparatuS) and CMS (Compact Muon

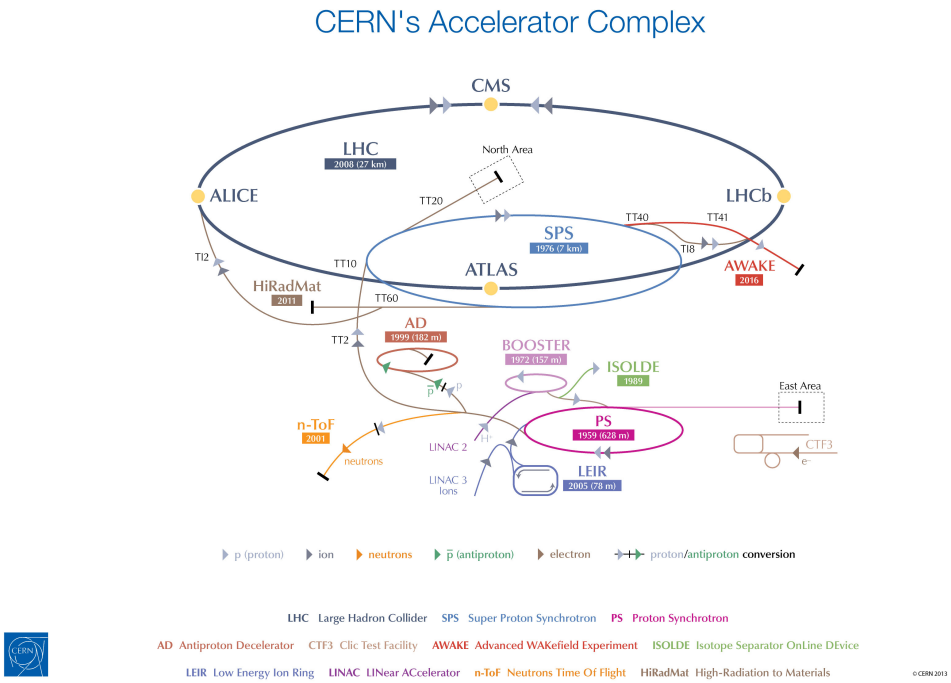

Figure 3.1.: The CERN accelerator complex [2]

Solonoid), LHCb which is a very forward detector focussing on b-quark physics, and ALICE which focusses on heavy ion physics.

3.2. The ATLAS Detector

The ATLAS detector [3] is an all-purpose detector, aiming for complete coverage and to identify all the particles produced in a collision. The interactions of interest occur over very short distances in very short time scales and hence cannot be measured directly. However, the stable particles produced can be and they act as a probe to measure the interaction that took place. This involves measuring the type of particle produced, its position and momentum. The detector was designed with interesting processes in mind, focussing on obtaining the best resolution while using radiation hard materials and electronics and allowing for distinction between various particles. As the particles interact in different ways the detector is formed of concentric layers, each focussed on identifying different types of particles. The detector layout is shown in Figure 3.2.

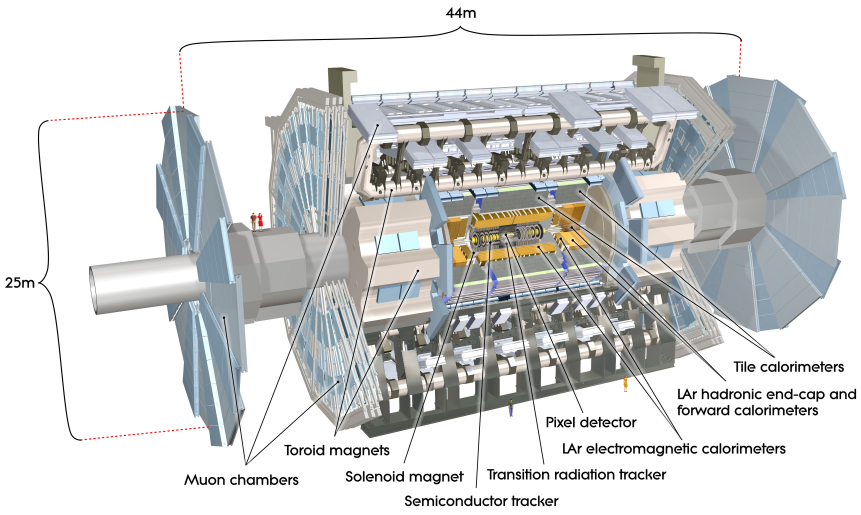

Figure 3.2.: The ATLAS detector [3]

Closest to the beam line is the inner tracking detector, contained within a thin superconducting solenoid magnet producing a 2T field. Charged particles passing through create hits in the detectors allowing the particles to be tracked and from the curvature of the path a momentum measurement made. This is also used to identify interaction vertices as well as allow longer lived particles to be identified by a displaced vertex. Outside this, the calorimeters measure the energy of both charged and neutral particles, the showers from electrons and photons in the electromagnetic calorimeter and those from hadrons in the hadronic calorimeter. Muons can pass relatively unimpeeded through all these layers of the detector and so the calorimeters are surrounded by the muon chambers. Toroidal magnets outside the calorimeters cause the muons to bend as they pass through allowing for an accurate momentum measurement to be made.

The detectors can be described using cartesian coordinates, such that the z axis is the beam line, the x axis points towards the centre of the ring and the y axis points upwards. The polar and azimuthal angles are denoted by θ and ϕ respectively and are defined with respect to the beam axis. It is useful to define quantities invariant with respect to a Lorentz boost along the z axis to describe events, as the detector frame is not necessarily the same as the centre of mass frame of the interacting partons. The rapidity difference is one such quantity, a Lorentz invariant angular

measurement, where rapidity is defined as

$$y = \frac{1}{2} \ln \frac{E + p_z}{E - p_z} \tag{3.1}$$

Particles are produced roughly constantly in rapidity. In the case of massless particles this simplifies to the pseudorapidity

$$\eta = -\ln \left(\tan \frac{\theta}{2} \right) = \frac{1}{2} \ln \frac{p + p_z}{p - p_z} \tag{3.2}$$

which is a simple function of the polar angle and is a good approximation to the rapidity for high energies. A useful momentum measurement is the transverse momentum, p_T, defined as

$$p_T = \sqrt{p_x^2 + p_y^2} \tag{3.3}$$

The interacting particles are travelling along the beam line so initially have very little transverse momentum, hence a large p_T indicates a significant interaction took place.

3.2.1. The Inner Detector

The Inner Detector, as shown in Figure 3.3 is comprised of three tracking detectors which measure hits of charged particles as they pass through, these are then combined to form particle tracks. It is immersed in a 2T magnetic field from the surrounding solenoid magnets and hence provides a momentum measurement of the particles from their curvature. It is also important for the identification of primary and secondary interaction vertices and so is used to identify longer lived particles such as b hadrons. The detector provides full azimuthal coverage and reaches up to $|\eta| < 2.5$. It reaches about 7m in z and 1.15m radially.

The innermost tracking uses silicon detectors, with the pixel detector closest to the beam which is arranged in 3 concentric cylinders around the beam line with 6 discs at the ends. The pixel detector provides high granularity in most intense region very close to the beam line. The large number of channels reduces the hit rate per channel (compared to strip detectors for example) which allows for a fast readout. The pixels are segmented in R-ϕ and z in the cyclinders, with a size of 10μm (R-ϕ)

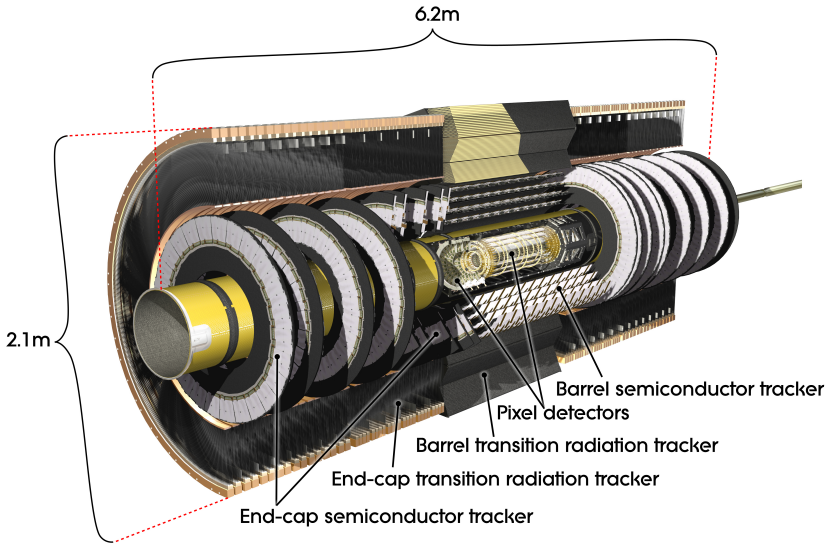

Figure 3.3.: The ATLAS inner detector [3]

x 115μm (z) and in R-ϕ and R in the discs, with a size of 10μm (R-ϕ) x 115μm (R), resulting in about 80.4 million readout channels. The whole pixel detector is contained within a distance of 65 cm in z and 24 cm radially. Most particles will pass through three pixel layers.

The Semiconductor Tracker (SCT) is a silicon strip detector with the strips aligned with the beams axis in cylinders around it and aligned radially in the end disks. It consists of two 6.4 cm long strips daisy chained together with a pitch of about 80 μm. To improve the accuracy of the position measurement the strips are arranged in pairs with layers tilted at an angle of 40 mrad. This results in an accuracy of 17 μm in R-ϕ and 580 μm in z. There are 4 layers of these pairs in the barrel and 9 disks at each end, with a size of about 3m in z and 0.5m radially.

The final layer of the tracker is the Transition Radiation Tracker (TRT), which consists of straw drift tubes aligned with the beam axis in the barrel and in a fan at the ends. The tubes are about 4mm in diameter, filled with a Xe-CO_2-O_2 gas mixture which is ionised when a charged particle passes through. The negative electrons drift to the wire running down the centre of each tube, producing a current. The accurate timing measurement of the pulses leads to a precision of about 130μm in R-ϕ. In the barrel the tubes are up to 144cm long and offer no information on the z position, similarly at the ends no information on the R position is given. This is

much less precise than the silicon detectors, however, this is compensated for by each charged particle passing through causing about 36 hits and it offers a good extension to the track length. The volume between the tubes is filled with polypropylene foil or fibres which causes transition radiation when highly relativistic charged particles cross it, the amount of which is dependent on their Lorentz boost. This can help with electron identification, as they are lighter and hence more boosted resulting in a large pulse picked up in some tubes.

3.3. The Calorimeters

The Calorimeters measure the energy of both charged and neutral electromagnetic and hadronic particles. They are designed to give an accurate energy measurement over the full range of ϕ and up to high η (up to $|\eta| = 4.9$) such that an accurate measurement of the missing energy can be made, used for identifying neutrinos, which pass straight through the detector without interaction. They make use of the fact that hadrons penetrate further and have broader showers than electrons and photons with the electromagenetic calorimeter closer to the beam line than the hadronic calorimeter. Different technologies and materials are used in different regions due to different doses of radiation and different physics requirements. The calorimeter system is shown in Figure 3.4.

The calorimeters use alternating layers of active and passive material. The particles shower when they interact with material and the energy of these cascades is measured by the regions of active material. The calorimeters must be large enough to contain these showers, such that an effect known as punch-through does not occur, where the particles not fully absorbed by the calorimeters reach the muon detectors and cause a signal there. The electromagnetic showers are characterised by their radiation length, X_0 and the hadronic showers by their nuclear interaction length, λ, the value of which varies between different materials. The size of the calorimeter in terms of interaction lengths is shown in Figure 3.5

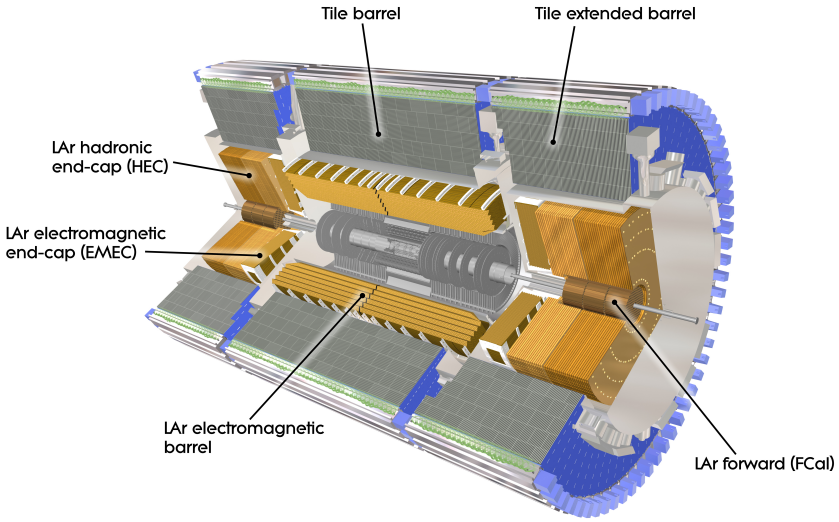

Figure 3.4.: The ATLAS calorimeter system [3]

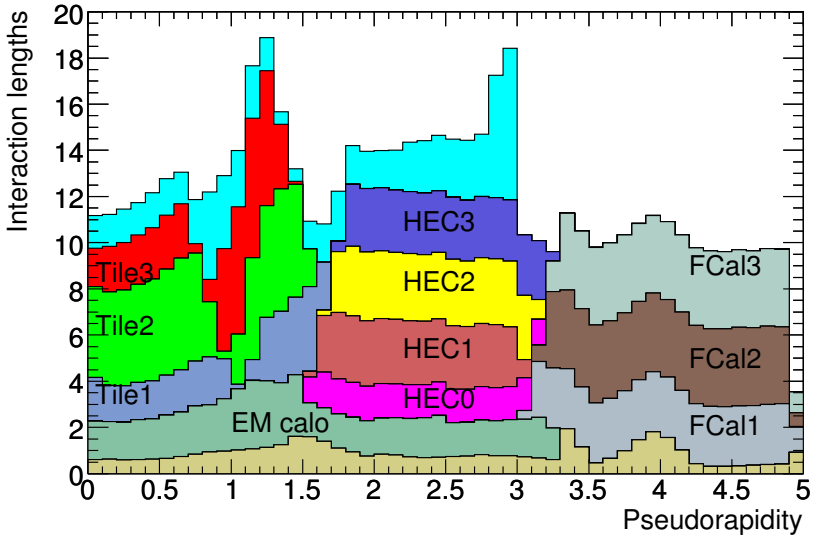

Figure 3.5.: The number of interaction lengths of material in the ATLAS calorimeters as a function of the position in terms of pseudorapidity. This is shown for the material before the calorimeters and for the electromagnetic calorimeter and each section of the hadronic calorimeter. The amount of material before the muon detector up to $|\eta| < 3.0$ is also shown [3].

3.3.1. The Electromagnetic Calorimeter

The Electromagnetic Calorimeter is a liquid-argon (LAr) sampling calorimeter, where the liquid-argon is the active material and lead is used as an absorber. It offers fine granularity such that precision measurements of electrons and photons can be made. It is divided into a barrel region covering $|\eta| < 1.475$ and two end caps for $1.375 < |\eta| < 3.2$, each in their own cryostat. The barrel is split into two identical half barrels which are separated by 4mm at $\eta = 0$ and the end caps each consist of two coaxial wheels, the inner one covering $1.375 < |\eta| < 2.5$ and the other $2.5 < |\eta| < 3.2$. To reduce the amount of material and hence improve the performance the LAr calorimeter and central solenoid are put in the same vacuum vessel.

The lead plates and copper electrodes are arranged in an accordion geometry to ensure complete ϕ symmetry without any cracks. In the barrel region it is separated into 3 longitudinal layers and reaches out to $22X_0$. In the end caps the calorimeter is $24X_0$ with the first wheel separated into three layers and the outer wheel into two and has a coarser granularity. In addition a presampler detector covers the region $|\eta| < 1.8$ which consists of a layer of liquid-argon 1.1cm thick in the barrel region and 0.5 cm in the end caps. It is used to correct for the energy lost in electrons and photons before they reach the calorimeter.

3.3.2. The Hadronic Calorimeter

The hadronic calorimeter uses scintillator-tiles in the barrel region ($|\eta| < 1.7$) and LAr calorimetry for the end caps ($|\eta| > 1.5$), both covering about 10λ. The tile calorimeter uses a steel absorber with scintillating plates as the active material, which are read out through wavelength-shifting fibres on each side of the scintillating tiles to photomultiplier tubes. It is divided into a central barrel region, $|\eta| < 1.0$, which is subdivided into 3 radial layers of 1.5, 4.1 and 1.8 λ thick, and two extended barrels for $0.8 < |\eta| < 1.7$, which is also formed of 3 radial layers of 1.5, 2.6 and 3.3 λ thick. Each of these consists of 64 modules in ϕ.

The Hadronic End Cap (HEC) uses LAr technology similar to the electromagnetic calorimeter. It covers $1.5 < |\eta| < 3.2$, overlapping slightly with the tile calorimeter and the Forward Calorimeter (FCal), such that the material density decrease in the transition region is reduced, lying directly behind the electromagnetic calorimeter

end caps, sharing a cryostat. There are 2 wheels per end cap with 32 wedges in ϕ, each wheel divided into two layers. It uses copper as an absorber (unlike the electromagnetic end caps), with 25mm sheets in the first layer and 50mm sheets in the second, separated by 8.5 mm of LAr.

3.3.3. The Forward Calorimeter

The FCal also uses LAr technology, both for electromagnetic and hadronic calorimetry measurements. It is designed such that it can cope with the high radiation environment and is dense such that it can fit in the limited space available, providing 10λ in depth. The electrodes are formed of concentric tubes and rods which lie parallel to the beam line with very small liquid-argon gaps, as small as 0.25mm, to avoid ion build-up in the high radiation environment close to the beam line. There are 3 modules, the first of which uses copper, focussed on electromagnetic measurements and the two further out use tungsten for hadronic measurements.

3.4. The Muon Spectrometer

The muon spectrometer accurately measures the position and momenta of muons, using the fact that they are the only particles which reliably pass through the calorimeter without stopping (aside from the neutrinos). The three barrel and two endcap air core toroid magnets provide a magnetic field roughly perpendicular to the muon momentum across the whole of the muon detector. To minimise multiple scatterings the detector covers a large volume but is of low density.

The detector is composed of four different components, as shown in Figure 3.6, two for precision tracking and two for triggering. The tracking is done for $|\eta| < 2.7$, mostly by Monitored Drift Tubes (MDTs), with Cathode Strip Chambers (CSCs) for the innermost layer at higher pseudorapidities, $2.0 < |\eta| < 2.7$. The triggering is done using Resisitive Plate Chambers (RPCs) for the most central region ($|\eta| < 1.05$) and Thin Gap Chambers (TGCs) in the end-caps ($1.05 < |\eta| < 2.4$). These provide bunch-crossing information as well as some additional information at the azimuthal position of the muons, and well-defined p_T thresholds. As for the central tracker

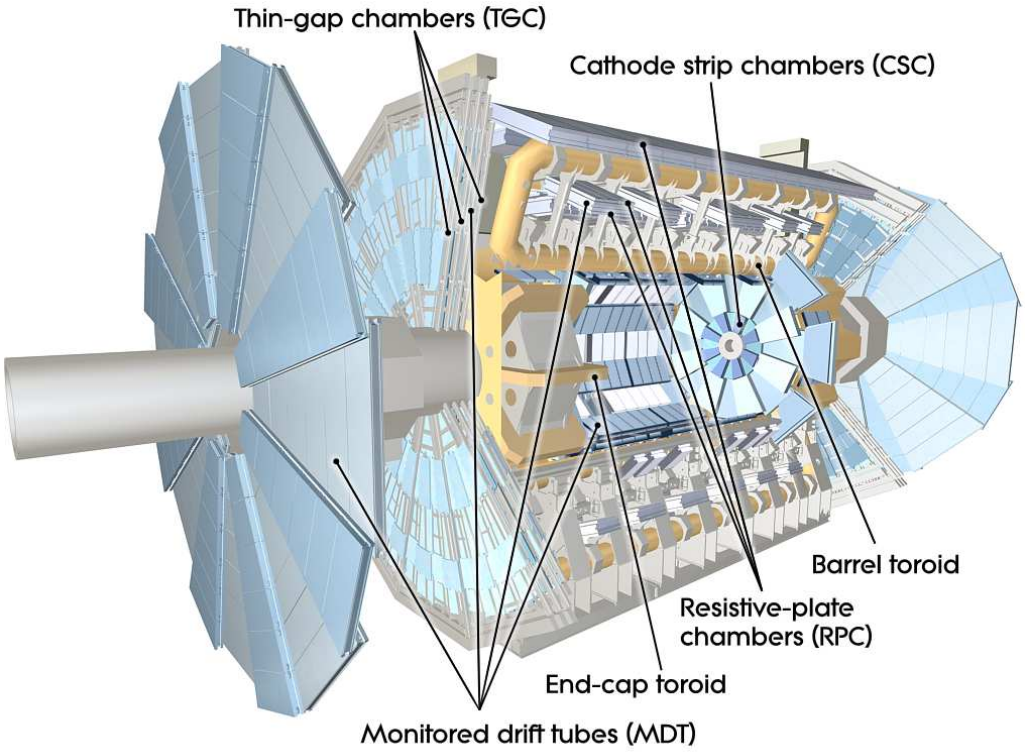

Figure 3.6.: The ATLAS muon spectrometer [3]

the hits are combined, based on pattern recognition, to find tracks consistent with muons and the curvature of the tracks provides momentum and charge information.

3.5. Luminosity

The luminosity is the number of events with the cross section σ that will occur per unit time and hence can be calculated as

$$\mathcal{L} = \frac{R}{\sigma} \tag{3.4}$$

where R is the interaction rate. The luminosity can also be calculated using properties of the beam

$$\mathcal{L} = \frac{n_b f n_p^2}{2\pi\sigma_x\sigma_y} \tag{3.5}$$

where n_b is the number of bunches per beam, f is the rotation frequency of the beam, n_p is the number of protons in each bunch and σ_x and σ_y characterise the width of the beam in the horizontal and vertical directions. From this equation it can be seen that the luminosity can be increased by decreasing the width of the beams, increasing the number of bunches or putting more protons in each bunch. A higher luminosity is preferable so that processes with low cross sections can be observed, however increasing the luminosity leads to more collisions in each bunch making detection more difficult.

3.6. Pileup and Underlying Event

Pileup is the number of inelastic collisions per bunch crossing, which increases as the instantaneous luminosity increases. Generally there is one hard scattering process of interest, with the other softer interactions essentially introducing a background level of energy across the detector. The shape of the LAr pulse is designed such that the pileup should be cancelled on average. The level of pileup in an event can be assessed by the number of vertices an event has. The vertices are constructed based on tracing tracks back to the beam line. Another useful quantity is the average number of interactions per bunch crossing, μ, which is calculated by averaging the number of interactions per bunch crossing over a large enough time window to include the whole period for which the calorimeter signal is sensitive to the collision activity.

The underlying event is composed of multiple parton interactions within a proton interacting and strong interactions between partons from different origins, known as colour reconnection. As in the case of pileup the other interactions are generally soft simply adding some background energy to the event. In both cases the energy of jets can be adjusted by subtracting the energy expected to come from pileup and the underlying event.

Chapter 4.

Analysis Techniques

4.1. Jet Construction in ATLAS

4.1.1. Calorimeter Jets

The sprays of hadrons produced from quarks and gluons produced in interactions are detected as energy deposits in the ATLAS calorimeters. These energy deposits do not correspond directly to hadrons due to the finite resolution of and electronic noise within the detector. Also some hadrons will go undetected, for example if they are scattered off other material before reaching the calorimeters. However, the calorimeter deposits need to be grouped into hadron-like objects to form inputs into the jet clustering algorithms described in Section 2.6. The simplest way to do this is to divide the calorimeter into towers [39] which are 0.1 x 0.1 blocks in η x ϕ, combining the cells or fractional contributions from cells. However, it is more common to use topological clusters [39] as inputs to jet reconstruction.

Topoclusters are 3 dimensional energy depositions in the calorimeter, which aim to roughly correlate to hadrons. The method of formation suppresses noise and doesn't involve all the cells in clusters. The process starts by taking a cell with energy, $E_{cell} > 4\sigma_{cell}$, where σ_{cell} is the standard deviation of the noise in that cell, as the seed cell. Any neighbouring cell with $E_{cell} > 2\sigma_{cell}$ is combined into this, repeating until there are no more neighbouring cells satisfying this condition. Lastly one layer of cells satisfying $E_{cell} > 0$ are added. These are then used as inputs to jet

clustering, with the mass taken to be 0 and the position taken as the energy-weighted centre of the cluster.

Once the clusters are formed, local maxima within them are searched for and if more than one maximum is found within a cluster it is split in two. A maxima is defined as a cell with an energy larger than 500 MeV, providing no neighbouring cell has a larger energy. The splitting algorithm combines neighbouring cells as before, but the cells lying on the border between two clusters can have their energy shared.

4.1.2. Track Jets

Jets can also be formed using tracks as inputs rather than calorimeter deposits. The tracks only pick up charged particles so don't give an accurate reconstruction of the jet but it is useful to compare these track jets to the calorimeter jets to give an estimate of the systematic uncertainties. The tracks that enter the jet clustering algorithms have to pass some quality cuts, but otherwise their four vectors are used as a direct input to the jet clustering algorithm. The tracks must pass some quality cuts to be used in the tracks collection, namely that they have $p_T > 500$ MeV, there are at least 7 hits in the pixel and silicon tracking detectors and the χ^2 per degree of freedom for the track is no more than 3. The track must also satisfy $z \sin\theta < 2$mm and $d < 2$mm, where d is the impact parameter of the track from the beam spot.

4.1.3. Ghost Association of Tracks to Jets

Ghost association [40] is a method of associating tracks to jets by involving them in the clustering. This is preferable to a geometrical matching because jets are not always circular. The p_T of the tracks, passing the same quality cuts as for track jets, are made infinitesimally small and the mass set to 0, but the η and ϕ coordinates kept the same and these are then added to the set of calorimeter clusters usually used for forming jets. The jet clustering process is rerun and should produce the same jets, as any infrared safe jet clustering algorithm will not be affected by the infinitesimally-low p_T track objects. Then the tracks which appear as constituents of the jet of interest are considered to be ghost-associated to it.

4.2. Jet Calibration

The calorimeter cells measure energy at the electromagnetic scale, giving the correct energy for an electromagnetic shower deposit. However, hadrons have a lower response which is not accounted for, as well as some energy escaping due to dead material in the detector, or not being detected above the level of noise. As a result the jets are calibrated to provide a more accurate measurement of the energy. This can be done by calibrating the individual clusters, and then providing a small correction to the jets obtained, or by simply calibrating the jets without changing the clusters first. The jet calibration [41, 42] is divided into three steps, the pileup correction, the origin correction and finally the Jet Energy Scale (JES) correction.

4.2.1. Local Hadronic Calibration of Topological Clusters

The topological clusters used as an input to the jet clustering algorithms can be calibrated [43]. The correction is applied on a cluster-by-cluster basis, dependent on whether it is identified as a hadronic or electromagnetic cluster, on its position in the detector and on its energy. The clusters are classified based on their depth in the calorimeter and the energy density, with the hadronic showers being less dense but reaching further. The clusters identified as hadronic have a hadronic weighting applied to account for the non-compensation of the calorimeters.

After this both the hadronic and electromagnetic clusters are adjusted by the out-of-cluster correction, which accounts for energy lost due to the cell noise thresholds. The isolation of the clusters is considered and the out-of-cluster correction changed accordingly. Lastly a correction is applied for energy that is lost in dead material in the detector, considering eight different detector regions.

The resulting jets based on these calibrated clusters then have calibration applied in the same way as those based on the electromagnetic scale clusters, obviously with different calibration constants.

4.2.2. Pileup Correction to jets

Pileup interactions add extra energy deposits to the calorimeters, generally softer than the hard interaction of interest which can affect the energy of the reconstructed jets. The level of pileup in an event can be assessed by looking at the number of primary vertices (N_{PV}) and the average number of interactions per bunch crossing (μ) in an event. The average pileup contribution to an event is calculated as a function of N_{PV} and η and the jets adjusted accordingly. For data taken in 2012 a jet area based pileup correction was introduced and applied before a residual offset correction similar to that described above. However, this is not used in the analyses presented here.

4.2.3. Jet Origin Correction

The positions of the jets are initially calculated assuming that they came from the centre of the ATLAS detector, however, this is rarely the case. The vertices in an event can be identified by looking at the points that the tracks come from and the primary vertex is the one for which the scalar sum of the p_T of tracks originating from it is largest. Each of the calorimeter clusters has the direction adjusted such that it comes from this primary vertex and the clusters in a jet are then resummed to produce the final origin corrected jet.

4.2.4. Jet Energy Scale

The final correction is the Jet Energy Scale (JES) to account for the lower response of hadrons in the calorimeters. The correction is calculated using MC simulation so that the final reconstructed jets can be compared to those at particle level, truth jets. The truth jets are formed using the same jet clustering algorithm as is run on the topoclusters but using the MC particles as four-vector inputs. All stable particles are included except muons, which are minimally interacting and neutrinos, which are not detected in the calorimeters. These truth jets are geometrically matched to reconstructed jets and by comparing the energy a correction factor is calculated, as a function of both the jet energy and its η position. Lastly, after this has been applied, a small η correction is also applied to adjust jets falling in crack regions of

the detector. The JES is calculated for jets using both calibrated and uncalibrated clusters as inputs.

4.3. Jet Cleaning

Before any jets from data are used in analyses they need to pass some quality requirements [44], designed to remove fake jets coming from background events or caused by detector effects (bad jets) and those that are not well measured by the detector due to problems with the calorimeter (ugly jets). Bad jets can be divided into three main categories, firstly those caused by a spike in the HEC, which are characterised by having most of their energy coming from a single cell. The second is those caused by noise bursts in the EM calorimeter, which leads to a jet with most of its energy in the EM calorimeter with badly reconstructed cells. This is measured by how well the pulses match the digitised samples, which in turn indicates how good the amplitude measurement is. Lastly, bad jets can be caused by cosmics or the beam background, which are generally not in time with the rest of the event. There are several variables that can be used to identify and remove these jets, as defined in Table 4.1.

Four different sets of cuts have produced with increasingly stronger requirements on these variables to reject these bad jets, known as looser, loose, medium and tight jet cleaning. A summary of these cuts is shown in Table 4.2. The number of analysis jets removed by these cuts is less than a percent.

4.4. Data Quality Requirements

4.4.1. Good Runs Lists

Before any event is considered for an analysis it must pass the Good Runs List (GRL) [44] which is a list of luminosity blocks where all the relevant parts of the detector are operating correctly. The luminosity blocks are sections of the data about

Table 4.1.: Jet Cleaning Variables

EM_f	fraction of energy deposited in the EM calorimeter
f_{max}	maximum fraction of energy deposited in a single calorimeter layer
HEC_f	fraction of energy deposited in the HEC
LAr_Q	fraction of energy deposited in LAr cells with a cell Q-factor > 4000
HEC_Q	fraction of energy deposited in HEC cells with a cell Q-factor > 4000
E_{neg}	negative energy in the jet
t	jet time calculated from the mean time of the cells in the jet
η	η of the jet at the EM scale
ch_f	the charged fraction of the jet : $\frac{\sum p_T^{track}}{p_T^{jet}}$

2 minutes in length. The GRL flag is decided offline considering the various parts of the detector, the luminosity recording and the triggers.

4.4.2. LAr Hole

In 2011 data taking, for periods E to H, a crate in the LAr calorimeter failed so any jets falling in this region of the detector may be mismeasured. The region affected is $0.1 < \eta < 1.5$ and $-0.9 < \phi < -0.5$. The failure is replicated in Monte Carlo so should not affect comparisons between data and MC and should not have a major impact on analyses. However, some analyses choose to exclude this regions while others apply a correction to the energy of jets falling in this region to adjust for that missing due to the LAr hole.

4.4.3. LAr and Tile Errors and Incomplete Events

Events with noise bursts in the LAr calorimeters as well as events with data corruption in either the tile or LAr calorimeters must be rejected. These events are flagged during data taking and so are easily rejected. The tile calorimeter also has frequent module trips which are generally corrected for offline and hence do not affect the data for analyses. However, in 2012 data taking between periods E and J, there were occasional trips in one module which were not identified and masked and hence these

Table 4.2.: Jet Cleaning Requirements

	looser	loose	medium	tight
HEC spike	$HEC_f > 0.5$ and $\|HEC_Q\| > 0.5$ and $LAr_Q^{mean} > 0.8$ – OR – $\|E_{neg}\| > 6GeV$	$HEC_f > 0.5$ and $\|HEC_Q\| > 0.5$	$HEC_f > 1 - \|HEC_Q\|$	
EM coherent noise	$EM_f > 0.95$ and $\|LAr_Q\| > 0.8$ and $LAr_Q^{mean} > 0.8$ and $\|\eta\| < 2.8$	$EM_f > 0.95$ and $\|LAr_Q\| > 0.8$ and $\|\eta\| < 2.8$	$EM_f > 0.9$ and $\|LAr_Q\| > 0.8$ and $\|\eta\| < 2.8$	$LAr_Q > 0.95$ – OR – $EM_f > 0.98$ $\|LAr_Q\| > 0.05$
Cosmics and beam background	$EM_f < 0.05$ and $ch_f < 0.05$ and $\|\eta\| < 2$ – OR – $EM_f < 0.05$ and $\|\eta\| \geq 2$ – OR – $f_{max} > 0.99$ and $\|\eta\| < 2$	$\|t\| > 25$	$\|t\| > 10$ ns – OR – $EM_f < 0.05$ and $ch_f < 0.1$ and $\|\eta\| < 2$ – OR – $EM_f > 0.95$ and $ch_f < 0.05$ and $\|\eta\| < 2$	$EM_f < 0.1$ and $ch_f < 0.2$ and $\|\eta\| < 2.5$ – OR – $EM_f > 0.9$ and $ch_f < 0.1$ and $\|\eta\| < 2.5$ – OR – $ch_f < 0.01$ and $\|\eta\| < 2.5$ – OR – $EM_f < 0.1$ and $\|\eta\| < 2.5$

events also need to be rejected. Lastly there are some events in 2012 data taking which have some detector information missing and hence are said to be incomplete. These occur when recovering from busy detector periods without requiring a full run restart. These events are also excluded from physics analyses.

Chapter 5.

ATLAS Trigger System

In 2011 the LHC ran at a centre of mass energy of 7 TeV with a bunch spacing of 50 ns with more than 10^{11} protons per bunch delivering a luminosity of about $3 \times 10^{33}\text{cm}^{-2}\text{s}^{-1}$. This produces an event rate of about 20 MHz and a proton proton interaction rate of about 0.2 GHz. In 2012 the centre of mass energy was increased to 8 TeV, keeping the same bunch spacing but increasing to a luminosity of about $6 \times 10^{33}\text{cm}^{-2}\text{s}^{-1}$ and hence an interaction rate of about 0.4 GHz. At design, with a centre of mass energy of 14 TeV and luminosity of about $10^{34}\text{cm}^{-2}\text{s}^{-1}$, the rate will increase to about 1 GHz. However these rates are far too high to record all the data and hence events are triggered on and only those passing various trigger requirements are kept and reconstructed for analysis.

There are three levels to the ATLAS trigger - level 1 (L1), level 2 (L2) and event filter (EF). L1 is a hardware based trigger which has 2.5 μs to reduce the event rate to 75 kHz, the maximal rate of the detector readout system. As the decision has to be made so quickly at this stage only reduced granularity information from the calorimeters and muon detectors is available to search for muons, electrons, photons, jets and tau leptons. The L1 calorimeter trigger looks for high energy objects, possibly requiring some isolation, or a high total E_T or E_T^{miss}. The L1 muon trigger looks for patterns of hits consistent with muons originating from the interaction region and bins them into six p_T regions. The L1 then sends information about the location of the trigger objects to the L2 trigger in the form of regions of interest (RoIs).

L2 and EF are collectively known as the software-based High-Level Trigger (HLT). L2 reduces the rate to 3.5 kHz with a latency of 40ms. It reconstructs the event in

the RoIs, using the full granularity of the detector to make a decision, which results in about 2% of the total event information being reconstructed. This allows for more accurate decisions as both the energies and positions of the objects are better reconstructed and information from other areas of the detector, such as the tracking can also be used. Finally the EF reconstructs the full event, using similar methods to offline analyses, to make a decision in about 4s after which the rate is about 400 Hz.

Most trigger chains are prescaled at L1 and HLT to keep the rate within the limits allowed. A prescale of X means that only 1 in every X events is taken by the trigger using a random sampling in the HLT and by taking X^{th} event at L1.

5.1. The ATLAS Jet Trigger

The ATLAS jet trigger is allocated about 10% of the total rate allowed at each level of the system. It looks for jets above a certain E_T threshold, sometimes adding in further requirements in the HLT. It is divided into a central ($|\eta| < 3.2$) and forward ($3.2 < |\eta| < 4.9$) region. The cross section for producing jets falls as the E_T increases so the jet trigger aims to keep a selection of jets across the full range of E_T, with roughly equal rates. This means high prescales need to be placed on the lowest E_T thresholds but the highest thresholds are kept unprescaled.

The jet trigger menu consists of inclusive jet, multi-jet and topological triggers. Inclusive jet triggers simply require a jet above a certain E_T threshold. These thresholds increase from L1 to L2 to EF, such that the 100% efficiency (plateau) points at each level match up, for example a jet trigger requirement of $E_T > 55$ GeV at the event filter is seeded from a trigger requirement of $E_T > 50$ GeV at L2 and $E_T > 30$ GeV at L1. This would be written as L1_J30 - L2_j50 - EF_j55_a4tc_EFFS, where the j stands for jet (fj is used for a forward jet trigger), a4tc means the jets are reconstructed using the anti-k_T jet algorithm with a radius of 0.4 based on topoclusters and EFFS stands for event filter full scan. Different jet radii can be considered at EF level.

As the name suggests, multi-jet triggers require more than one jet above a given E_T threshold in the event and in the chain name the letter j is preceeded by the required jet multiplicity, for example 4j for a 4 jet trigger. Topological triggers add

some extra requirement such as a $\Delta\eta$ requirement. The jet triggers can also be combined with requirements for other objects in the event such as leptons.

Chapter 6.

Forward Jet Trigger Performance Studies

The performance of the jet triggers is constantly monitored to check they are behaving as expected and that the thresholds have been chosen correctly such that the allowed rate is not exceeded and the highest threshold remains unprescaled. Here, the performance of the forward jet trigger based on 2011 data is shown in terms of efficiency plots along with a comparison to MC.

6.1. Event Selection

The efficiency plots are calculated with respect to fully reconstructed anti-k_T, R=0.4 jets in the forward region passing the selection cuts. The events in data must pass the GRL. The events must also pass some quality requirements, which are described in more detail in Section 4.3. Firstly any events with jets that are considered bad with the loosest requirements are rejected. Events are also not kept if they have a LAr error or any jets in the LAr hole. The events must also have at least one primary vertex with at least two tracks.

A jet cannot be ugly and must be in the region $3.6 < |\eta| < 4.4$ so that it is fully contained within the forward jet trigger detector region. They also must pass a seed trigger with a lower E_T threshold chosen to be fully efficient in the turn on region of the trigger being considered. The jet is then required to be matched to a trigger jet at L1, L2 and EF. The matching between offline and EF jets, and then between

EF and L2 jets is done by finding the closest jet within ΔR of 0.2. The matching between L2 and L1 is done by requiring a L1 jet in the forward region of the detector with $\Delta\phi$ less than 0.4 from the L2 jet. This is because the η information is not available at L1 for the forward jets.

6.2. Efficiency Plots

The offline jets are calibrated using the offset η JES correction, and this offline E_T is the scale used for the efficiency plots. The efficiency is defined as

$$\text{Efficiency} = \frac{\text{Number of jets with trigger jet } E_T > \text{threshold}}{\text{Total number of jets}} \tag{6.1}$$

where the total number of jets is those passing the selection cuts and the seed trigger. The seed trigger used for the lowest threshold is EF_fj10_a4tc_EFFS, which is fully efficient for an offline calibrated jet E_T above 20 GeV, so the turn on curve is valid for values above this. The higher thresholds use EF_fj30_a4tc_EFFS as a seed trigger which is fully efficiency above 40 GeV. This was done for three of the forward jet triggers: L1_FJ10 - L2_fj25 - EF_fj30, L1_FJ30 - L2_fj50 - EF_fj55 and L1_FJ50 - L2_fj70 - EF_fj75, as shown in Figure 6.1. Efficiency curves for the high-E_T chain, L1_FJ75 - L2_fj95 - EF_fj100, are not included because there are not enough events in the forward region to make these plots.

The turn on curves show the behaviour expected with the L1 curves much slower to turn on than the L2 and EF curves, due to the worse energy resolution of the L1 calo system with respect to the offline. The point at which the triggers become 100% efficient roughly matches up between the corresponding L1, L2 and EF thresholds, showing they are chosen correctly such that unnecessary rate isn't wasted at L1. The agreement between the data and the PYTHIA and HERWIG MCs is not perfect, but the plateau points agree fairly well, with the largest discrepancies shown in the modelling of the L1 trigger.

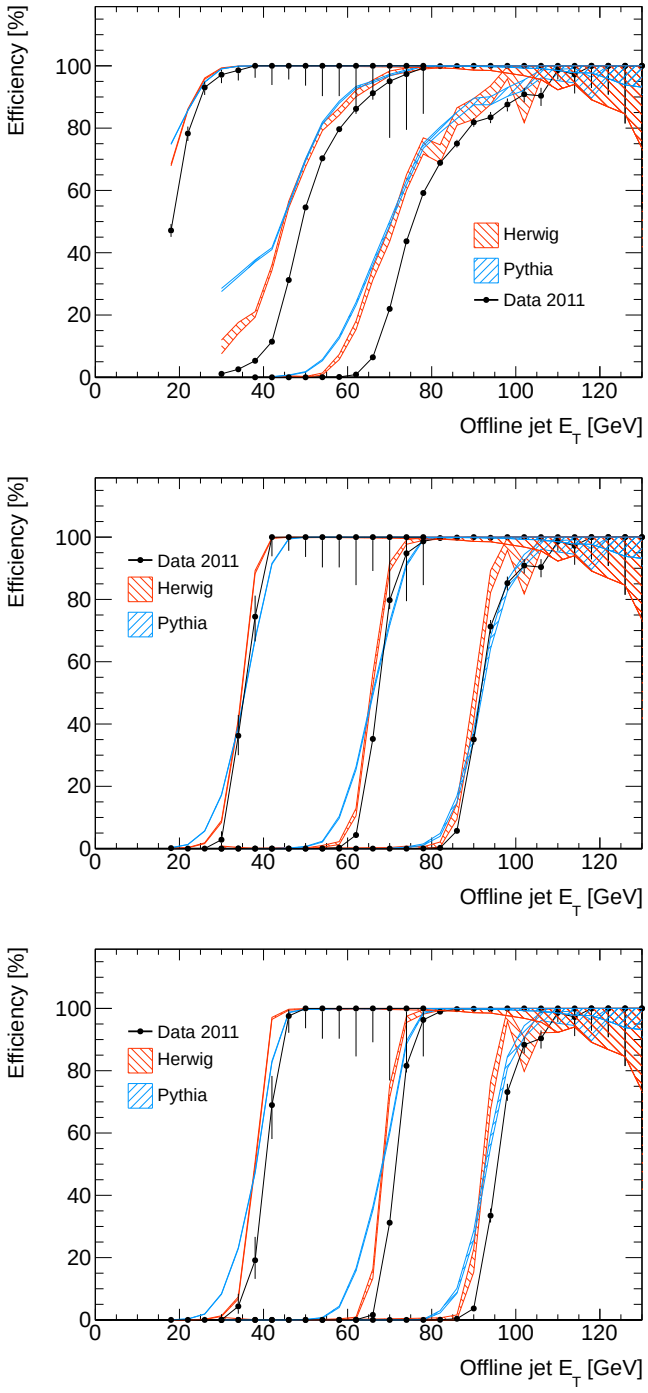

Figure 6.1.: The turn on curve for three forward jet trigger thresholds, L1_FJ10, L1_FJ30 and L1_FJ50 (top), L2_fj25, L2_fj50 and L2_fj70 (middle), and EF_fj30, sEF_fj55 and EF_fj75 (bottom), in data and pythia and herwig MC samples.

Chapter 7.

Applying Energy Scale Calibration to the ATLAS Jet Trigger

7.1. Introduction

In 2011, the ATLAS jet trigger was selecting jets based on their E_T at the EM scale, which is the sum of the energy measured by the electromagnetic and hadronic calorimeters. This energy scale correctly accounts for electromagnetic deposits in the calorimeter, established from test beam measurements of electrons and photons, however, it does not account for the fact that the response of the calorimeters from hadrons is lower.

For offline analyses the jets are calibrated as described in Section 4.2. The EM+JES calibration scheme applies p_T-η dependent calibration factors to jets at the EM scale based on comparison between calorimeter and truth jets in the MC. Within the boundary dictated by the trigger latency, it is preferable for jet reconstruction at trigger level to be as similar to what is done for offline analyses as possible. This means that the selection will produce a clearer match to that used in offline analyses and makes it easier to understand in terms of the jets used in analyses. It is also possible that applying calibration will sharpen the turn on curves, or improve the rejection of the triggers while maintaining the same 100% efficiency point, cutting out only jets which would be rejected by the offline analysis. To calibrate the trigger jets it is possible to calculate a new set of correction factors for each level of the trigger and there are also more complicated calibration schemes that could be investigated.

Here, as a first study and for simplicity, the calibration factors used for offline jets are applied based on the p_T and η of the trigger jet.

The effect calibration has on the trigger and how useful it is to apply is assessed by simulating the effect of such a change and producing turn on curves with and without the calibration applied. As calibration changes the energy of a jet the threshold used in the calibrated trigger must be adjusted and this is chosen such that the 99% efficiency points on the two turn on curves match. The improvement that can be made is assessed by calculating the difference in rate of the two curves using

$$\text{Rate difference} = \frac{\text{EMscale rate - Calibrated rate}}{\text{EMscale rate}} \tag{7.1}$$

7.2. Event Selection

The application of calibration at trigger level is investigated using 2011 data. The events must first pass the GRL and must also have at least one primary vertex with at least 4 tracks. The offline jets used are reconstructed with the anti-k_T jet algorithm with a radius of 0.4 and these jets must pass the quality requirements. This cleaning is described in Section 4.3 and here the jets are required not to be either ugly or bad, using the tightest criteria for selecting a bad jet.

The effect of applying calibration to both the central and forward jet triggers is considered. For the central jet trigger the highest p_T jet in the event with $|\eta| < 2.8$ is considered and for the forward jet trigger the highest p_T jet in the event in the range $3.6 < |\eta| < 4.4$ is used. The split between the central and forward jet triggers is at $|\eta| = 3.2$ and so choosing these ranges ensures that the jet is fully contained within the central or forward jet trigger region of the detector.

These offline jets are then required to be matched to a trigger jet at each level. First the offline jet is matched to an EF jet by finding the closest jet within a ΔR of 0.4. Then the EF jet is matched to the closest L2 jet within a ΔR of 0.4. Finally the L2 jet is matched to L1 using the RoI information that is stored at L1 and L2. Providing a jet is found at each of these levels the jet is used to calculate the trigger efficiencies.

The jets considered for a particular trigger efficiency curve must pass a seed trigger with a lower threshold that is fully efficient in the p_T range that is considered for the turn on curve, as for the forward jet trigger efficiency plots. The list of triggers considered are summarised in Table 7.1 along with the corresponding seed triggers.

7.3. Trigger Efficiency Curves

The trigger efficiency curve is made using equation 6.1 where the total number of jets is given by those passing the criteria specified above, including the seed trigger. The turn on curve for the calibrated triggers is then calculated in a similar way, but the trigger E_T is calibrated using the EMJES calibration scheme. The correction factors based on the jet E_T and η are not recalculated for the trigger jets, instead the same values as those used for offline reconstruction are used.

Applying the calibration generally increases the E_T of a jet and so to get the efficiency curves to reach plateau at the same value of offline E_T the thresholds chosen for the calibrated triggers should be raised relative to the thresholds used for the EM scale triggers. The calibrated thresholds are chosen by matching the plateau points for the EM and calibrated triggers. The values used are shown in Table 7.2, along with the rate difference associated with each one. Note that a positive value means the rate was reduced by applying calibration. The resulting plots for each trigger chain, showing both the EM scale and calibrated scale triggers are shown in Figure 7.1 for the central jet trigger chains and Figure 7.2 for the forward jet trigger chains. The calibrated triggers have a sharper turn on curve than the EMscale triggers, which is supported by the rate savings in the table. Based on this it was concluded that applying calibration to the trigger is desirable for improving the performance, as well as bringing the trigger jets closer to offline analyses, so JES calibration was added to the trigger and tested at the end of 2011 running. Calibration was applied to most of the jet triggers in 2012.

Table 7.1.: The jet trigger thresholds considered for applying calibration

L1	L2	EF	seed trigger
L1_J15	L2_j35	EF_j40_a4tc_EFFS	EF_j30_a4tc_EFFS
L1_J30	L2_j50	EF_j55_a4tc_EFFS	EF_j30_a4tc_EFFS
L1_J50	L2_j70	EF_j75_a4tc_EFFS	EF_j40_a4tc_EFFS
L1_J75	L2_j95	EF_j100_a4tc_EFFS	EF_j55_a4tc_EFFS
L1_FJ30	L2_fj50	EF_fj55_a4tc_EFFS	EF_fj30_a4tc_EFFS
L1_FJ50	L2_fj70	EF_fj75_a4tc_EFFS	EF_fj30_a4tc_EFFS

Table 7.2.: The calibrated thresholds used for the triggers along with the associated rate difference.

EMscale threshold	Calibrated threshold	L2 rate difference	EF rate difference
L1_J15 - L2_j35 - EF_j40	L1_J15 - L2_j55 - EF_j60	0.0527	-0.0386
L1_J30 - L2_j50 - EF_j55	L1_J30 - L2_j80 - EF_j85	0.2760	0.2229
L1_J50 - L2_j70 - EF_j75	L1_J50 - L2_j105 - EF_j110	0.1975	0.1644
L1_J75 - L2_j95 - EF_j100	L1_J75 - L2_j135 - EF_j140	0.1178	0.0973
L1_FJ30 - L2_fj50 - EF_fj55	L1_FJ30 - L2_fj65 - EF_fj70	0.1525	0.0860
L1_FJ50 - L2_fj70 - EF_fj75	L1_FJ50 - L2_fj95 - EF_fj100	0.5672	0.5566

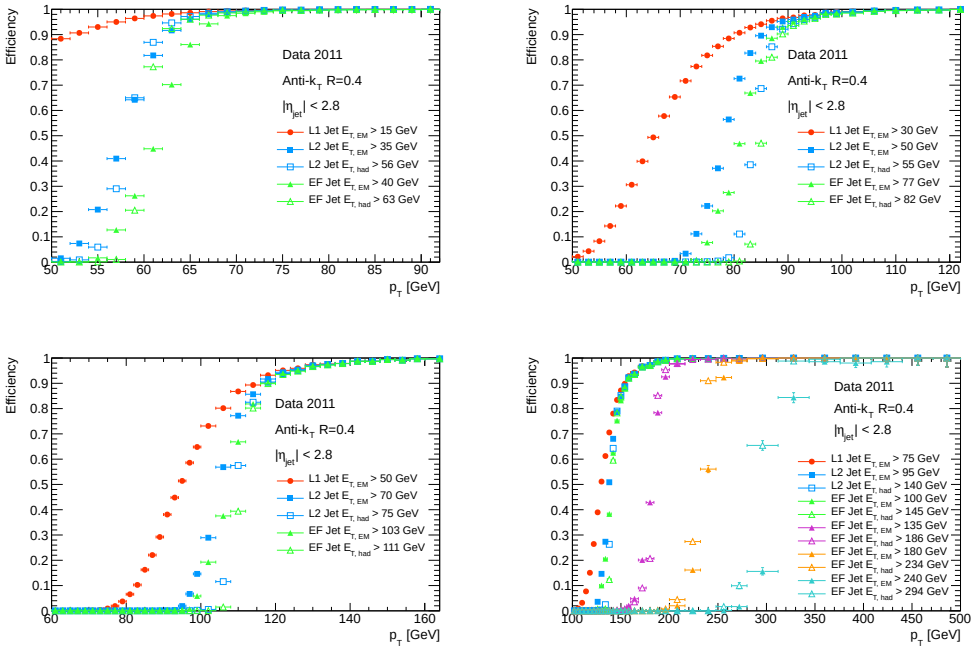

Figure 7.1.: The turn on curves for the central jet triggers at L1, L2 and EF and the corresponding simulated calibrated triggers with thresholds chosen such that the plateau points for the calibrated triggers match up to the uncalibrated ones.

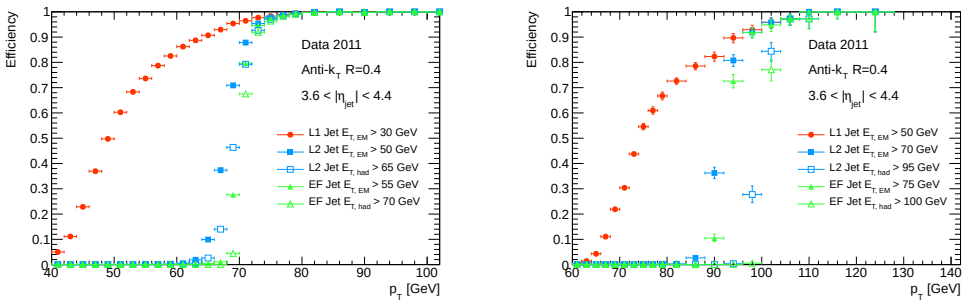

Figure 7.2.: The turn on curves for the forward jet triggers at L1, L2 and EF and the corresponding simulated calibrated triggers chosen with the thresholds chosen such that the plateau points for the calibrated triggers match up to the uncalibrated ones.

Chapter 8.

Hadronically decaying Boosted W/Z Bosons

8.1. Introduction

About two thirds of all decays of W and Z bosons are hadronic, as shown in Table 8.1, however, hadronic decays are difficult to observe over the large QCD background. At high p_T the background falls off faster than the signal, so this 'boosted' regime has more manageable initial signal/background (S/B) ratios. High energy decays of W and Z bosons are very useful in the search for new physics where they may be produced by decays of new heavy resonances, for example a W', a Z', a heavy higgs or fourth generation quarks, at the TeV scale. The identification of hadronically decaying boosted W/Z bosons is a prerequisite to such searches.

	branching ratios	
	W	Z
$l\nu$, ll	22%	7%
$\tau\nu$, $\tau\tau$	11%	3%
$\nu\nu$	0%	20%
qq	67%	70%

Table 8.1.: The branching ratios for W and Z boson decays where l represents both electrons and muons.

At energies above a few hundred GeV the decay products of the W or Z boson become highly collimated and will be reconstructed as a single jet, hence the structure within the jet must be used to distinguish the signal from the background. A variety of techniques [45–49] have been proposed to do this, mostly using the jet constituents to identify the structure. Here, a method using the clusters in the centre of mass frame of the jet [50] is used to suppress the background to a level where the signal can be seen.

This W signal peak can be used as a "standard candle" to assess the performance of jet grooming techniques, which have been studied in the context of QCD events and top decays [51–54], specifically for jets already exhibiting a strong two-body structure - "signal-like" jets. The grooming techniques aim to remove the jet constituents coming from the underlying event and pileup leaving behind just the hard structure. This means that the jet mass should more accurately reflect the mass of the boson it came from, improving its resolution. The jet shapes can also be recalculated using the new set of jet constituents obtained after grooming and a selection based on these can be used to select the jets. To assess how well jet grooming techniques perform they were looked at in terms of data-MC agreement, pileup reduction and improvement in s/b significance.

8.2. Monte Carlo Samples

In all the studies shown here the default MC for the signal is generated using HERWIG and multiplied by a NLO/LO k-factor of 1.25 calculated based on the ratio between the cross sections from MCFM [55] (NLO) and HERWIG (LO). Signal samples have also been generated using PYTHIA 8 and PYTHIA 6 with both AMBT1 and AMBT2B tunes.

The default background MC is generated using PYTHIA 8, chosen as it gives the best agreement in distributions of jet shapes, jet p_T and jet mass. For comparison and evaluation of systematics background samples have also been produced with HERWIG++, PYTHIA 8, POWHEG and PYTHIA 6 using the AMBT1, AMBT2B and PERUGIA 2011 tunes. The default signal and background MC samples are from different generators based on what was available at the time, but the systematic errors cover the differences between the generators.

8.3. Event Selection

8.3.1. Kinematic and Cleaning Cuts

The events used in this analysis were taken in 2011, corresponding to a luminosity of 4.7 fb^{-1} [56]. They are required to pass the EF_j100_a4tc_EFFS_ht350 (periods D-J), or the EF_j100_a4tc_EFFS_ht400 (periods K-M) trigger which were unprescaled for 2011 data taking. At EF trigger level these require one jet to have $p_T > 100$ GeV and the event to have $H_T > 350$ or 400 GeV respectively, where H_T is the scalar sum of the p_T of jets with $p_T > 30$ GeV and $|\eta| < 3.2$ in the event. Additionally, data events are required to pass the GRL. The events in MC are also reweighted such that the distribution of the average number of pileup interactions matches between data and MC.

Jets are reconstructed with the anti-k_T algorithm with a jet radius of 0.6 and then have a jet energy calibration applied as described in Section 4.2. These jets are then required to have a $p_T > 320$ GeV and $|\eta| < 1.9$. This requirement ensures that the trigger is close to 100% efficient. The radius of 0.6 was chosen based on the fact that for a two body decay the angular separation of the decay products is given by approximately $\Delta R \sim 2m_X/p_T$ [57] where the mass and p_T are those of the decaying particle. Hence a radius of 0.6 ensures that in the majority of cases the decay products of the high p_T W will be contained within the jet. These jets are required to pass medium cleaning requirements, as described in Section 4.3.

8.3.2. Jet Shapes in the Centre of Mass Frame

After the basic kinematic cuts have been made the signal is still a couple of orders of magnitude below the QCD dijet background as shown in Figure 8.1. Further discrimination between signal and background can be gained by looking at the distribution of the constituents within the jet. The signal jets are expected to have a two-body structure caused by the jet constituents from the two decay products being contained within the single jet, whereas the background should have a more isotropic structure. Various techniques [45–50] have been developed to assess the difference between these two types of jets. In this analysis jet shapes calculated from the jet in its centre of mass frame are used.

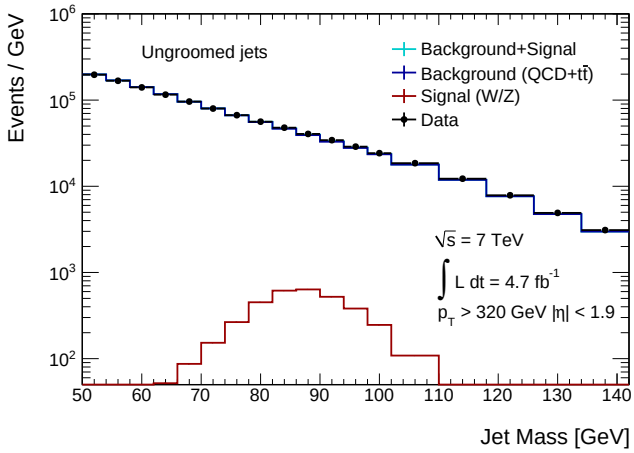

Figure 8.1.: The invariant mass distribution for the signal, background MC and data after the basic kinematic and cleaning cuts but before any further selection.

Boosting the jet back into its centre of mass frame should leave the W/Z jets with a back-to-back topology, whereas the background jets should be more isotropically distributed, as shown in Figure 8.2. Then various shapes can be used to assess how signal-like the jet is [58], or how linearly the constituents are distributed. The jet shapes considered were sphericity [59], thrust major [60, 61], thrust minor [60, 61], aplanarity [59] and the fox wolfram moments [62]. It was found that to get the best background rejection while maintaining a high signal efficiency and prevent the background distribution from peaking under the signal, an uncorrelated likelihood composed of three of these shape variables should be used: sphericity, thrust minor and aplanarity.

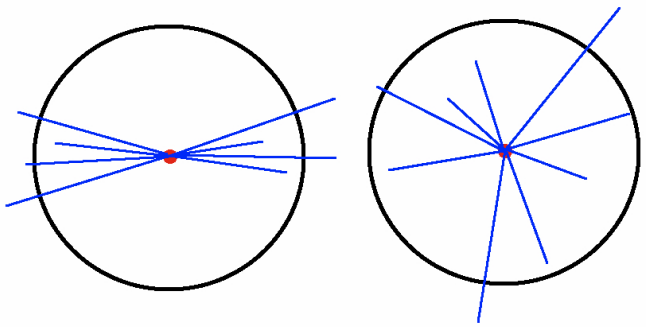

Figure 8.2.: The expected distributions of the jet constitents of signal jets (left) and background jets (right) when boosted into the centre of mass frame.

The sphericity is a measure of how isotropically the constituents are distributed, or how well the constituents cover a sphere. The aplanarity measures how well the constituents are confined to a plane. Both these shapes are based on the sphericity tensor which is defined as:

$$S^{\alpha\beta} = \frac{\sum_i p_i^\alpha p_i^\beta}{\sum_i |\overrightarrow{p}_i|^2} \tag{8.1}$$

where α and β refer to the x and y components of the momentum vector of each constituent. This tensor has three eigenvalues $\lambda_1 \geq \lambda_2 \geq \lambda_3$ with $\lambda_1 + \lambda_2 + \lambda_3 = 1$. The sphericity is defined as

$$S = \frac{3}{2}(\lambda_2 + \lambda_3) \tag{8.2}$$

This is essentially a sum of the squares of the momenta lying transverse to the jet axis normalised such that $0 \leq S \leq 1$. The more isotropic the jet the closer the value to 1.

The aplanarity is given by

$$A = \frac{3\lambda_3}{2} \tag{8.3}$$

This is a measure of how much of the momentum lies outside the main plane of the jet. It takes values $0 \leq A \leq \frac{1}{2}$ where a more isotropic distribution leads to a value closer to $\frac{1}{2}$.

The minor thrust is an assessment of how much of the momenta of the constituents lies perpendicular to the direction which maximises the sum of the longitudinal momenta of the energy of the constituents, $\hat{T}$, calculated using an iterative procedure. The constituent with the largest p_T is taken as the starting vector, the constituents in the event are then added or subtracted based on whether they have a positive or negative contribution to the momentum along that axis. If this matches the starting axis, this is taken as $\hat{T}$, otherwise the process is repeated starting with this new axis. This is repeated with the second, third and fourth highest transverse momentum constituents to ensure that the method has not found a local minimum. The thrust

is then defined as

$$T = \frac{\sum_i |\overrightarrow{p}_i \times \hat{T}|}{\sum_i |\overrightarrow{p}_i|} \tag{8.4}$$

It takes values $0 \leq T \leq \frac{1}{2}$ where the more isotropic the distribution the closer the value is to $\frac{1}{2}$.

The distributions of these variables in signal and background MC and data are shown in Figure 8.3. The shapes are also plotted for various different MCs in Figure 8.4 which shows that there is reasonable agreement between the different models and the data.

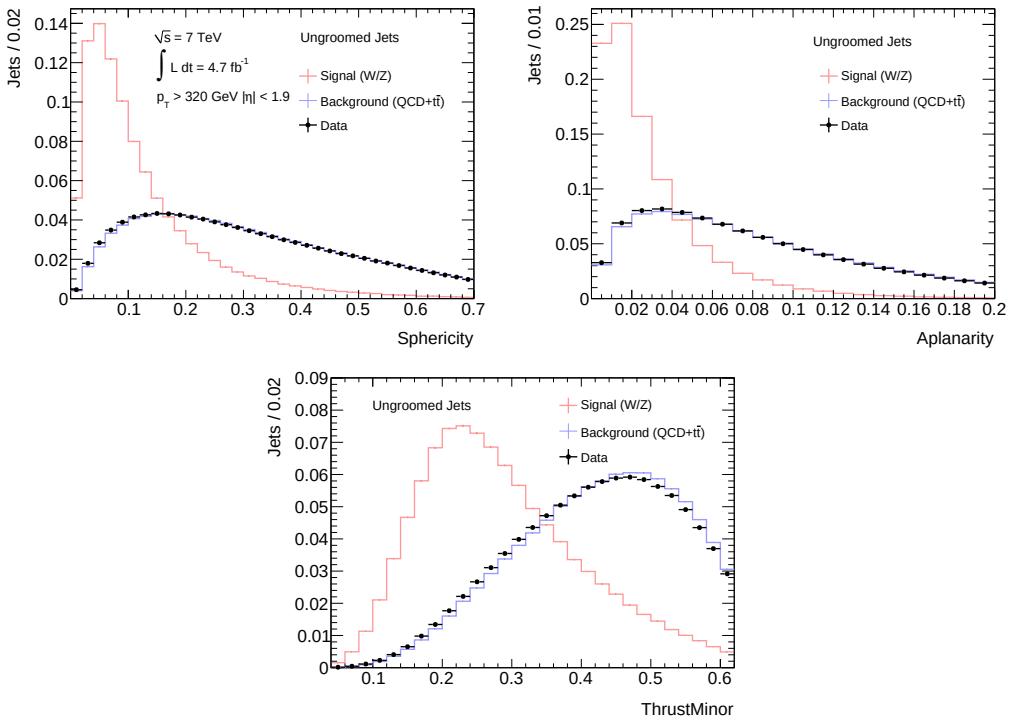

Figure 8.3.: The distribution of the shapes in signal and background MC and data.

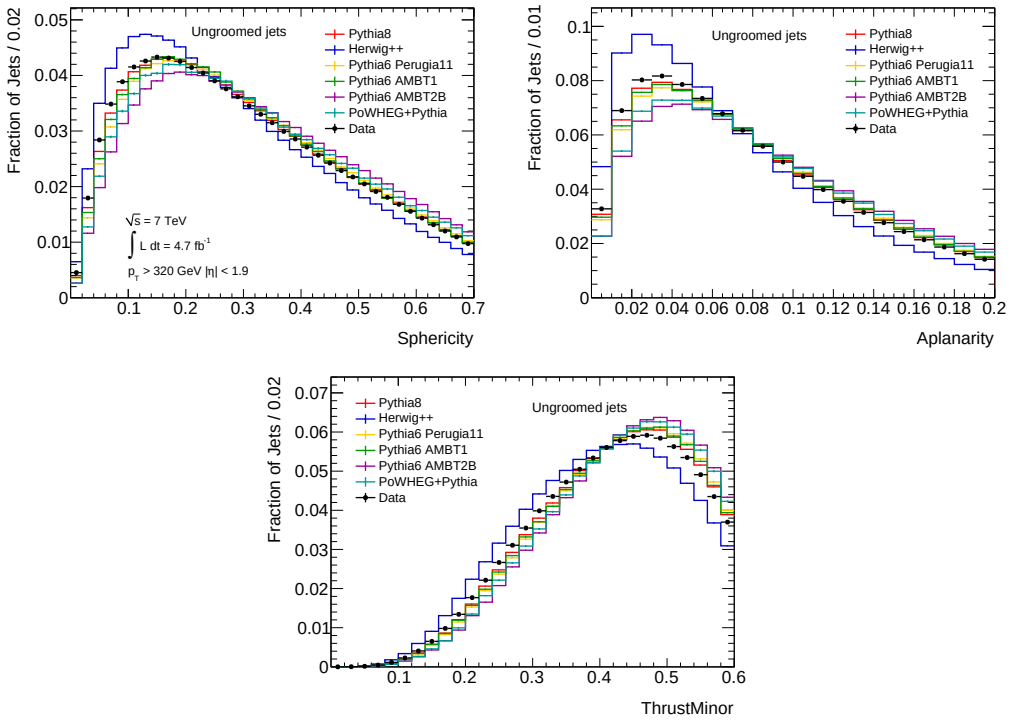

Figure 8.4.: The distribution of the shapes comparing data to the various background MC simulations.

8.3.3. Jet Shape based Likelihood Function

The final cut on the jet shapes in the centre of mass frame is performed using a likelihood combining the sphericity, aplanarity and thrust minor. It is defined as

$$LH(i) = \frac{\mathcal{L}_S(i)}{\mathcal{L}_S(i) + \mathcal{L}_B(i)} \tag{8.5}$$

where

$$\mathcal{L}_{S(B)}(i) = \prod_{k=1}^{n_{var}} p_{S(B),k}(x_k(i)) \tag{8.6}$$

The variables entering the likelihood are, as expected, quite correlated, but by combining them in a likelihood some additional discrimination can be gained and the background shape also remains smoother. The distribution of the likelihood for signal, background and data can be seen in Figure 8.5 as well as the comparison to the various background MCs studied.

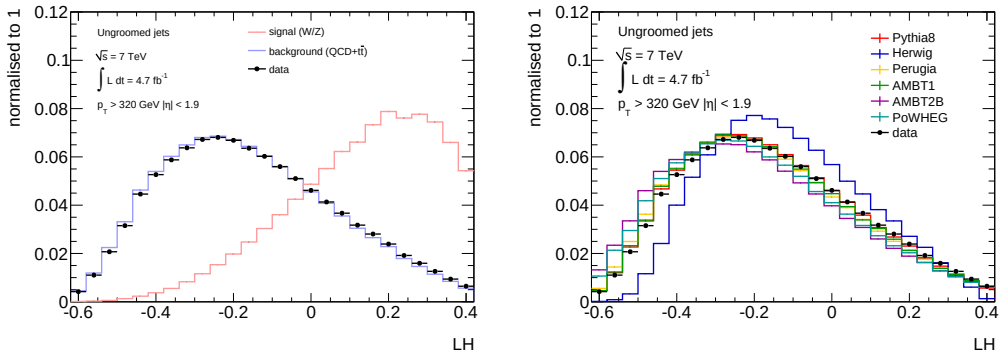

Figure 8.5.: The distribution of the LH in signal and background MC and data (left) and comparing data to the various background MC simulations (right).

The final cut on the likelihood was chosen to maximise the significance of the signal, using the measure $S/\sqrt{S+B}$ where S is the number of signal jets and B the number of background jets given by the MC after all the cuts and in the mass window $50 < m_{jet} \leq 150$ GeV. This results in a likelihood cut of $LH > 0.15$, producing a background rejection of 89.2% and a signal efficiency of 56.2% based on the default Herwig signal MC and Pythia 8 background MC.

8.4. Hadronically Decaying W/Z Boson Cross Section Measurement

8.4.1. Extraction of the signal yield

The signal yield is found using a maximum likelihood fit to the jet mass distribution in data. To do this the various contributions to the jet mass distribution need to be accounted for: the QCD jet background, $t\bar{t}$ events, single top and diboson processes and the signal contribution.

QCD background Model

The QCD background contribution is modelled using an analytical function which is developed based on the shape shown in the various MC samples and tested using a signal-depleted data sample. This is sample is generated by considering the jet

with a lower value of the likelihood in events with more than one jet passing and by cutting on the jet p_T balance to reduce the signal, a variable which is shown to be uncorrelated with mass. The shape of the background in MC is not necessarily the same as the one found in data, hence the parameters of the function are allowed to float when the fit to the data is performed. The function used is

$$S_{QCD}(m_{jet}) = f_E E(m_{jet} : m_0, \sigma_m) + f_1 C_1 \exp(a_1 m_{jet}) + (1 - f_E - f_1) C_2 \exp(a_2 m_{jet}) \tag{8.7}$$

where $E(m_{jet} : m_0, \sigma_m)$ is the sigmoid function,

$$E(m_{jet} : m_0, \sigma_m) = \frac{1}{1 + \exp(-m_{jet})} \tag{8.8}$$

C_1 and C_2 are normalisation factors and f_E, m_0, σ_m, f_1, a_1 and a_2 are free parameters which are allowed to float in all fits. The sigmoid function is used because the background distribution has a shoulder shape, although there are other functions that could be used to model this also.

To check this function successfully models the background mass distribution it is tested on those produced by each of the different MC simulations and found to model each one well. It is also tested on the background mass distributions obtained when the cuts on the likelihood distribution and the jet p_T are varied, as well as the spectrum from jets reconstructed with different jet radii. The function describes all these different distributions well and hence should also be able to model the data. The changes in the parameters using the different selection criteria are consistent between MC and data.

Contribution from the $t\bar{t}$ Background

The second largest contribution to the background, although small in comparison to QCD, are $t\bar{t}$ events. This contribution is simply modelled using the histogram produced by the MC simulation, normalised according to the cross section predicted by the MC and the luminosity in data. The distribution in Figure 8.6 shows a clear peak in the signal region and an additional contribution at higher masses, where the b-jet is also contained within the jet.

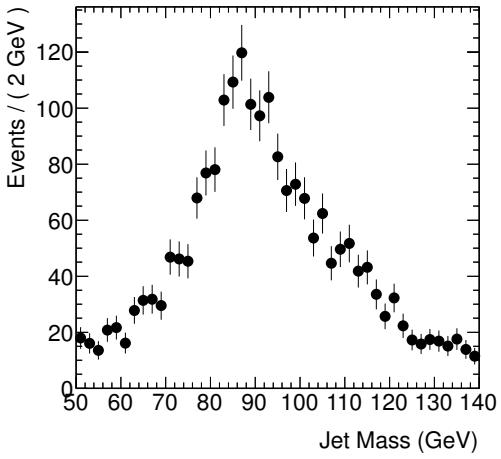

Figure 8.6.: The distribution of the jet mass from $t\bar{t}$ MC samples normalised to the data luminosity.

Contribution from the Single Top Background

The distribution, based on MC, from the single top background is shown in Figure 8.7, normalised to the luminosity in data using the MC cross section. It can be seen that it is only the Wt channel that contributes to the background, although this amounts to a very small number of events and hence it is not accounted for in the fit, but instead subtracted from the signal yield.

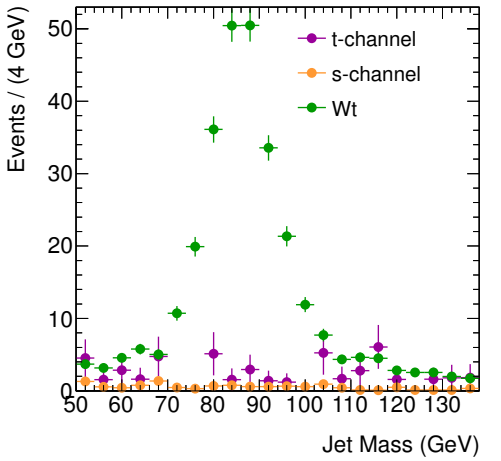

Figure 8.7.: The distribution of the jet mass from single top MC samples normalised to the data luminosity.

Contributions from Other Backgrounds

Additional sources of background were also considered, such as that from diboson production (WW, WZ, ZZ, $W\gamma$, $Z\gamma$). Although these do contain W bosons they are considered background as the cross section measurement is only for W + jets production. This contribution is tiny, but as it peaks in the same place as the signal, again the signal yield is corrected by subtracting it at the end. The distribution from MC is shown in Figure 8.8.

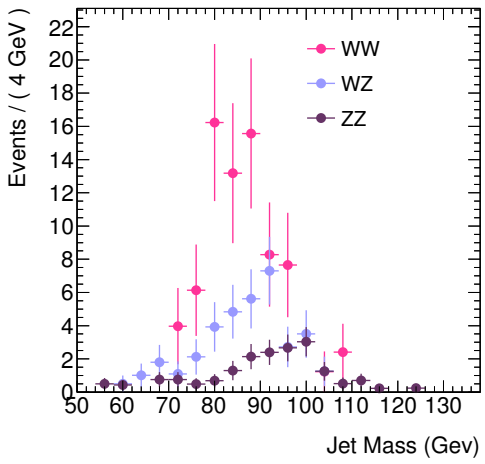

Figure 8.8.: The distribution of the jet mass from diboson MC samples normalised to the data luminosity.

W/Z Signal Mass Distribution

The signal distribution is modelled using a Breit-Wigner function convoluted with a gaussian for each the W and Z distribution

$$S_W(m_{jet}) = F_{BW}(m_{jet} : m, \Gamma_W) \otimes G(m_{jet} : m, \sigma_W) \tag{8.9}$$

$$S_Z(m_{jet}) = F_{BW}(m_{jet} : m, \Gamma_Z) \otimes G(m_{jet} : m, \sigma_Z) \tag{8.10}$$

where the Breit-Wigner function is

$$F_{BW}(m : \bar{m}, \Gamma) = \frac{1}{2\pi} \frac{\Gamma}{(m_{jet} - \bar{m})^2 + \Gamma^2/4} \tag{8.11}$$

and the Gaussian function is

$$G(x : \bar{x}, \sigma) = \frac{1}{\sigma\sqrt{2\pi}} \exp\left[-\frac{(x-\bar{x})^2}{2\sigma^2}\right] \tag{8.12}$$

This fit is first performed on the MC with all the parameters free to float except the W and Z widths, which are fixed to the PDG values [63]. The resulting pole masses of the W and Z are shifted by 5 GeV and 4 GeV respectively with respect to the PDG values, as expected due to contributions from other sources such as pileup and the underlying event. The fit to MC is shown in Figure 8.9, where it does a reasonable job of describing the shape of the distributions, although it doesn't capture all the details.

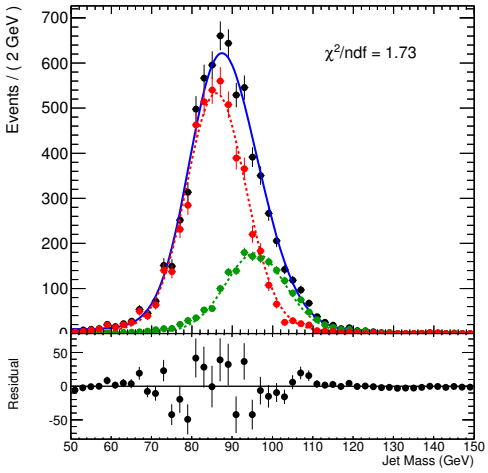

Figure 8.9.: The result of the fit to the signal MC where the green is the Z contribution, the red is the W contribution and the blue is the total found by summing the two.

For the fit to the data the pole masses are reparameterised as

$$\bar{m_W} = m_W + m_W^{\text{offset}} \tag{8.13}$$

$$\bar{m_Z} = m_W + \Delta m_{WZ} + m_Z^{\text{offset}} \tag{8.14}$$

where m_W is the pole mass of the W boson, Δm_{WZ} is the pole mass difference between the W and Z and $m_{W(Z)}^{offset}$ is the difference between the reconstructed W (Z) mass and its PDG value. This parameterisation of the mass allows for direct comparison of the W boson pole mass to the PDG value. In the data fit, m_W and Δm_{WZ} are fixed to the PDG values , $m_W = 80.385 \pm 0.015$ GeV, $\Delta m_{WZ} = 10.803 \pm 0.015$ GeV and

$m_{W(Z)}^{offset}$ is fixed to the value predicted by the MC. The detector resolutions, $\sigma_{W(Z)}$, are also fixed to the values predicted by the MC.

Maximum Likelihood Fit

The final fit is done using a maximum likelihood fit defined by

$$\mathcal{L} = \prod_{i=1}^{n} \{f_{sig}[f_W S_W + (1 - f_W)S_Z] + f_{t\bar{t}} S_{t\bar{t}} + (1 - f_{sig} - f_{t\bar{t}})S_{QCD}\}_i \qquad (8.15)$$

where f represents the fraction of events, S represents the probability distribution function obtained for each contribution and n is the total number of jets selected.

The various parameters associated with the fit are summarised in Table 8.2 and the parameters obtained as a result of the fit are shown in Table 8.3. This gives a final result for the number of W and Z signal events

$$N_{W^\pm} + N_{Z^0} = 14555 \pm 1334 \qquad (8.16)$$

The mass distribution from data is shown in Figure 8.10. The fit has a χ^2 probability of about 30%. The fit was repeated with the background models only which results in a distribution inconsistent with the data, showing a significant excess in the signal region with a χ^2 probability of 5×10^{-16}, significantly worse than with the signal PDF included.

The systematic uncertainties due to the QCD background PDF, the signal PDF, the other sources of background and the jet mass scale and resolution are considered and summarised in Table 8.4. There is more detail on the calculation of these in Appendix A. The final result obtained is

$$N_{W^\pm} + N_{Z^0} = 14188 \pm 1334(\text{stat.}) \pm 2439(\text{syst.}) \qquad (8.17)$$

name	Description	Comments
Signal		
f_{sig}	Combined signal fraction	Free parameter
f_W	Relative fraction of W-jets of signal yield	Fixed to MC prediction
m_W	W boson pole mass	Fixed to PDG value
Δm_{WZ}	pole mass difference between W and Z	Fixed to PDG value
$m_{W(Z)}^{offset}$	difference between reconstructed and PDG W (Z) mass	Fixed to MC prediction
Γ_W	Intrinsic width W boson	Fixed to PDG value
Γ_Z	Intrinsic width Z boson	Fixed to PDG value
σ_W	Detector resolution of reconstructed W mass	Fixed to MC prediction
σ_Z	Detector resolution of reconstructed Z mass	Fixed to MC prediction
QCD		
f_{E}	Fraction of the sigmoid component in QCD PDF	Free parameter
f_1	Fraction of the first exponential component in QCD PDF	Free parameter
m_0	Inflection point of the Sigmoid function in QCD PDF	Free parameter
σ_m	Curvature at inflection point of the Sigmoid function in QCD PDF	Free parameter
a_1	Slope of the first exponential component in QCD PDF	Free parameter
a_2	Slope of the second exponential component in QCD PDF	Free parameter
Other background		
$f_{t\bar{t}}$	Fraction of $t\bar{t}$ background	Fixed to MC prediction

Table 8.2.: List of parameters used in the default fit.

name	Fitted result
f_{sig}	0.024644 ± 0.00226
f_{E}	0.88 ± 0.02
f_1	0.055 ± 0.0038
m_0	$109.8 \pm 0.22\,\text{GeV}$
σ_m	$21.99 \pm 0.52\,\text{GeV}$
a_1	-0.1513 ± 0.0082
a_2	-0.0110 ± 0.0044

Table 8.3.: Summary of the fitted values of the free parameters used in the default fit.

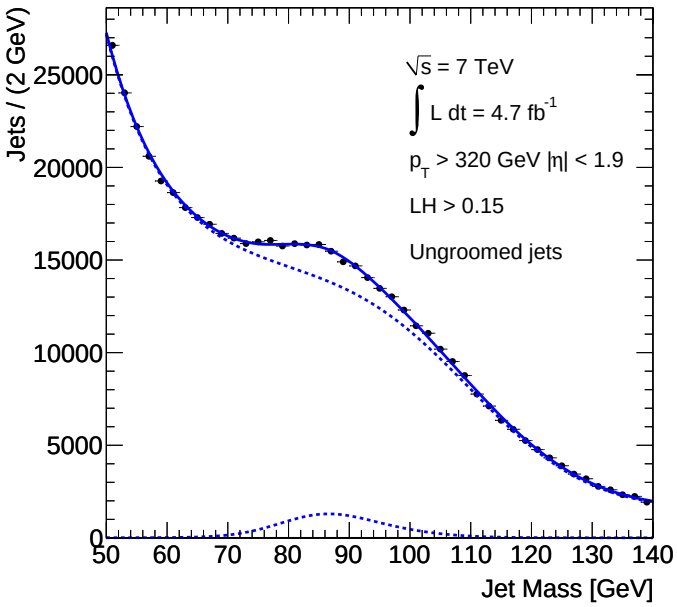

Figure 8.10.: The final result of the fit to the data showing the extracted signal.

Sources	$N(W^{\pm}) + N(Z^0)$
Fit bias	1.7 %
Signal PDF uncertainty	5 %
Background PDF uncertainty	8.8 %
Jet mass scale	2.2 %
Jet mass resolution	12.6,%
$t\bar{t}$ contribution	1.34 %
Single top contribution	< 1 %
Di-Boson contribution	< 1 %
Total	16.4 %

Table 8.4.: Summary of the relative systematic uncertainties of the $W^{\pm} + Z^0$ jet signal yields from different sources.

8.4.2. Extraction of the Hadronically Decaying W/Z Cross Section

The cross section is calculated using the relation

$$\sigma(W^{\pm} \to qq + Z^0 \to qq) = \frac{N^{reco}_{W^{\pm}} + N^{reco}_{Z^0}}{\epsilon_{W^{\pm}/Z^0}\mathcal{L}} \tag{8.18}$$

where $N^{reco}_{W^\pm} + N^{reco}_{Z^0}$ is the signal yield from the data, $\mathcal{L}$ is the luminosity and $\epsilon_{W^\pm/Z^0}$ is the signal reconstruction efficiency, which is calculated based on Herwig signal MC using

$$\epsilon_{W^\pm/Z^0} = \frac{N^{reco}_{W^\pm+Z^0}(p_T^{reco} > 320GeV, |\eta^{reco}| \leq 1.9, m_{jet} > 50GeV, LH > 0.15)}{N^{gen}_{W^\pm+Z^0}(p_T^{gen} > 320GeV, |\eta^{gen}| \leq 1.9)} \tag{8.19}$$

$N^{gen}_{W^\pm+Z^0}$ is the signal yield from the MC at truth level. The result is $\epsilon_{W^\pm/Z^0} = 0.36 \pm 0.02$, where the uncertainty is only statistical. The cross section for just the $W^\pm$ can be calculated using

$$\sigma(W^\pm) = \frac{f_W^{MC}(N^{reco}_{W^\pm} + N^{reco}_{Z^0})}{Br(W^\pm \to qq)\epsilon_{W^\pm}\mathcal{L}} \tag{8.20}$$

where Br is the branching ratio for hadronic decays of the W. The efficiency in this case is calculated using

$$\epsilon_{W^\pm} = \frac{N^{reco}_{W^\pm}(p_T^{reco} > 320GeV, |\eta^{reco}| \leq 1.9, m_{jet} > 50GeV, LH > 0.15)}{N^{gen}_{W^\pm}(p_T^{gen} > 320GeV, |\eta^{gen}| \leq 1.9)} \tag{8.21}$$

which produces the result $\epsilon_{W^\pm} = 0.37 \pm 0.02$ from the Herwig signal MC.

The systematics on the measured cross section are calculated considering contributions from the measurement of the signal yield, the calculation of the signal efficiency, the uncertainty on the branching ratio, the theoretical contribution and the luminosity which are discussed in more detail in Appendix A. These are summarised in Table 8.5. The main systematic error comes from the uncertainty on the mass resolution when extracting the signal yield, which could be improved with further study and more data using $t\bar{t}$ events in data.

The final production cross section obtained for boosted $W^\pm$ and Z^0 bosons with $p_T \geq 320$ GeV and $|\eta| \leq 1.9$ in pp collisions at a centre of mass energy $\sqrt{s} = 7$ TeV is

$$\sigma(W^\pm/Z^0 \to qq : p_T > 320 \text{ GeV}, |\eta| < 1.9) = 8.5 \pm 0.8(\text{stat.}) \pm 1.5(\text{syst.}) \text{ pb} \tag{8.22}$$

$$\sigma(W^\pm : p_T > 320 \text{ GeV}, |\eta| < 1.9) = 8.6 \pm 0.8(\text{stat.}) \pm 1.5(\text{syst.}) \text{ pb} \tag{8.23}$$

Sources	$\sigma(W^{\pm} + Z^0)$
Signal yield	16.4 %
data/MC difference	4.4 %
Jet energy scale	3.7 %
Jet energy resolution	0.3 %
MC statistics	0.57 %
Luminosity	1.8 %
Theoretical	2.9 %
Total	17.7 %

Table 8.5.: Summary of the relative systematic uncertainties of the measured $W^{\pm}$ and Z^0 production cross sections from different sources.

which is found to be about 1.9 standard deviations higher than the theoretical prediction from MCFM of [1]

$$\sigma(W^{\pm}/Z^0 \to qq : p_T > 320\text{GeV}, |\eta| < 1.9) = 5.1 \pm 0.5\text{pb} \tag{8.24}$$

8.5. Jet Substructure and Grooming Studies

Different techniques have been developed to try and mitigate the effect of pileup and the underlying event on jets and leave behind only the interesting hard structure. The techniques considered here are splitting and filtering [64], pruning [47, 65] trimming [66] and area subtraction [67].

[1] As mentioned in the introduction the nature of working in a large collaboration is that analyses are performed in groups. In this analysis I must mention Francesco de Lorenzi specifically for the huge amount of work he did here

8.5.1. Description of the Grooming Techniques

Splitting and Filtering

The splitting and filtering algorithm aims to identify and keep the hard structure in a jet that might be produced by the two-body decay of a high p_T heavy object by looking for concentrations of energy within a jet. It was designed and optimised for a search for a Higgs boson decaying to $b\bar{b}$ in the final state when it is produced in association with a vector boson in the boosted regime [64]. The Cambridge-Aachen algorithm is used to reconstruct the original jet because it performs the clustering based only on angular distances, with the largest distances clustered last. This means that undoing the last step of the clustering procedure wide splittings within a jet can be looked for, while keeping flexibility over the actual scale of this splitting.

The algorithm can be divided into two parts, the splitting which tries to identify jets which have a two-body-like structure and the filtering which aims to keep the parts of the jet associated with this decay while throwing away contributions from pileup and the underlying event.

The splitting procedure uses iterative decomposition of the jet looking to identify a symmetric splitting which could be caused by a boosted heavy particle decay. This is done starting with the jet, j, and undoing the last step of the clustering to form two subjets j_1 and j_2 ordered in mass such that $m_{j_1} > m_{j_2}$. These subjets must then pass two criteria: the mass-drop and a symmetry cut. The mass-drop requirement is that

$$\frac{m_{j_1}}{m_{jet}} < \mu \tag{8.25}$$

where m_{jet} is the original jet mass and μ is a parameter of the algorithm. This cut ensures there is a large enough decrease in mass. The symmetry cut is

$$y_f = \frac{min(p^2_{T_{j_1}}, p^2_{T_{j_2}})}{m^2_j} \Delta R^2_{j_1,j_2} > y_{cut} \tag{8.26}$$

which is a measure of how evenly the energy is split between the two subjets. Applying the fact that $\Delta R \sim \frac{2m_X}{p_T}$ shows that this is essentially a cut on the minimum fraction

of the p_T that must be carried by the lower p_T subjet, or on the ratio between the transverse momenta of the two subjets.

If these criteria are passed, the jet is a potential two-body decay and so passes the splitting. If the cuts are not passed then j_1 is relabelled as j and the procedure repeated.

The choice of the values of the parameters has been optimised for the case of the $H \to b\bar{b}$ boosted higgs search. The choice for μ is guided by the fact that to allow for gluon radiation, $V \to q\bar{q}g$, and still pass this mass drop requirement the value of μ should be $\mu \gtrsim 1/\sqrt{3}$. The standard value of 0.67 is chosen to be slightly higher than this. For the choice of y_{cut}, the value that maximises the significance, measured using $S/\sqrt{B}$, where the background comes from mistagged light jets is $y_{cut} \simeq 0.15$. The value that is optimised for the higgs search is $y_{cut} = 0.09$, which is used in this analysis.

The second part of the procedure is the filtering, which tries to remove the parts of the jet thought to come from the underlying event or pileup, but keep the part belonging to the decay of the boson contained within the jet. This is done by reclustering the jet with a smaller jet radius based on the angular scale of the splitting , $R_{filt} = min(0.3, \Delta R_{j_1,j_2}/2)$, such that the decay products have their own jets. From this only the three hardest jets are kept, aiming to capture the quarks and potential gluon radiation. The steps in this procedure are summarised by Figure 8.11.

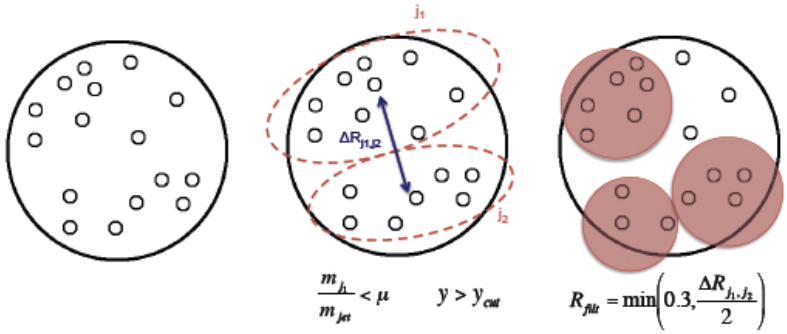

Figure 8.11.: A visual representation of the splitting and filtering technique. The final jet is the sum of the three jets in red at the last stage.

Jet Trimming

Jet trimming is a process designed to throw away the parts of a jet coming from the initial state radiation, multiple parton interactions and pileup while keeping the parts that come from the hard scatter, so includes those from the final state radiation. The process was designed with QCD jets in mind, but it should improve the jet reconstruction for all jets. The idea is that a larger jet radius is preferable to properly capture all the final state radiation, however to mitigate the effects of the underlying event and pileup a smaller jet radius is better. The ideal would be to reconstruct with a large jet radius and then remove the extra contributions. As the underlying event and pileup are generally much softer than the the particles coming from the hard scatter, trimming attempts to find these softer groups of calorimeter cells and remove them from the jet.

The process starts by clustering the event into jets using any clustering algorithm to produce seed jets. Each seed jet is then reclustered using the k_T-algorithm with a smaller jet radius, R_{sub}, to produce a number of subjets. A subjet, i, is discarded if it doesn't satisfy the p_T cut:

$$\frac{p_{T_i}}{p_{T_{jet}}} < f_{cut} \tag{8.27}$$

The remaining subjets form the final jet. This is shown pictorially in Figure 8.12.

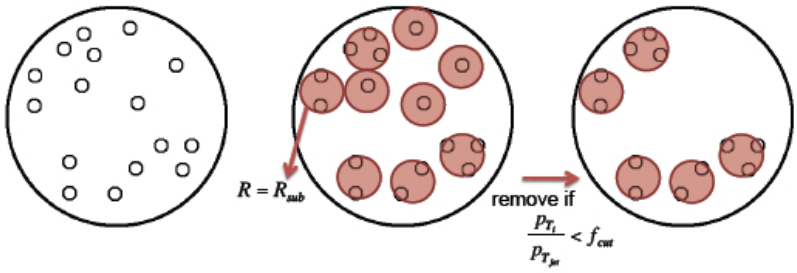

Figure 8.12.: A visual representation of the trimming technique.

The k_T-algorithm is the most suitable choice for the reclustering because it forms jets starting with the softest and ending with the hardest clusters. This leads to more equal sharing of energy between the subjets so in the case that the final state

radiation from the hard scatter cannot be contained within a single subjet it will be split more evenly between several, and hence not accidentally discarded.

This process tends to have the largest impact on low mass jets produced by a light-quark or gluon, which can lose up to about 50% of their mass while the jets containing the hadronic decay of a boosted boson are less affected. The parameters that were found to be optimal for this process, based on the largest improvement to a resonance mass peak, were $f_{cut} = 0.03$ and $R_{sub} = 0.2$.

Jet Pruning

Jet pruning is similar to trimming in that it also attempts to remove the part of the jets which are thought to come from pileup or the underlying event, but using a slightly different method. It was developed to help improve the mass resolution in searches for generic boosted heavy object decays contained within a single jet, hence improving the likelihood of seeing new resonances. That said, the process should work to remove these contributions in any jet and doesn't actually look to identify the jets containing a boosted heavy object decay.

Pruning is a "bottom-up" technique, which removes the soft and large angle contributions to the jet during the clustering process. The jets are first created using any clustering algorithm. The constituents of a jet are then reclustered using either the k_T- or Cambridge-Aachen algorithm (with a larger radius so as to contain all the constituents). At each stage in the clustering process the two constituents being merged, $1, 2 \rightarrow j$, must satisfy two criteria. The first ensures the constituent is hard enough, so has a high enough p_T with respect to that of the initial jet:

$$\frac{min(p_{T_1}, p_{T_2})}{p_{T_j}} < z_{cut} \tag{8.28}$$

The second requirement rejects large angle constituents:

$$\Delta R_{12} > R_{cut} \times \frac{2m_j}{p_{T_j}} \tag{8.29}$$

If either of these two conditions are not met, the softer of these constituents is removed, otherwise they are merged. Then the clustering continues. This is shown in Figure 8.13.

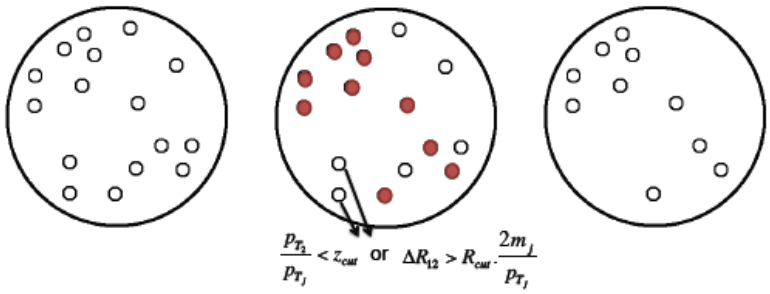

Figure 8.13.: A visual representation of the pruning technique.

Both of these cuts can be adjusted and must be chosen so as not to start removing the hard component of the jet, but so they are large enough that they have an effect. The values that are recommended based on performance are $z_{cut} = 0.15$ and $R_{cut} = 0.5$. This method has the advantage that it is part of the formation of the jet rather than based on forming subjets and quantities from the jet once already formed.

Area Subtraction

Area subtraction, although not strictly a grooming technique, reduces the momentum of a jet by the amount which is thought to have come from pileup and the diffuse underlying event. It does this by subtracting an average correction calculated on an event-by-event basis in an entirely data driven technique. The amount that is subtracted varies from jet to jet based on its area.

There are several different definitions of the jet area [68], all based on introducing infinitely soft ghost particles to the event and seeing where they cluster: the passive area, the active area and the Voronoi area. The passive area is calculated by adding a single ghost particle to the event and considering which jet it gets clustered into. Providing an infrared safe jet algorithm is used this won't affect the clustering of jets in any way. The space around a jet for which this ghost particle gets clustered into it then gives its area.

The k_T algorithm is a special case because the ghost particle, being infinitely soft, will always get clustered with a particle first (unless there isn't one within a distance R). This means that an area for each particle in the event can be determined.

In fact the whole event can be divided into cells where for all positions in a cell the corresponding particle is the closest one, or the ghost will be clustered with that particle. This is known as a Voronoi diagram and leads to the definition of the Voronoi area of the particle as the intersection of this Voronoi cell with a circle of radius R centred on the particle. The Voronoi area of a jet is then the sum of the particle Voronoi areas. For the k_T algorithm this gives the same as the passive area, but this can also be used for other jet algorithms despite not being directly understandable in terms of ghost particle clustering.

Another way of calculating the area of a jet, known as the active area, is by introducing a dense background of ghost particles and reclustering the jets with these included. The area of a jet, A is then defined by counting the number of these ghosts in a jet, $\mathcal{N}_g$, and using their density, ν_g

$$A(J|\{g_i\}) = \frac{\mathcal{N}_g}{\nu_g} \tag{8.30}$$

However, because this area will vary depending on the exact distribution and density of the ghost particles to get a consistent value this must be averaged over many different ghost selections and the limit of infinite density of ghost particles taken

$$A(J) = \lim_{\nu_g \to \infty} \langle A(J|\{g_i\}) \rangle \tag{8.31}$$

The contribution that must be subtracted from each jet is the average contribution of pileup. In each event it is expected that aside from the jets produced by the hard scatter there will many produced by pileup and so these can be used to calculate the expected contribution on an event by event basis. Each of these pile up jets should give about the same value of ρ, the contribution of pileup to the p_T per unit area, with fluctuation as pileup is not exactly uniformly distributed. So this value can then be calculated using

$$\rho = \text{median}\left[\left\{\frac{p_{T_j}}{A_j}\right\}\right] \tag{8.32}$$

where the median has been used so that the value is not strongly affected by the jets coming from the hard scatter. It is clear that for this to be correct the number of pileup jets must be far greater than the number coming from the hard scatter. It

is also the case that the jets used to calculate this must have a radius larger than the separation between pileup particles so that the jets cover the whole area, leaving little empty space, otherwise the median may be due to these areas of empty space rather than the pileup of interest. However, in the extreme LHC conditions it is almost guaranteed that these conditions will both be satisfied.

Based on this the transverse mometum of a jet can be adjusted for pileup using

$$p_{T_j}^{sub} = p_{T_j} - A_j \rho \tag{8.33}$$

relying on the pileup contribution being independent of where a jet is located in the detector. If this varies then the average contribution is no longer an appropriate measure.

8.5.2. Study of Grooming after the Standard Selection

None of the techniques described can be used to pick out a boosted hadronically decaying W/Z boson from the QCD background when applied alone, however, the peak produced by the cutting on jet shapes in the centre of mass frame can be used to study the effect of these various grooming techniques. When considering each techniques three main points were considered: the agreements between the data and the MC; the dependence of the mass on pileup; the improvement to the significance of the result in terms of S/B and $S/\sqrt{S+B}$.

Splitting and Filtering

The anti-k_T R=0.6 jets that pass the selection cuts described for the cross section measurement are then passed through the splitting and filtering technique with the standard parameters ($\mu = 0.67$ and $y = 0.09$) [64]. As this techniques is based on the Cambridge-Aachen algorithm the events are first reclustered, using a radius of $R = 1.2$ as for the standard splitting and filtering. The jet that is most closely matched geometrically to the anti-k_T jet is then passed through the splitting and filtering procedure and the mass of this resulting jet is used.

It is worth noting that the cut on the jet shapes as well as the p_T and η is based on the ungroomed anti-k_T jet, such that the jets in the distribution should be the same

ones and so a direct comparison can be made. Calculating the likelihood from jet shapes based on the Cambridge-Aachen jets was considered, but the discrimination between signal and background in this case was much worse.

The mass distribution obtained is shown in Figure 8.14, in both data and signal MC. These plots show that much of the background is thrown away by applying this process, but most of the signal is retained. This results in an improvement in signal to background ratio, however, the loss of background jets comes mostly from the low mass region leaving a peaking structure in the background mass distribution. This peak lies under the signal which makes signal extraction more difficult. Further investigation shows that this is an unfortunate coincidence due to the combination of the jet radius and the p_T cut, as shown in Figure 8.15, where the distribution is split into different p_T bins. Although this algorithm is not much use in this case it may well be useful in other analyses, such as searches for heavier states, as shown in the next section.

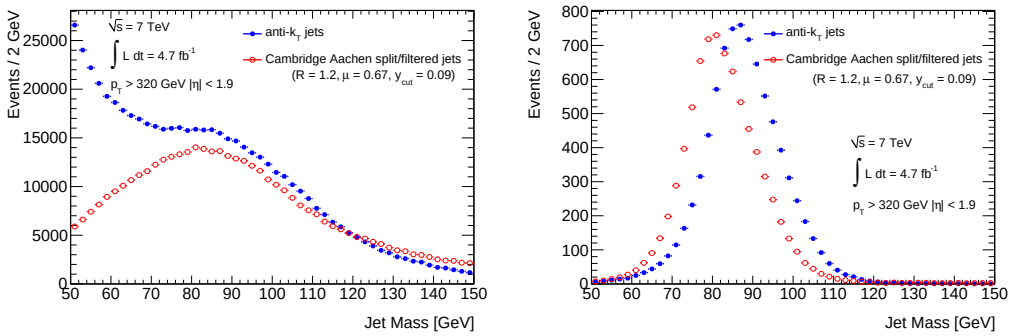

Figure 8.14.: The invariant mass distribution in data (left) and signal MC (right) for jets passing the standard LH selection based on ungroomed anti-k_T jets then reclustered with the Cambridge-Aachen algorithm and passed through the splitting and filtering criteria

A general shift to lower mass is observed as a result of applying the splitting and filtering technique, which can be seen clearly in the signal mass distribution. This is an expected consequence due to parts of the jet being removed. The resulting mass distribution comparing data and MC is shown in Figure 8.16, after both the standard and a harsher cut have been made on the likelihood. The harsher cut of $LH > 0.25$ is chosen to reject about 95% of the background with a signal efficiency of 35.7%.

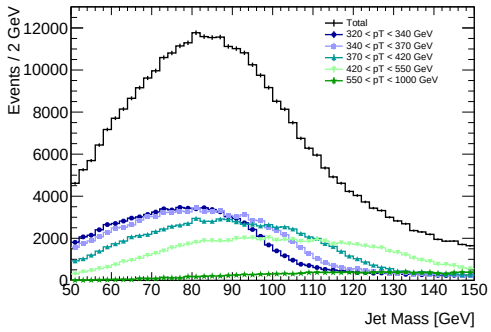

Figure 8.15.: The mass distribution after the standard likelihood selection and after the splitting and filtering process has been applied, in data, split into four p_T bins.

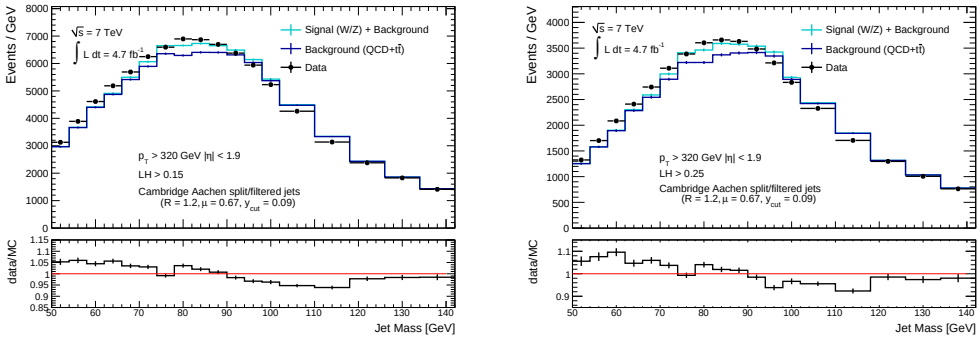

Figure 8.16.: The mass distribution comparing data and MC after applying the splitting and filtering technique to jets passing both the standard likelihood cut (LH $>$ 0.15, left) and a harsher cut (LH $>$ 0.25, right).

As the splitting and filtering technique actively looks for hard structure within a jet it is possible to tighten the selection cut to obtain a similar background rejection as the likelihood cut. This was done by increasing the value of y_{cut} to 0.35 which provides a background rejection of about 90% with a signal efficiency of 43%. So for the same background rejection this performs slightly worse in terms of signal efficiency. The distribution obtained is shown in Figure 8.17 which shows the background is still distorted making signal extraction more difficult.

Pruning and Trimming

The jets passing the standard likelihood selection were also groomed using the pruning and trimming algorithms. Once again all the cuts here are based on the ungroomed jets and the grooming is done after this selection. There are several

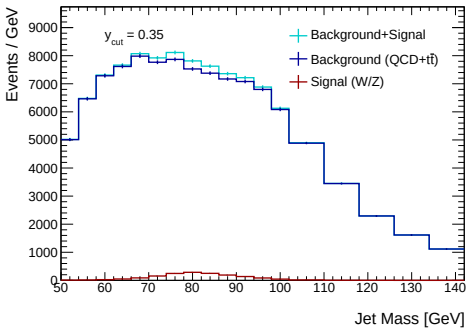

Figure 8.17.: The mass distribution in MC after the splitting and filtering technique is applied with $y_{cut} = 0.35$

tuneable parameters for these grooming techniques and so as to study the full potential of these algorithms, 6 different sets of parameters were considered for each technique, as summarised in Table 8.6.

	Trimming		Pruning	
	R_{sub}	f_{cut}	R_{cut}	z_{cut}
1	0.2	0.05	0.3	0.05
2	0.2	0.03	0.2	0.05
3	0.2	0.01	0.1	0.05
4	0.3	0.05	0.3	0.1
5	0.3	0.03	0.2	0.1
6	0.3	0.01	0.1	0.1

Table 8.6.: Parameters used for the pruning and trimming algorithms

To initially assess how each of these different parameter sets performs the shape of the background distribution was produced and the signal to background ratio was calculated. As the signal peak shifts to lower mass this ratio was plotted as a function of the jet mass, as shown in Figure 8.18. This figure also shows the significance, by calculating the ratio of the signal to the square root of the signal and background.

The signal to background ratio is not affected much by applying grooming, although a slight improvement can be achieved. The same behaviour can be seen in the significance plots. Looking at the distributions of the background masses, the level of the background remains about the same in the signal region using either

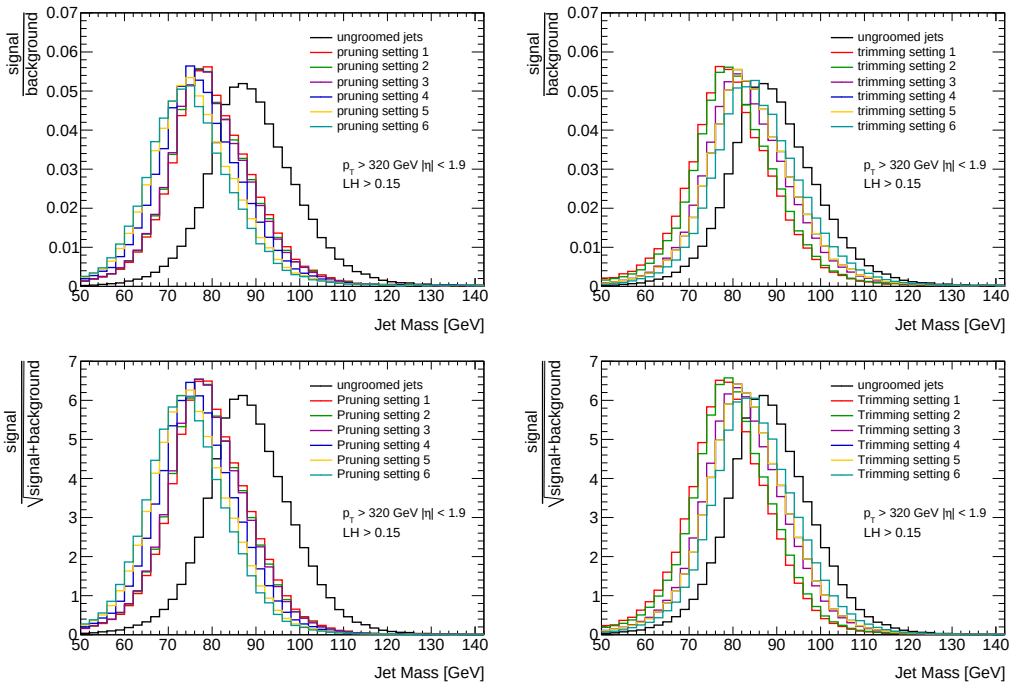

Figure 8.18.: The distribution of signal over background (top) and signal over the square root of the background (bottom) as a function of the mass after the jets passing the standard likelihood selection have been pruned (left) and trimmed (right) with the comparison to the ungroomed case. The value is calculated in each mass bin using the standard signal and background MC.

technique and the small improvement that can be gained in signal over background is mostly due to the narrowing in the signal peak. These plots also highlight the general shift to lower masses caused by grooming.

Based on this information and the background distributions produced, for each algorithm one set of parameters was chosen to perform further studies. These produce the best improvement in signal over background while not influencing the shape of the background much. For trimming theses values are $R_{sub} = 0.2$ and $f_{cut} = 0.03$, and for pruning $R_{cut} = 0.3$ and $z_{cut} = 0.05$, although the performance between the different parameter sets was not too different.

The resulting mass distribution for this choice of parameters is shown in Figure 8.19 for pruning and Figure 8.20 for trimming. These both show one plot for the standard likelihood cut and one with a harsher likelihood cut, $LH > 0.25$, chosen, as for the splitting and filtering, to reject about 95% of the background. The number of jets in these distributions is reduced compared to the ungroomed case, despite the

same selection being applied, because some of the jets are shifted out of the mass window. These plots also show that the background distribution is affected and becomes slightly more peaked in the signal region. The agreement between data and MC in these plots, as shown by the ratio plots at the bottom, is preserved after grooming with deviations generally less than 5% until the higher masses where deviations increase to about 10% in both cases. This discrepancy between signal and background does not affect the signal extraction as the background is not taken from the MC, rather the fit parameters are all free to float.

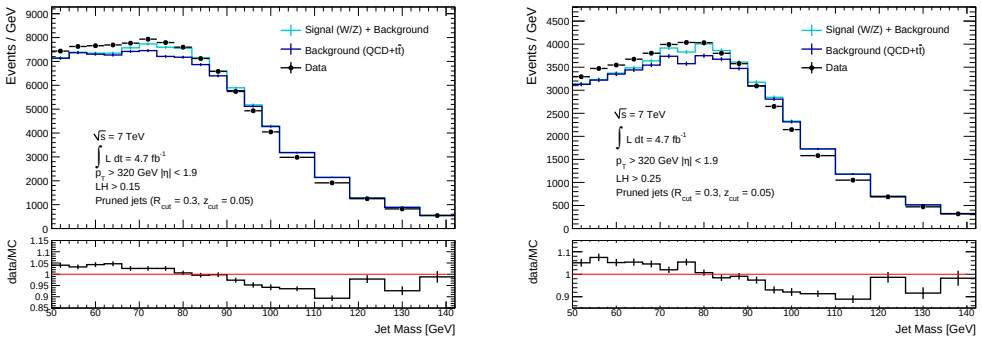

Figure 8.19.: The mass distribution comparing data and MC for jets passing the standard likelihood selection (left) and a harsher cut on the likelihood (right) that have then been pruned.

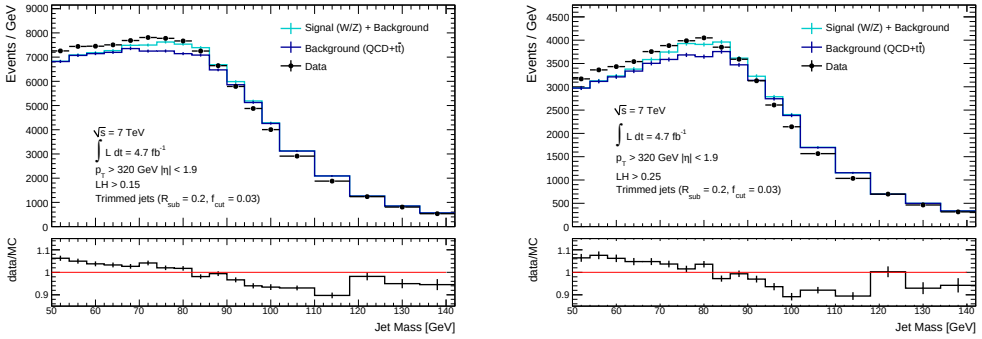

Figure 8.20.: The mass distribution comparing data and MC for jets passing the standard likelihood selection (left) and a harsher cut on the likelihood (right) that have then been trimmed.

Area Subtraction

As for the other techniques, area subtraction was also applied to the jets selected by the likelihood selection, using both the active and the Voronoi area definitions.

The resulting mass distributions applying the standard and harsher likelihood cuts are shown in Figure 8.21. Here the background distribution is least affected, staying relatively flat after area subtraction is applied, yielding similar results for the two area definitions. Once again the agreement between data and MC, as shown in the ratio plots, remains almost the same as before grooming was applied.

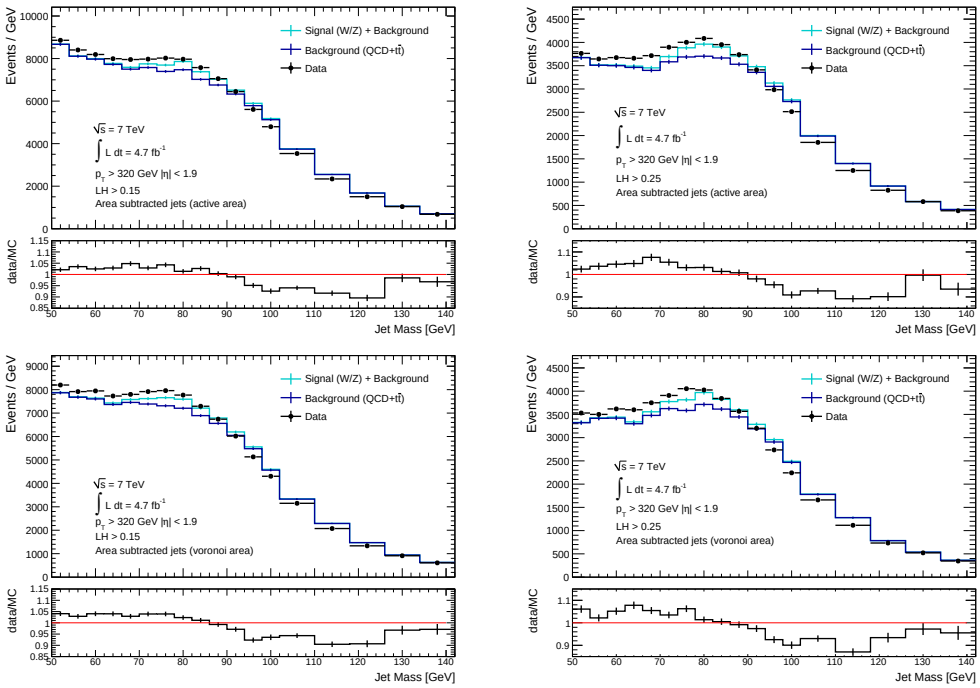

Figure 8.21.: The mass distribution comparing data and MC for jets passing the standard likelihood selection (left) and a harsh cut on the likelihood (right) after area subtraction has been applied, using the active (top plots) and Voronoi (bottom plots) area definition.

The resulting mass distribution in data is compared to the various different MC simulations in Figure 8.22. There is relatively good agreement between the data and the MCs with the data lying between the various different MCs considered.

Summary

Looking at the effect of applying grooming techniques to the jets after the selection, a small improvement in the signal to background ratio can be gained, as shown in Figure 8.23. The splitting and filtering technique applied using the standard parameters has a large effect on the background mass distribution causing a peak

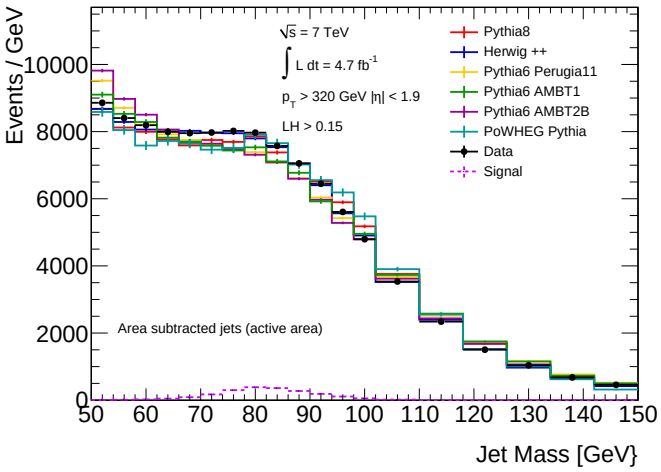

Figure 8.22.: The mass distribution after the standard likelihood cut and area subtraction has been applied using the active area definition comparing the data and the different background MCs (with the signal contribution added)

under the signal; however, the other techniques have a less severe impact on the background mass distribution, particularly in the case of area subtraction. This can be seen in Figure 8.24 which summarises the effect that the techniques have on both the background and signal mass distributions. To assess and compare the various techniques futher the RMS and mean of the signal distributions, along with the signal and background efficiencies are shown in Table 8.7. The shift in mass is clear and there is a slight improvement in the width of the distribution, except in the case of splitting and filtering. In all cases the agreement between the data and the Monte Carlo is not particularly affected by applying grooming.

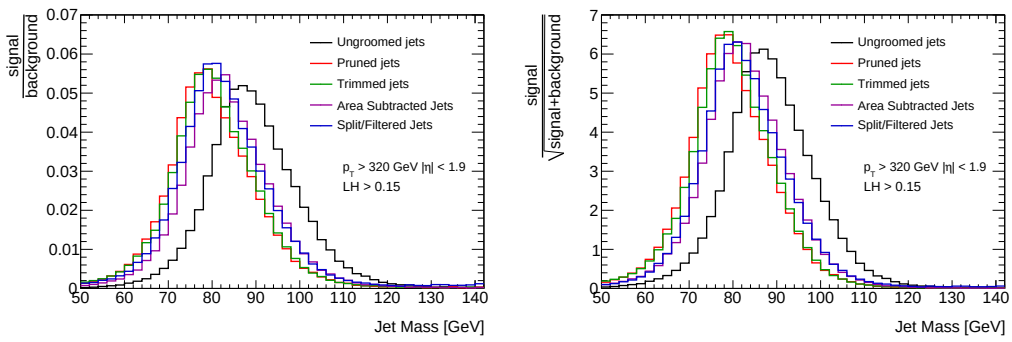

Figure 8.23.: The signal-to-background (left) and signal-to-square-root-background (right) ratios for the different grooming algorithms applied after the standard likelihood cut based on the default signal and background MC

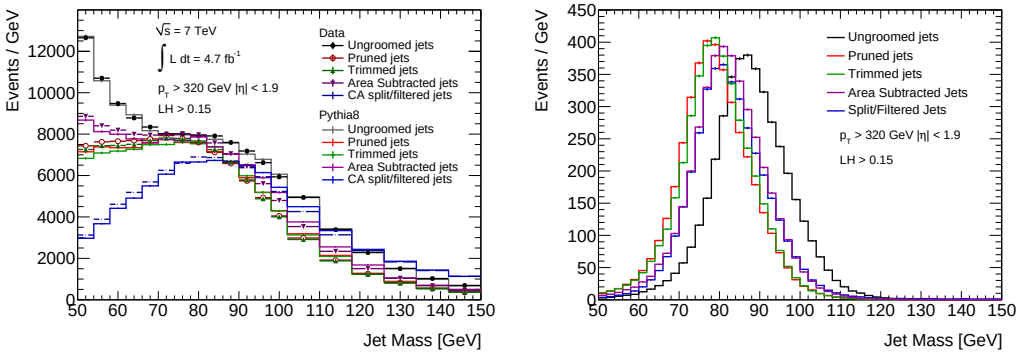

Figure 8.24.: A summary plot showing the effect of grooming on the mass distribution in the data compared to MC on the left and for the signal MC on the right

	RMS	<m> [GeV]	RMS/<m>	s_{eff}	b_{eff}
ungroomed	9.88	87.79	0.1125	1	1
pruned	9.30	78.99	0.1177	0.993	0.769
trimmed	9.26	79.49	0.1165	0.993	0.761
split/filtered	10.18	82.78	0.1230	0.943	0.740
area subtracted	9.51	82.21	0.1157	0.997	0.845

Table 8.7.: The effect of the grooming techniques in terms of the signal mean and RMS and the signal and background efficiencies.

As shown by the correlation plots in Figure 8.25 the grooming results in a shift of about 10 GeV in mass. The large spread in the case of splitting and filtering is because the jet is reclustered with a larger radius so can gain mass by taking in extra constituents compared to the anti-k_T case.

So far the effect of grooming on the jet mass has been considered but the grooming techniques also change the jet shapes, as some of the jet constituents are cut out. The effect of grooming on jet shapes and on the selection likelihood is also studied, and will be discussed after the evaluation of systematic uncertainties.

8.5.3. Systematic Errors on Groomed Distributions

For the groomed distributions two main sources of systematic errors were considered: the jet scale uncertainty and the resolution uncertainty. The jet scale uncertainty was calculated using the ratio between the value of the variable calculated using

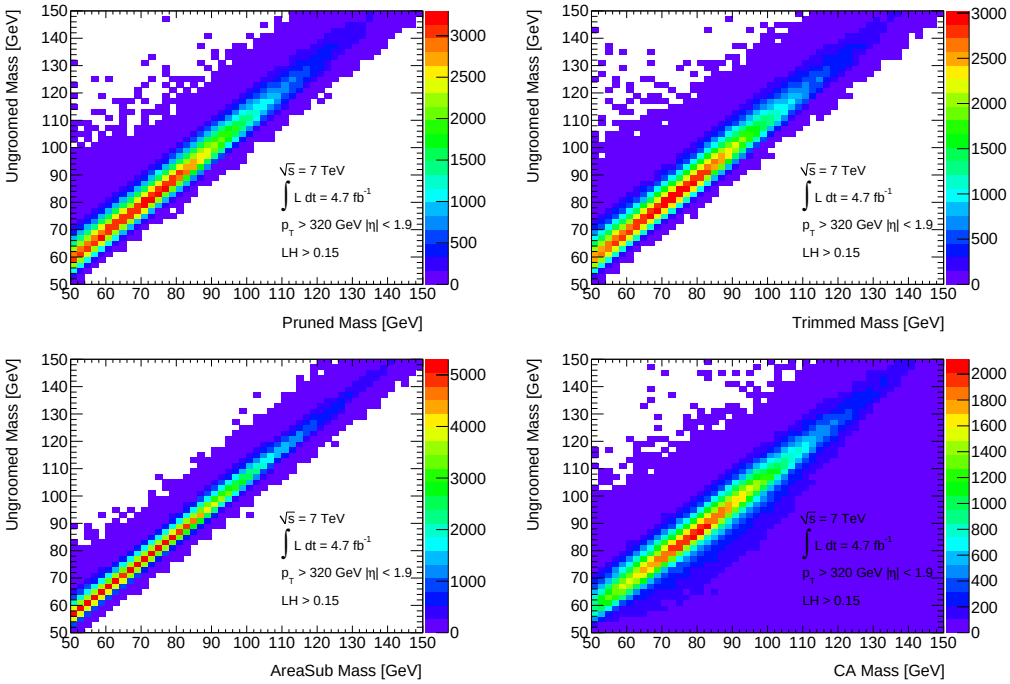

Figure 8.25.: Correlation plots showing the effect of the different grooming techniques on the mass.

calorimeter clusters and that same variable using tracks [52, 69], as shown in the plots in Figure 8.26. Then the double ratio of this distribution in data and various MCs was taken. The maximum envelope of this double ratio was fitted with a third degree polynomial function and this is taken as the fractional systematic error used on that variable.

The tracks are not reconstructed with 100% efficiency so an additional uncertainty must be evaluated to account for this. A track collection accounting for this uncertainty is produced, and in a similar way to before the ratio between the value of the variable calculated with the original track collection and the value calculated with this new track collection is taken. The ratio of this distribution in data and in PYTHIA 8 MC is calculated and then fitted with a third order polynomial function, as shown in Figure 8.27. This error is then summed in quadrature with the original scale uncertainty.

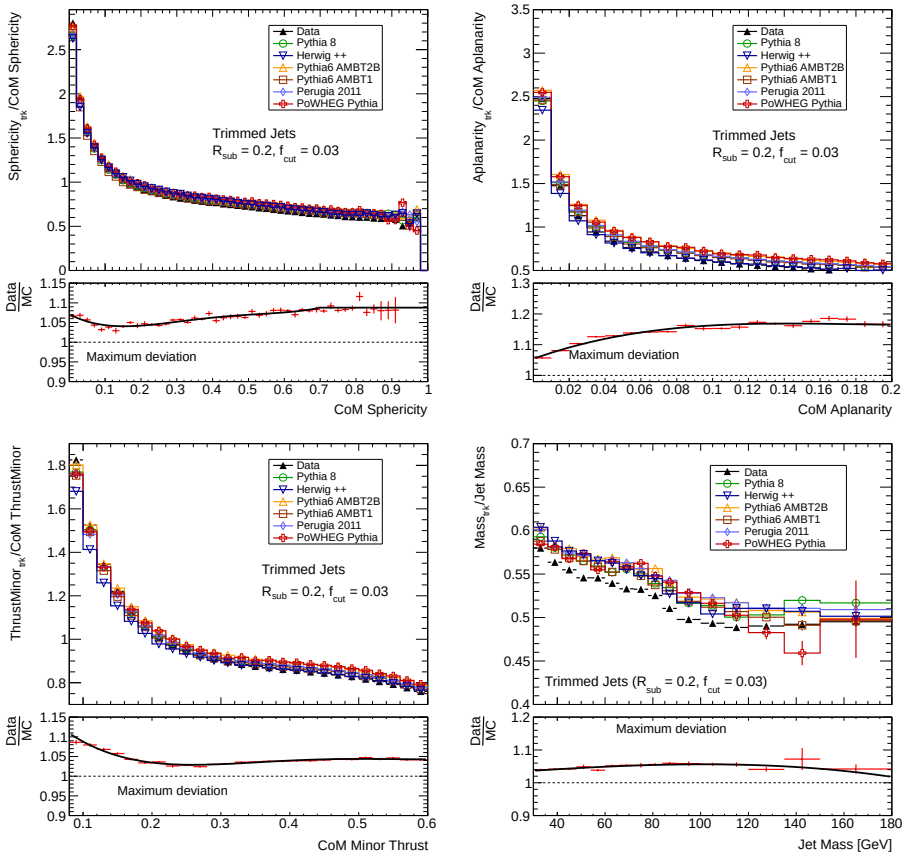

Figure 8.26.: The ratio between calorimeter and track based variables for sphericity, aplanarity, thrust minor and the mass (top left to bottom right). The maximum deviation of the double ratio between data and the various MCs of this quantity shown on the bottom plot. This maximum deviation is fitted with a polynomial function shown by the black line.

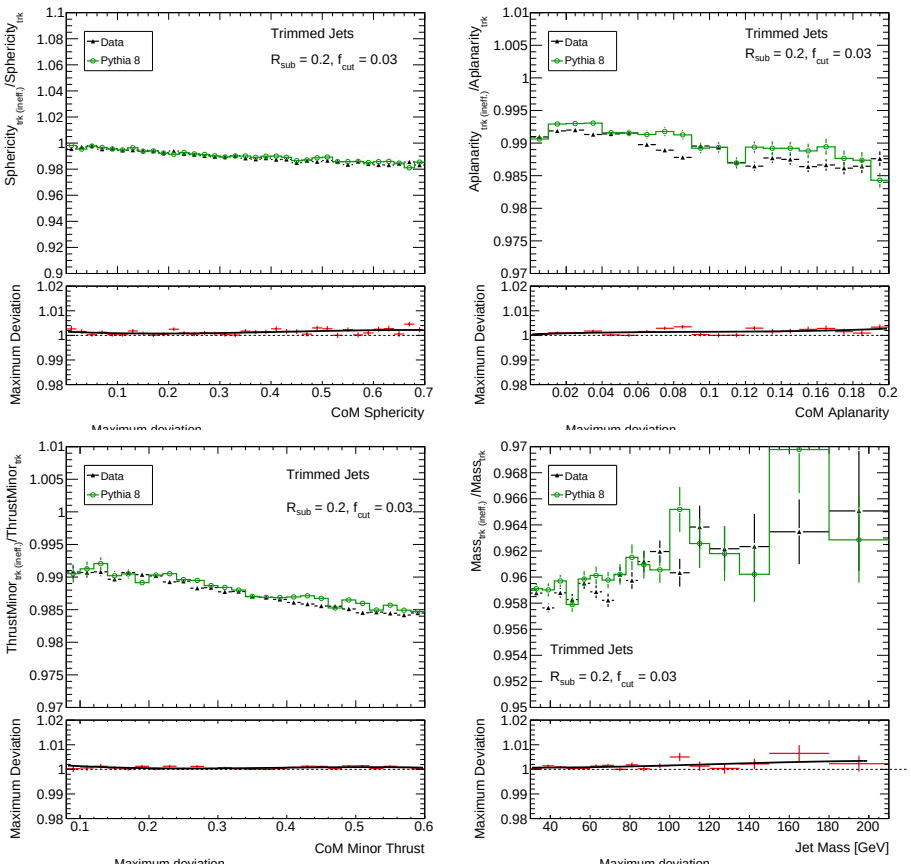

Figure 8.27.: The ratio between variables calculated using the tracks and a track collection which accounts for the tracking inefficiency for sphericity, aplanarity, thrust minor and the mass (top left to bottom right). The double ratio between data and MC of this quantity shown on the bottom plot and fitted with a polynomial function shown by the black line.

The resolution uncertainty is calculated using truth MC information. The difference between the value of a jet shape calculated at reconstruction level and at truth level is taken and the RMS of this distribution in each bin is plotted. The mean of the distribution is accounted for by the scale uncertainty so this is left free to float. Then, as before, the ratio of this distribution between the different MCs relative to PYTHIA8 is taken. The envelope of this is once again fitted with a third order polynomial and this is used as the fractional systematic error due to resolution. This is calculated both for different MC simulations, as shown in Figure 8.28, and for MCs with different geometry tags and hadronic shower models, as shown in Figure 8.29. The systematics from these two effects are then summed in quadrature to produce the final uncertainty on the resolution.

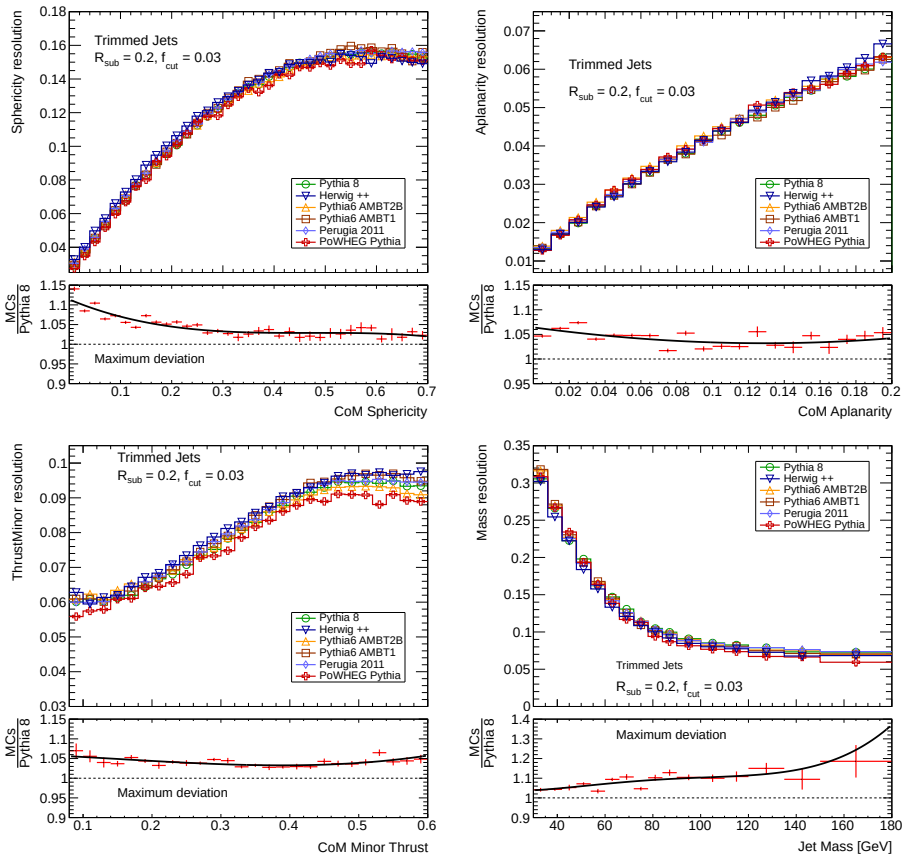

Figure 8.28.: The resolution for sphericity, aplanarity, thrust minor and the mass (top left to bottom right). The maximum deviation of the ratio between PYTHIA8 and the other MCs is shown on the bottom plot and fitted with a polynomial function shown by the black line.

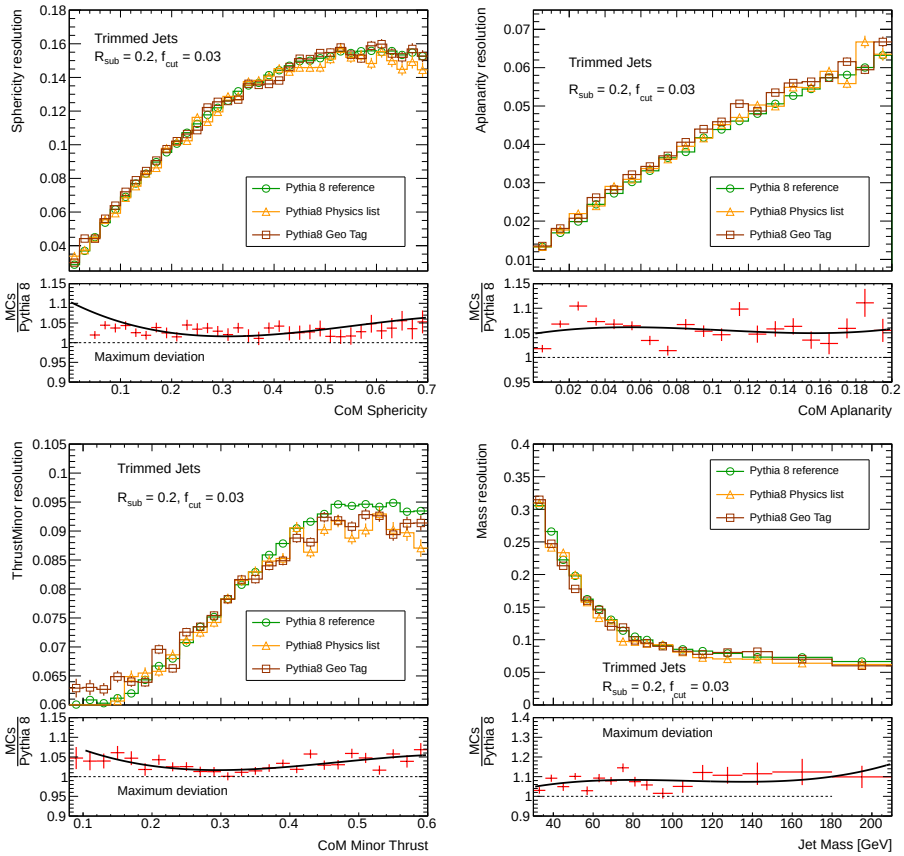

Figure 8.29.: The resolution for sphericity, aplanarity, thrust minor and the mass (top left to bottom right) in MCs accounting for dead material and different geometry tags. The maximum deviation of the ratio between PYTHIA8 and these other MCs is shown on the bottom plot and fitted with a polynomial function shown by the black line.

The contribution to the uncertainty of all these different sources is summarised in Figure 8.30. Once these uncertainties have been calculated they must be propagated through to the variables. To do this four distributions are produced. The first is the standard distribution of a variable. The second is the distribution of the same variable after it has been shifted up by the fractional systematic uncertainty due to scale. The third is the distribution after the value of the variable is shifted down by the fractional systematic uncertainty due to scale. For the last distribution the variable is smeared by the resolution uncertainty.

Additionally the jet energy scale is taken into account. In the case of the mass it is assumed the jet mass scale and jet energy scale are 100% correlated so the second and third curves are produced by shifting the mass and energy up (or down) at the

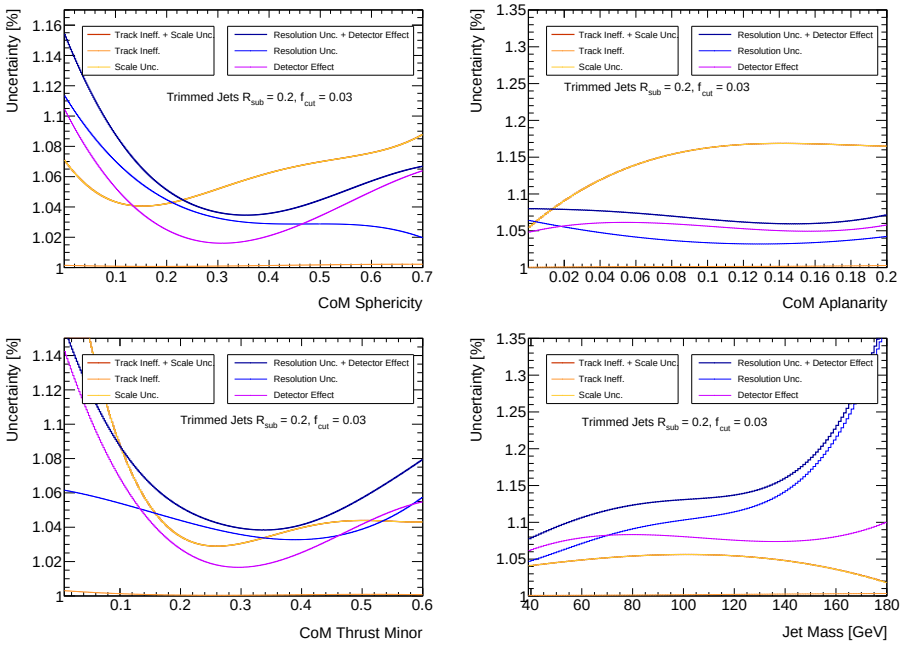

Figure 8.30.: A summary of the contribution to the systematics from the different sources considered for sphericity, aplanarity, thrust minor and mass (top left to bottom right) in the case of trimmed jets

same time. For the case of the jet shapes two additional curves are drawn where the jet energy scale is shifted up and down. Plots showing these curves are in Figure 8.31. The fractional uncertainty produced by these curves is shown in Figure 8.32.

The final uncertainty is the quadratic sum of these sources, where the maximum deviation is taken so as to have symmetric uncertainties on each point. It is these systematics that are used in the plots of the jet shapes and mass in the following sections.

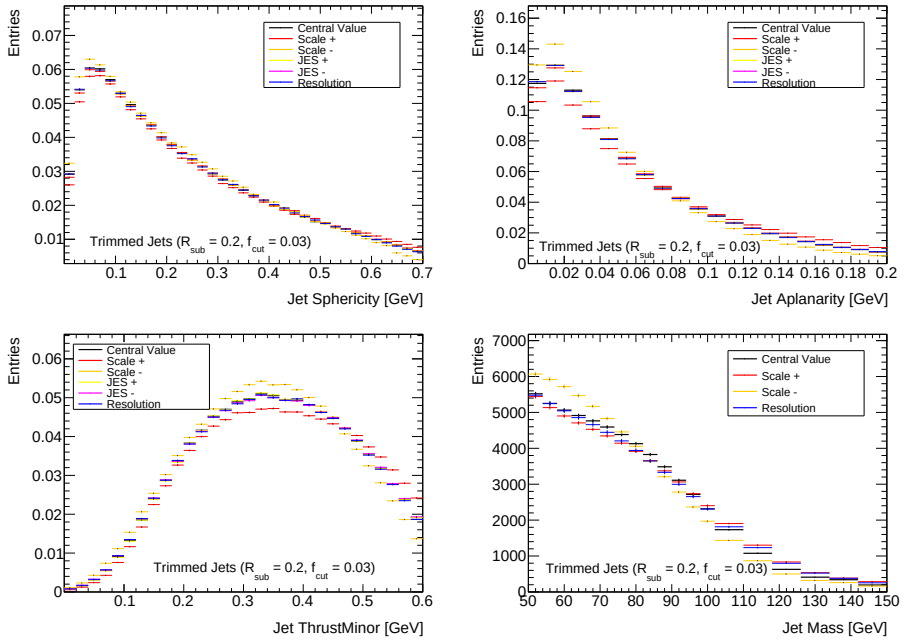

Figure 8.31.: A summary of the effect varying the various systematics has on the distributions of sphericity, aplanarity, thrust minor and mass (top left to bottom right) in the case of trimmed jets

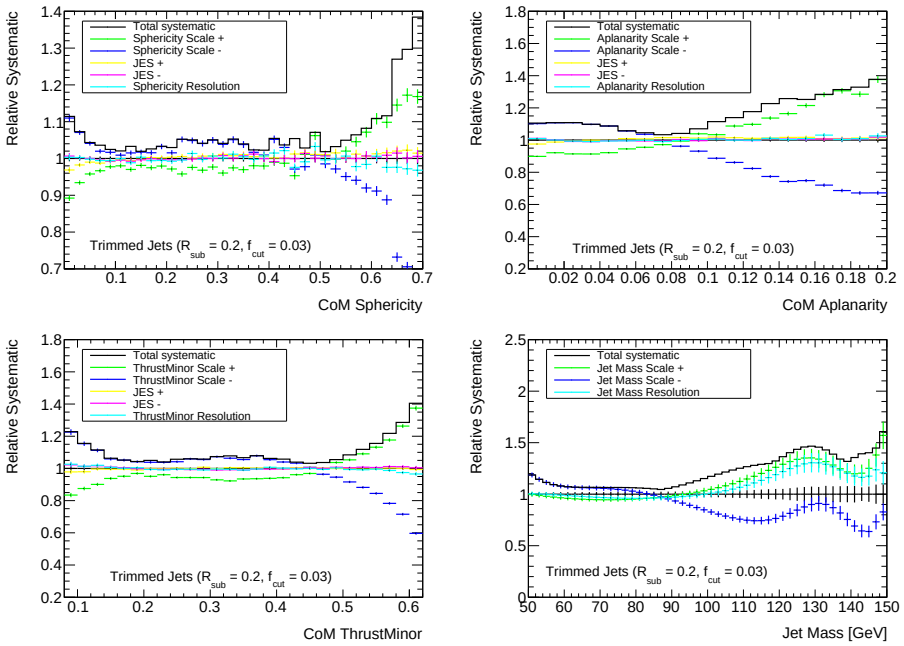

Figure 8.32.: A summary of the contribution to the systematics from the different sources considered for sphericity, aplanarity, thrust minor and mass (top left to bottom right) in the case of trimmed jets

8.5.4. Calculating the Jet Shapes after Grooming the Jets

Pruning and Trimming

In the cases of pruning and trimming the constituents making up the jet are changed and hence the shapes in the centre of mass frame can be recalculated using these constituents instead. From these a new likelihood can be developed and cut on. The distributions of the jet shapes after pruning are shown in Figure 8.33 for the standard signal and background MC and data, as well as the likelihood resulting from these. Similar distributions for the shapes after trimming are shown in Figure 8.34. The background MC and data match up well, as would be expected because without the likelihood cut applied the data is mostly composed of the background jets.

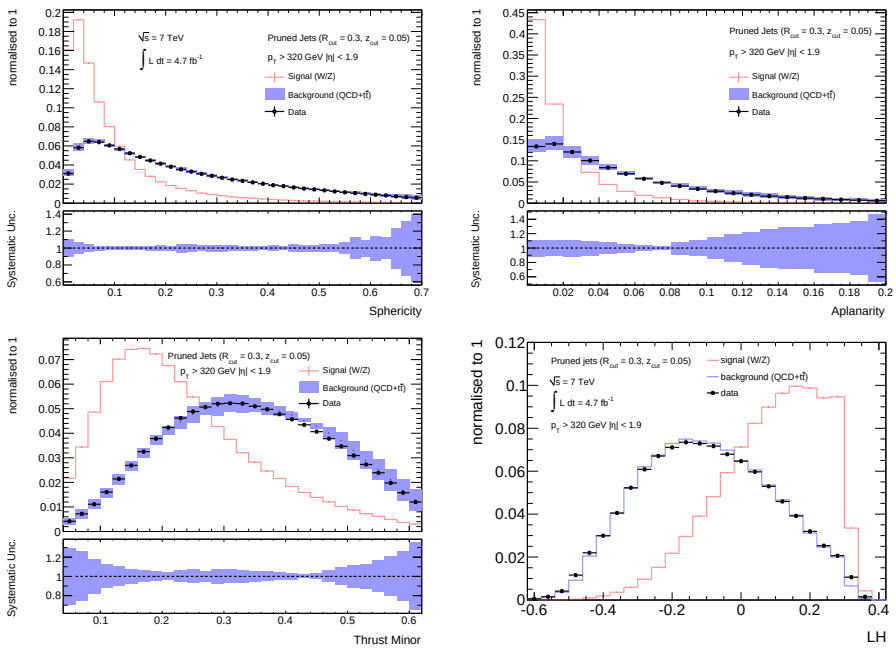

Figure 8.33.: The jet shape variables based on the jet constituents after pruning is applied and the resulting likelihood distribution based on these in data and signal and background MC.

These shape distributions show that a good discrimination between signal and background is still present after grooming and a similar background rejection can be achieved by cutting on the resulting likelihood distribution.

A comparison between the data and different background MCs is shown for pruning in Figure 8.35 and trimming in Figure 8.36. From these it can be seen that

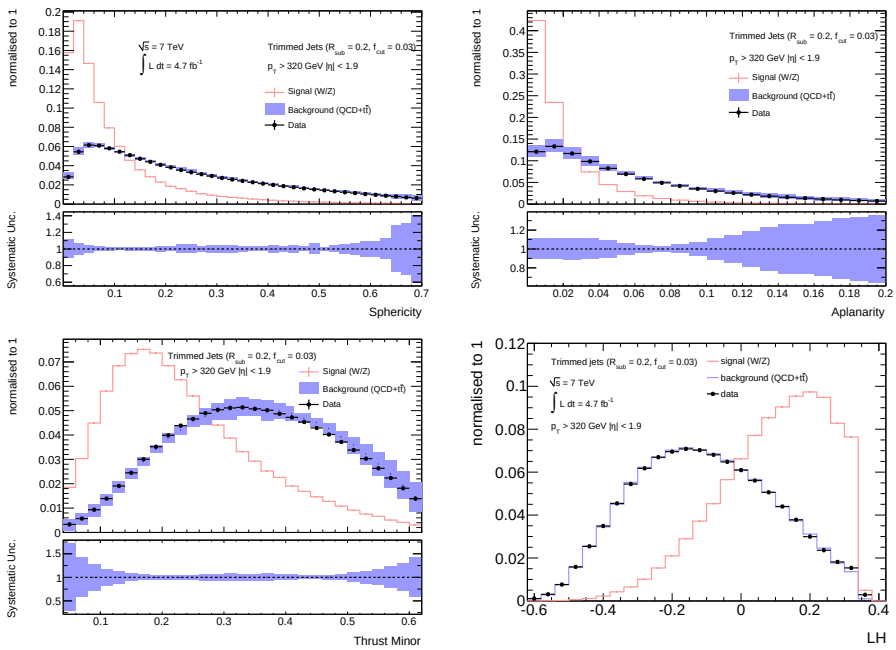

Figure 8.34.: The jet shape variables based on the jet constituents after trimming is applied and the resulting likelihood distribution based on these in data and signal and background MC.

there is a fair agreement between data and MC and that the data distribution lies between those from the different MCs. To assess more clearly how the agreement between data and background MC is affected by grooming several ratio plots were produced. Firstly, in Figures 8.37, 8.38 and 8.39, the ratio is plotted for ungroomed, trimmed and pruned jets on the same plot, with separate ratio plots for each of the different MCs. Secondly, the curves for each MC are put on the same plots but a separate plot is made for the shape after pruning and trimming and for the ungroomed sample, as shown in Figures 8.40, 8.41 and 8.42.

The ratio plots show there is a general improvement in the agreement between data and MC for the shapes calculated from groomed jets, especially at the low end of the spectra which is where the likelihood cut is focussed in the analysis and where the signal is expected to be found. This is possibly because the grooming techniques aim to cut out the softer parts of the jet which are more difficult to model hence less well represented by the MC. However, for the aplanarity and sphericity, in some cases the agreement between data and MC is worsened at the higher values. That said, the fluctuations in this region of the spectrum are generally larger as there are fewer events. Grooming the jets causes a mass shift, forcing some of the jets out

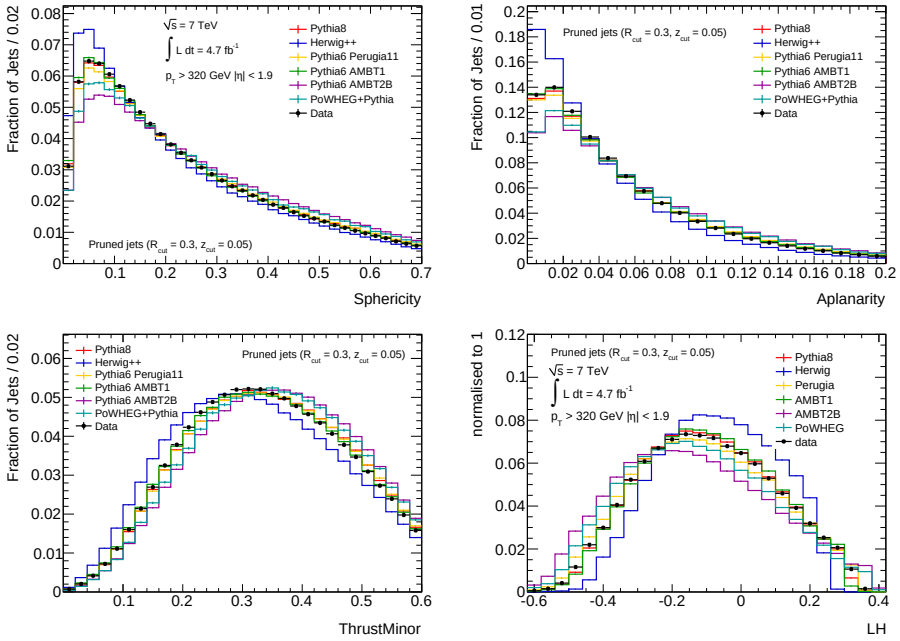

Figure 8.35.: The jet shape variables based on the jet constituents after pruning is applied and the resulting likelihood distribution based on these comparing different background MCs to data.

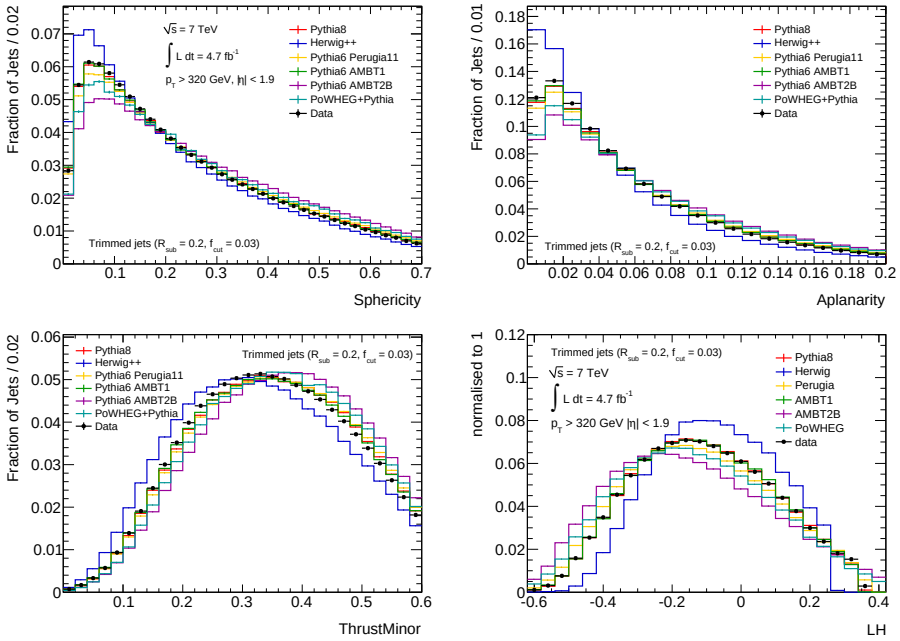

Figure 8.36.: The jet shape variables based on the jet constituents after trimming is applied and the resulting likelihood distribution based on these comparing different background MCs to data.

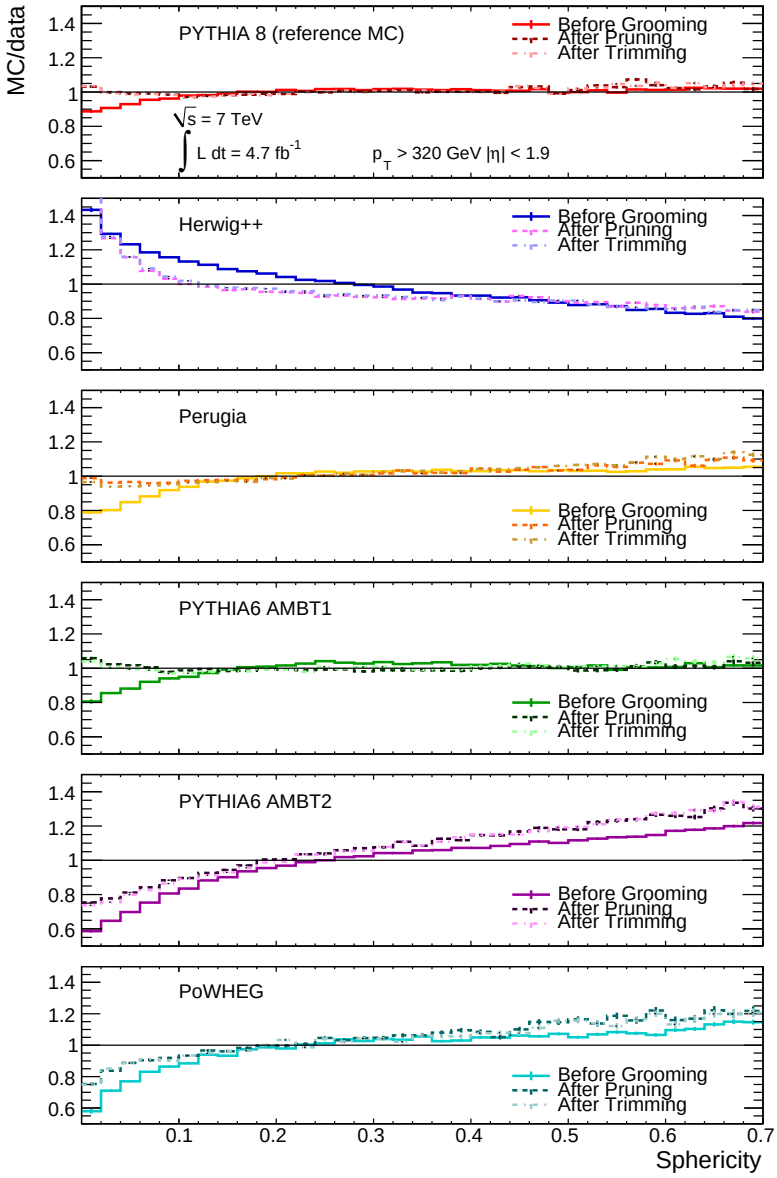

Figure 8.37.: The ratio of the jet sphericity in data and the various MCs for ungroomed, pruned and trimmed jets.

of mass range reducing the number of jets. The reduction in the number of events means the fluctuations at the higher values are enhanced for grooming.

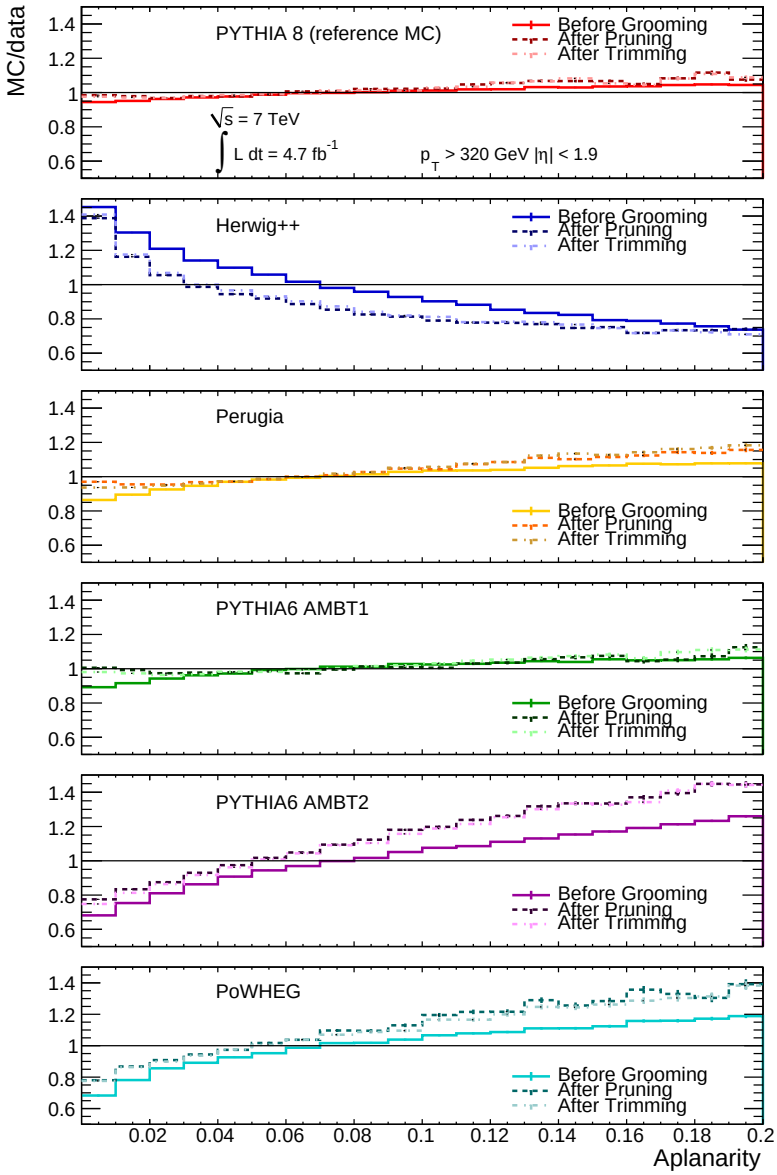

Figure 8.38.: The ratio of the jet aplanarity in data and the various MCs for ungroomed, pruned and trimmed jets.

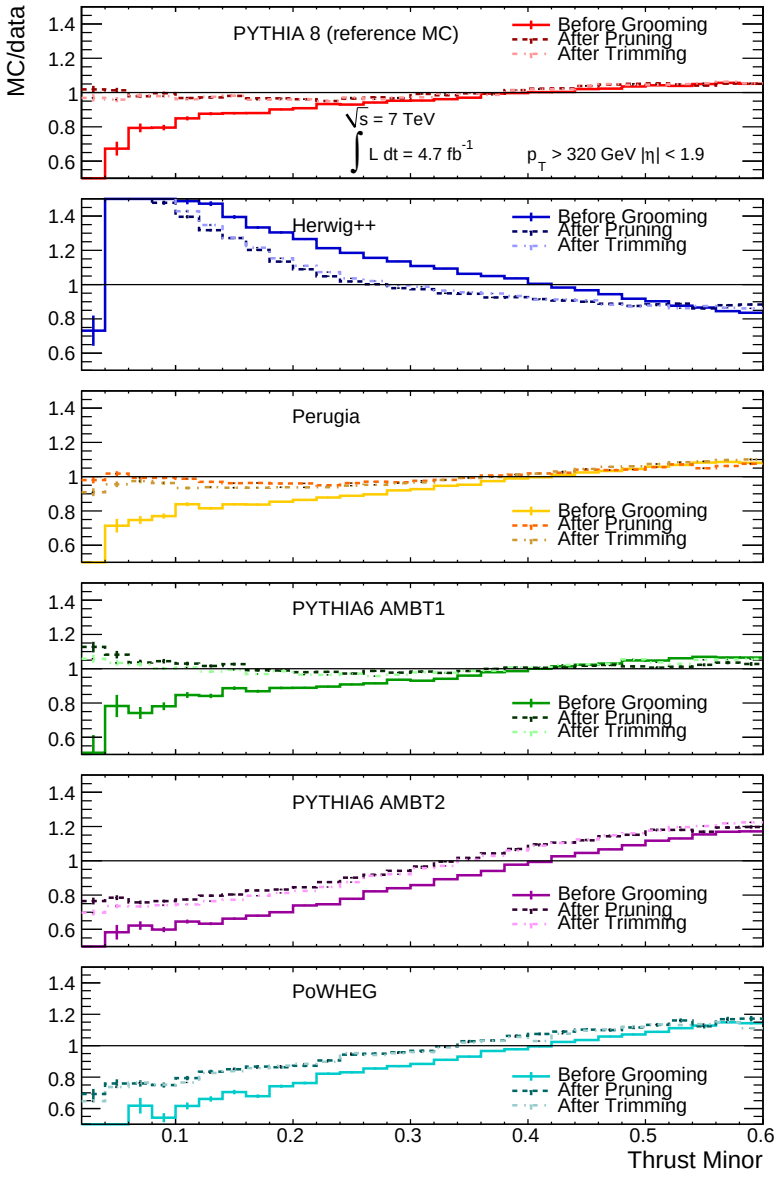

Figure 8.39.: The ratio of the jet thrust minor in data and the various MCs for ungroomed, pruned and trimmed jets.

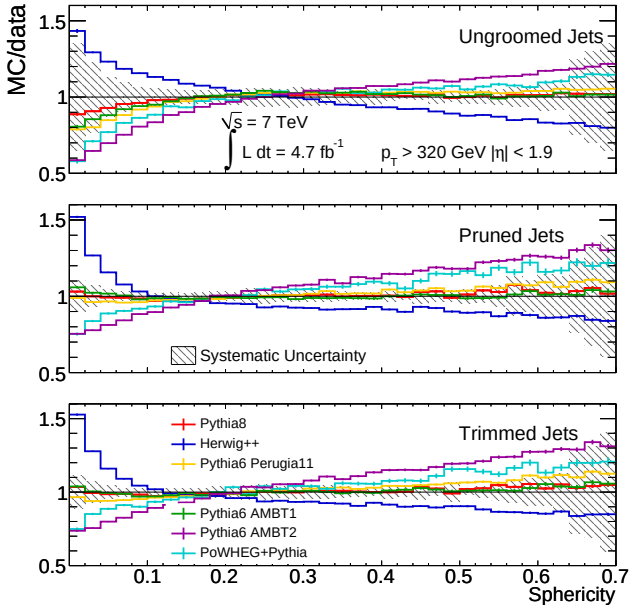

Figure 8.40.: The ratio of the jet sphericity in data and the various MCs for ungroomed, pruned and trimmed jets with the systematics uncertainty on the data in each case also shown.

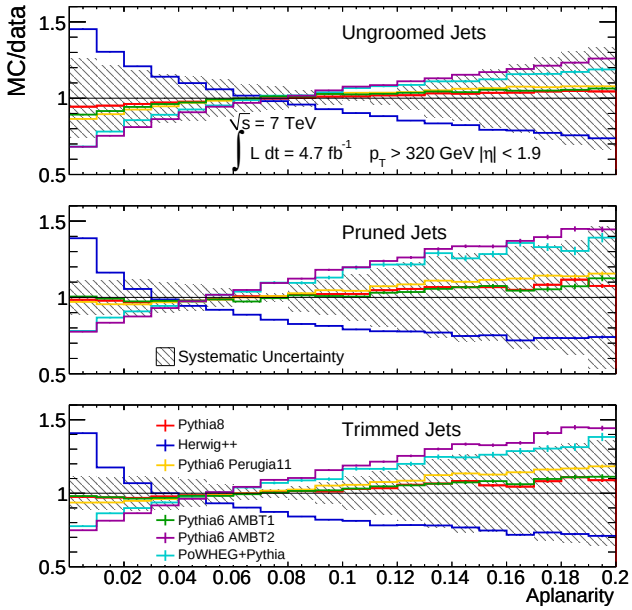

Figure 8.41.: The ratio of the jet aplanarity in data and the various MCs for ungroomed, pruned and trimmed jets with the systematics uncertainty on the data in each case also shown.

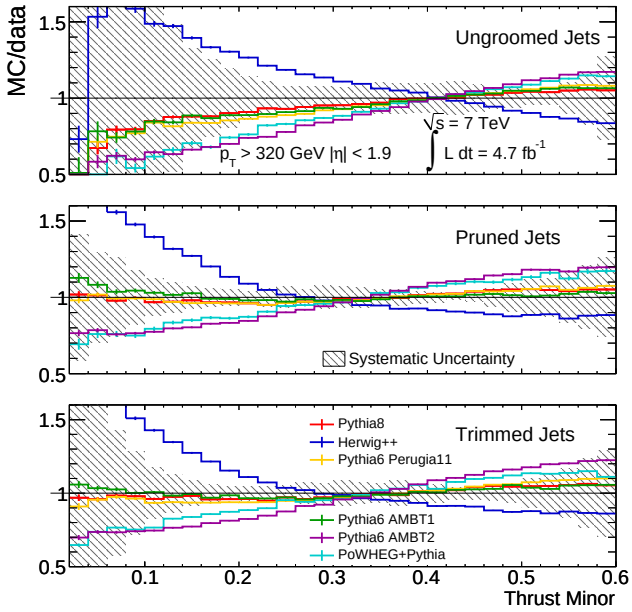

Figure 8.42.: The ratio of the jet thrust minor in data and the various MCs for ungroomed, pruned and trimmed jets with the systematics uncertainty on the data in each case also shown.

Area Subtraction

In the case of area subtraction the constituents of the jet remain unchanged but the p_T of the jet is changed and hence the boost of the constituents will be affected, which impacts the calculation of the shapes. The resulting distributions are shown in Figure 8.43. These jet shapes also have good discrimination between signal and background and a new likelihood function is produced from them.

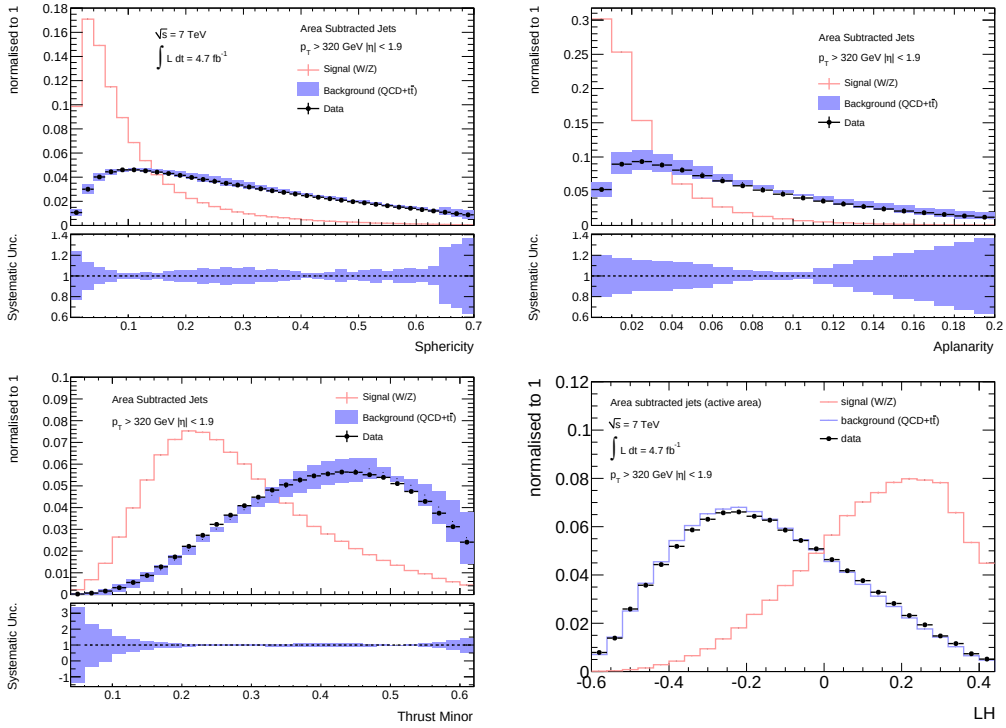

Figure 8.43.: The jet shape variables based on the jet constituents after pruning is applied and the resulting likelihood distribution based on these in data and signal and background MC.

8.5.5. Study of Grooming after Cutting on the Groomed Likelihood

It is possible to repeat the W/Z boson selection by cutting on the likelihood produced based on groomed shapes. The cut value was chosen to give the same background rejection as the ungroomed case, which resulted in a cut of $LH > 0.16$ for both trimmed and pruned jets. For pruning this leads to a background rejection of 89.7%

with a signal and efficiency of 39.3% and for trimming the background rejection is 89.5% for a signal efficiency of 41.6%. Although the signal efficiencies here seem substantially lower than the ungroomed case, this is distorted by the fact that some jets are moved out of the mass window by applying the grooming. In the case of pruning the background mass distribution has 51.1% fewer events, while the signal distribution retains 98.1% of the events. This means the total background rejection from the ungroomed mass distribution to the pruned mass distribution after cutting on the pruned likelihood is 95.0% with a signal efficiency of 38.6%. For trimming, the background rejection before the likelihood is applied is 49.5% with a signal efficiency of 98.3%, resulting in a total rejection after the likelihood cut compared to the original ungroomed mass distribution of 94.5% and a signal efficiency of 40.9%.

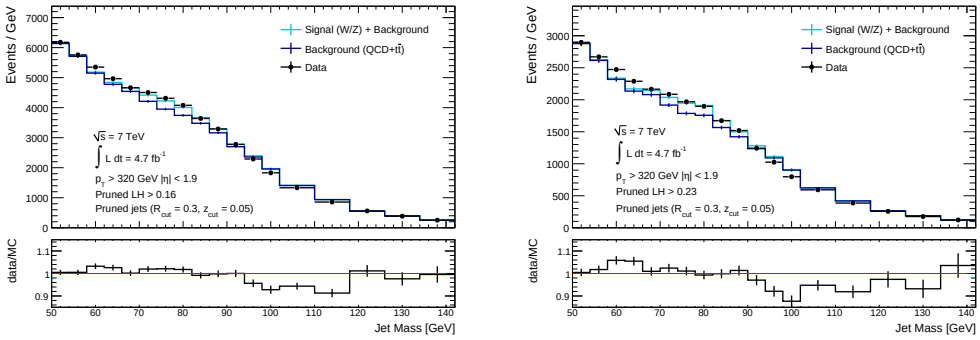

Figure 8.44.: The pruned mass distribution comparing data and MC for jets passing a cut on the pruned likelihood selection chosen to reject 90% of the background (left) and 95% of the background (right).

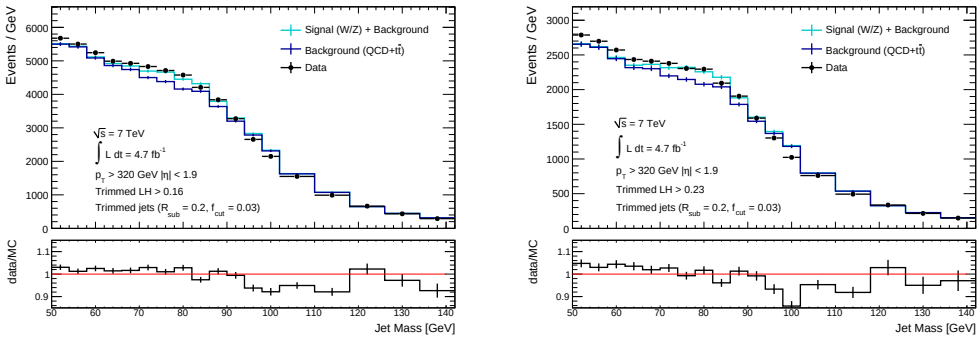

Figure 8.45.: The trimmed mass distribution comparing data and MC for jets passing a cut on the trimmeded likelihood selection chosen to reject 90% of the background (left) and 95% of the background (right).

The mass distribution after a cut on the groomed likelihood is shown for pruning in Figure 8.44 and trimming in Figure 8.45, for both a loose and tight likelihood cut.

The tight likelihood cut was chosen to give a background rejection of about 95% leading to a cut of $LH > 0.23$ in both cases. The corresponding signal efficiencies are 22.5% for pruning and 25.4% for trimming. These plots show that the background mass distribution remains fairly flat after this cut, perhaps flatter than the ungroomed case when pruning is applied. The agreement between the data and MC remains good, staying under about 5% difference for low masses and only reaching a maximum of about 10% at the higher masses. This comparison to the various different MC's considered is shown in Figure 8.46, with the signal contribution added to each one such that it can be compared to the data. The agreement between the data and various MCs can be seen more clearly by the ratio plots in Figures 8.47 and 8.48. Again one shows the MCs separately and the other shows the grooming techniques separately. From these it can be seen that the agreement between the data and MC is preserved after grooming, but is not considerably better or worse.

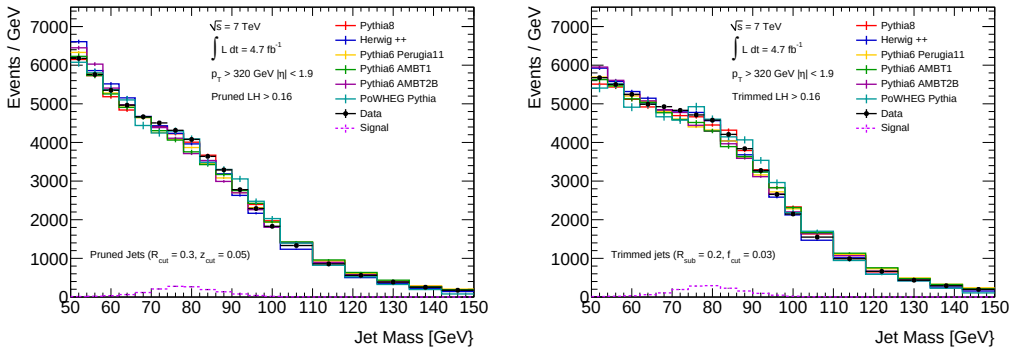

Figure 8.46.: The pruned (left) and trimmed (right) mass distributions comparing data and various MCs for jets passing a cut on the appropriate likelihood chosen to reject 90% of the background.

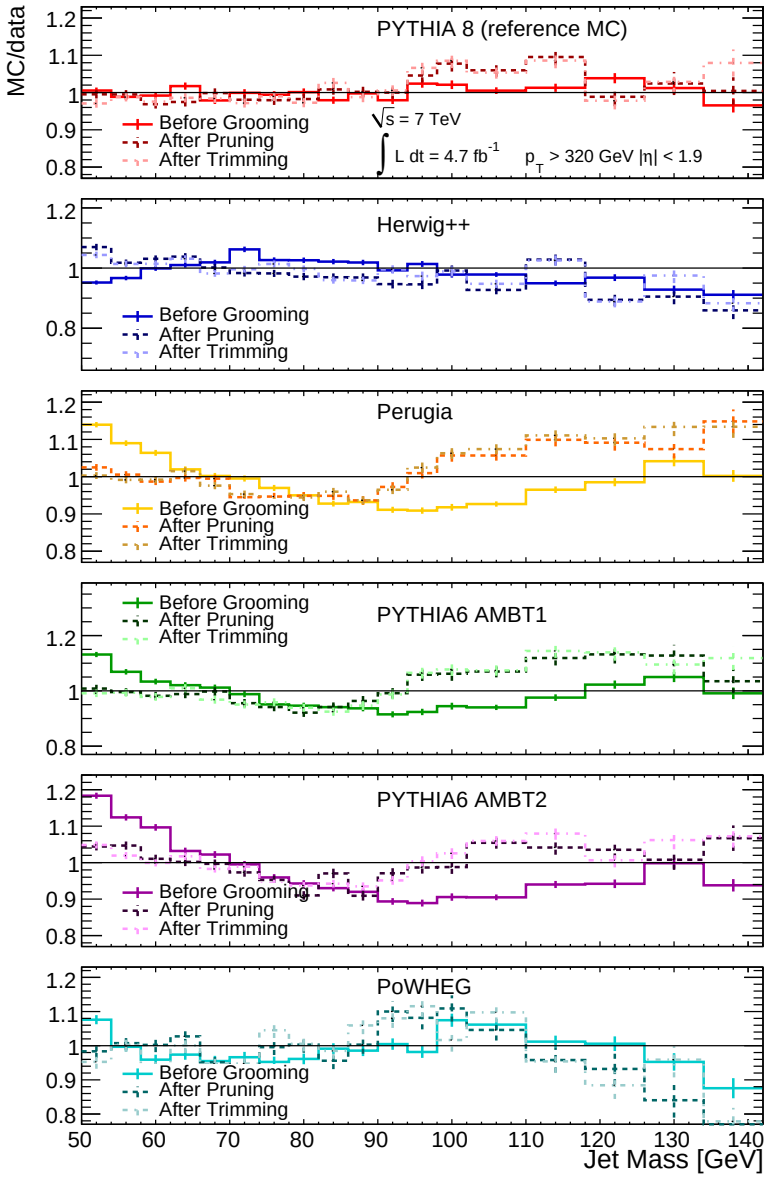

Figure 8.47.: The ratio of the jet mass in data and the various MCs for ungroomed, pruned and trimmed jets.

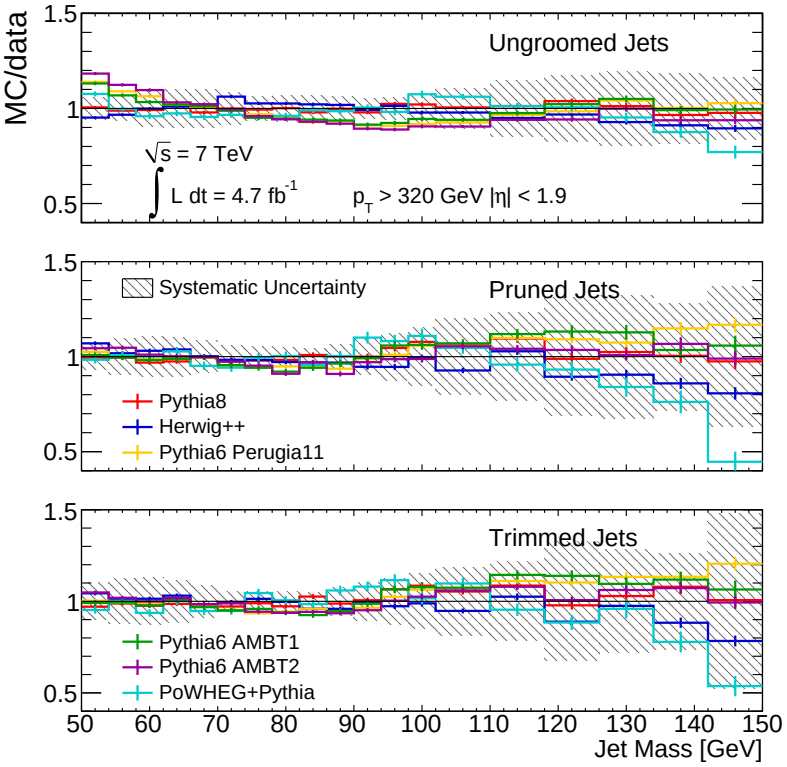

Figure 8.48.: The ratio of the jet mass in data and the various MCs for ungroomed, pruned and trimmed jets with the systematics uncertainty on the data in each case also shown.

8.5.6. Pileup Dependence

In order to assess the dependence of the mass on pileup the distribution is split into 3 different categories according to the number of vertices in the event. Events with less than 5 vertices are considered low pileup and events with more than 10 vertices high pileup. Only these two extreme cases are plotted so as to highlight the differences caused by pileup. These distributions in data and MC for ungroomed jets and after each of the techniques have been applied are shown in Figure 8.49. To see the difference more clearly the ratios between the high- and low-pileup distributions in data and MC for each of the different techniques are shown in Figure 8.50. It can clearly be seen that applying grooming reduces the dependence of the mass on pileup in all cases. As the grooming techniques all aim to counteract the effects of pileup

by removing the soft radiation, this is expected. This will become more important as the pileup increases with increased centre of mass energy at the LHC.

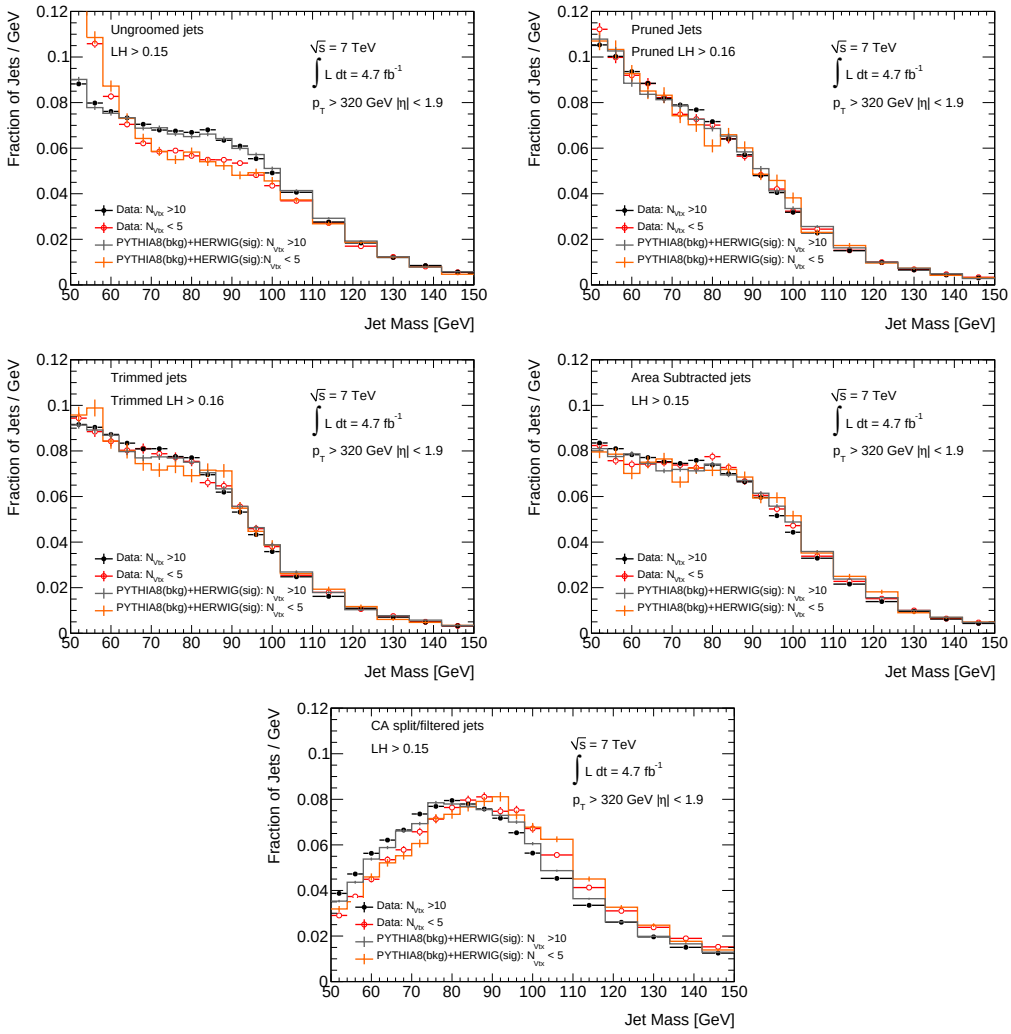

Figure 8.49.: The mass distribution separated into low (< 5 vertices) and high (> 10 verticles) pileup for jets before and after grooming is applied.

8.5.7. Summary

The four different techniques splitting and filtering, area subtraction, trimming and pruning have been studied in the case of an already strong selection for jets containing the decay of a boosted W or Z boson. As a summary the mass distribution obtained after each of these techniques is shown in Figure 8.51, with the groomed likelihood applied for the cases of trimming and pruning as this gives the best results. The

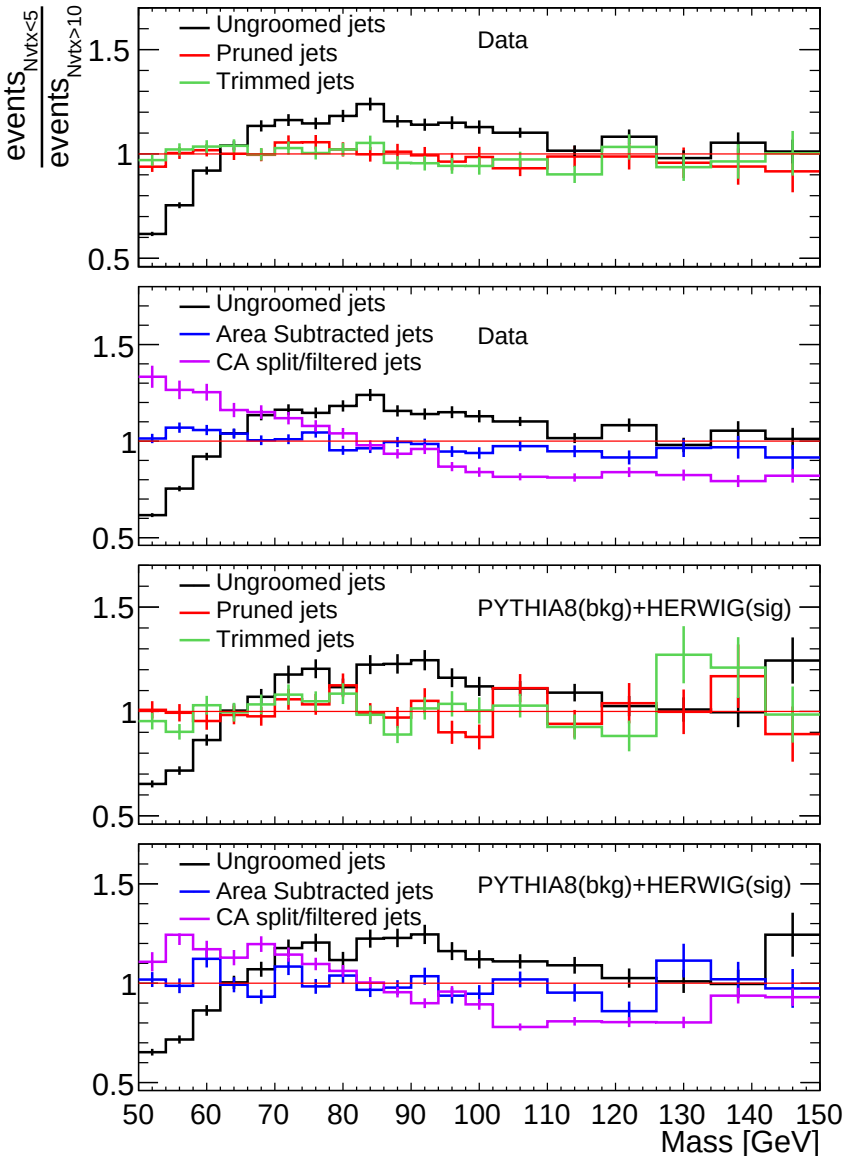

Figure 8.50.: The ratio of the low (< 5 vertices) and high (>10 vertices) pileup mass distributions before and after grooming is applied in data (top two plots) and MC (bottom two plots).

splitting and filtering technique introduces an undesirable peak in the signal mass region, due to the kinematic selection applied here. The other techniques produce a background that is as flat, if not flatter than the ungroomed case. The effect can be seen clearly in Figure 8.52 where all these distributions are plotted on the axes. This plot also highlights the reduction in the number of jets in the distributions due to

the shift in the jet mass caused by grooming. In all the cases the data MC agreement is not really affected by grooming.

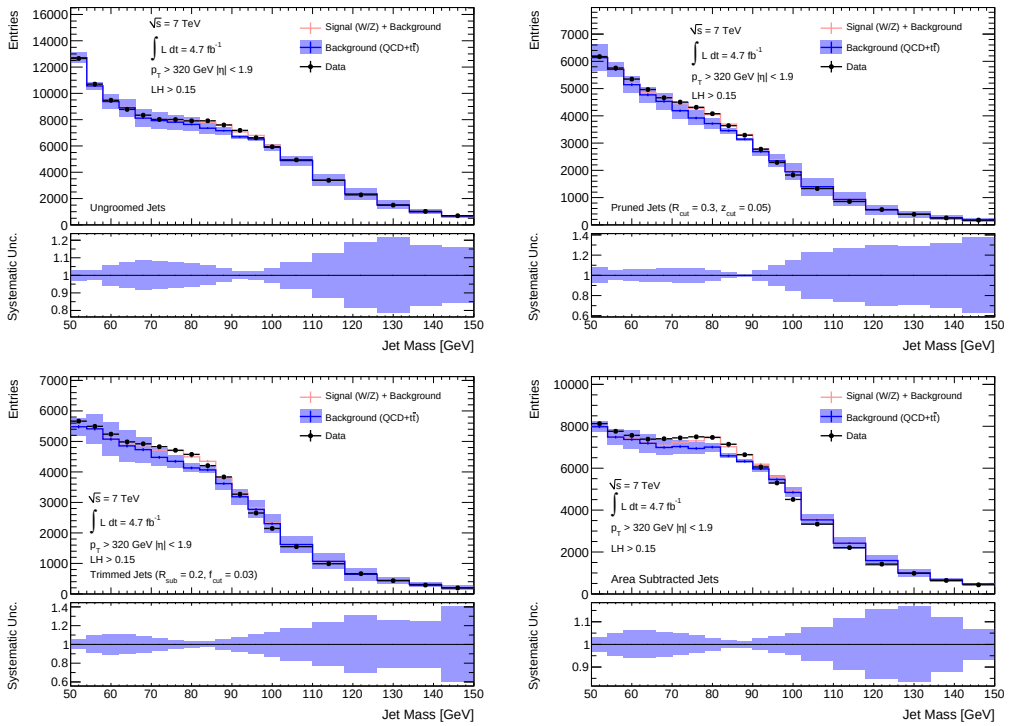

Figure 8.51.: The mass distributions with systematics in data and MC after the different grooming techniques have been applied and a cut on the appropriate likelihood made to reject about 90% of the background.

Figure 8.53 shows the signal to background ratio as a function of the jet mass as well as the value of $S/\sqrt{S+B}$ for each of the different techniques. This shows that a small gain in signal to background ratio can be made when trimming or pruning are applied but the other techniques have little effect. The significance also remains unchanged in all cases.

Lastly the effect of grooming in terms of pileup dependence was assessed and it was found that all the grooming techniques lessened the dependence of the mass distribution on pileup, which is very desirable as the luminosity increases.

As a result of these studies it can be concluded that all the grooming techniques will be very useful for future analyses at the LHC when looking for boosted heavy particle decays, particularly trimming and pruning. However, in this case the improvements are not large enough to make it worth repeating the cross-section measurement.

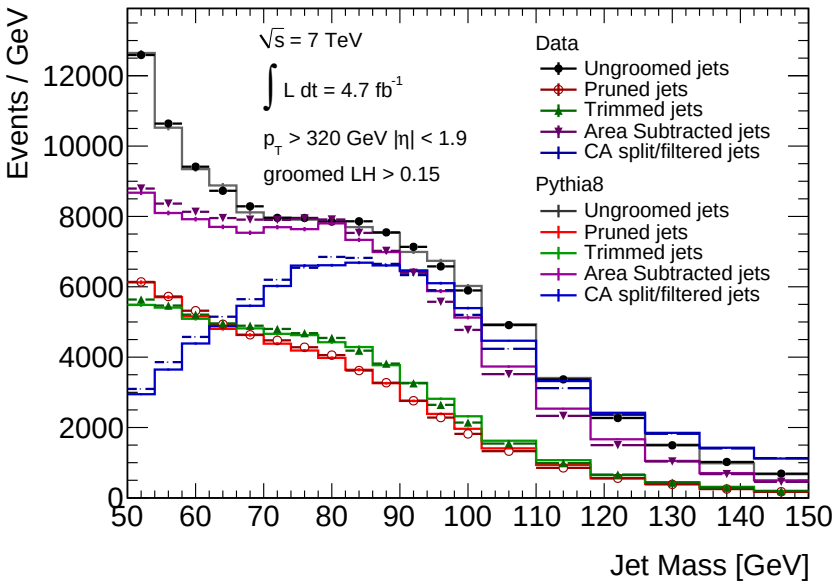

Figure 8.52.: The result of applying grooming to the jet mass distribution in data and MC using a cut on the groomed likelihood in the cases of pruning and trimming and the standard likelihood selection for the other distributions.

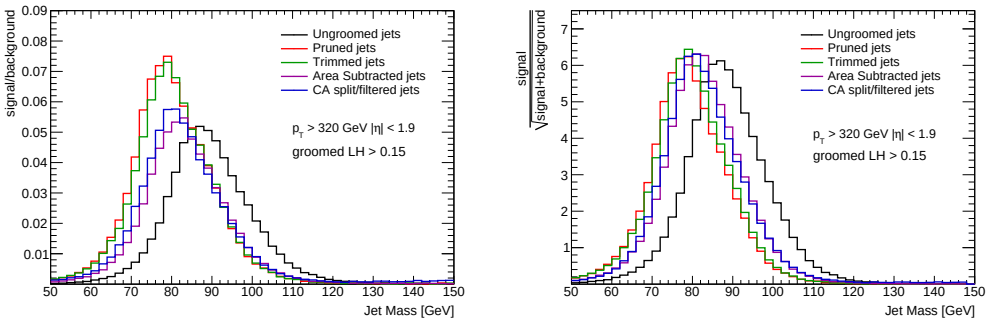

Figure 8.53.: The ratio between the signal and the background (left) and the signal and square root of the background (right) as a function of mass based on MC for each of the grooming techniques considered after cutting on the likelihood - the groomed likelihood in the cases of pruning and trimming.

Chapter 9.

Search for Diboson Resonances in Jet Final States

9.1. Introduction

The energies at the LHC allow for searches for new physics at the TeV energy scale. Here, a search for new resonant states, with masses between 1 and 3 TeV, decaying into W or Z bosons, which then both decay hadronically is carried out using 8 TeV data from the LHC obtained in 2012. Although the leptonic and semi-leptonic channels produce a cleaner signal the fully hadronic channel profits from a higher branching ratio, as shown in Table 8.1. Also, looking for TeV scale resonances means the decaying bosons are produced at high p_T where the background falls off faster than the signal, as mentioned in the context of the previous studies on hadronically decaying W/Z bosons. In this boosted regime the decay products will both be contained within a single jet, and a boson tagger, based on the splitting and filtering technique described in the previous section, but with optimised parameters, was developed to search for these states.

9.2. Collision Data

The data used in the analysis was recorded in 2012 at a centre of mass energy of 8 TeV, and corresponds to a luminosity of 20 fb^{-1}. The events are selected by the EF_j360_a10tcem trigger which requires there to be an anti-k_T jet with radius of 1.0

based on topoclusters at the electromagnetic scale at the EF trigger level with $E_T >$ 360 GeV. They must also pass the GRL and the recommended data quality cuts, namely that there was no error in the LAr or tile calorimeters, that the event was not flagged as bad by the tile trip reader and that the event is not incomplete.

9.3. Monte Carlo Samples

The process $qq \to W' \to WZ$ was used as a benchmark process for this analysis. A set of MC samples was produced with PYTHIA 8, using MSTW2008 PDFs for the event generation for W' masses between 1.2 and 3.0 TeV at 200 GeV intervals. These are based on the sequential standard model (SSM) [19], which assumes the W' couplings to quarks and leptons are the same as in the standard model, and the coupling to WZ is that of the W, scaled by $(m_W/m_{W'})^2$. Samples were also generated using Herwig for comparison and to help in the assessment of systematic uncertainties.

Two main backgrounds were considered, QCD multijet processes and V+jets events. The QCD background is by far the most dominant, but in the case that the boson tagging is very effective the V+jets could also contribute. Monte Carlo samples generated with PYTHIA 8 are used to assess both of these backgrounds.

9.4. Event Selection

An event is required to have at least two reconstructed Cambridge-Aachen (C/A) jets with a radius of 1.2, which is the basis jet for the boson tagging procedure described later. To ensure the jets are of good enough quality, events are rejected if they have any anti-k_T R=0.4 jets which are bad by the looser definition or ugly as described in Section 4.3.

An additional cleaning cut is applied to the C/A 1.2 jets, designed to remove those that are affected by trips in the tile calorimeter. When a trip occurs the region affected is masked and then corrected for offline by estimating the energy contribution from this region. However, the jets used in this analysis are large with narrow high p_T deposits within them. Hence, when these high p_T regions fall within a

masked module the jet is under corrected and when they fall in the cells neighbouring a masked module the jet is over corrected. Events are rejected if the three most energetic topoclusters in either the leading or subleading jet fall in a masked module or any of its neighbours.

These two jets must be in the region $|\eta| < 2.0$ so that the forward calorimeter is not used and that there is good overlap with the inner tracker which is used both in the boson tagging requirements and for assessment of the systematic uncertainties. A cut is also placed on the rapidity difference between these jets, $|\Delta y_{jj}| < 1.2$ which offers discrimination between the more central s-channel signal process and the mainly t-channel QCD background. This is motivated by the distributions of $|\Delta y_{jj}|$ in Figure 9.1 for four different signal mass points, 1.2, 1.8, 2.4 and 3.0 TeV, in both signal and background MC normalised to unit area. In these distributions the events are required to have a dijet mass within 10% of the W' mass being considered

$$\frac{|m_{jj} - m_{W'}|}{m_{W'}} < 10\% \tag{9.1}$$

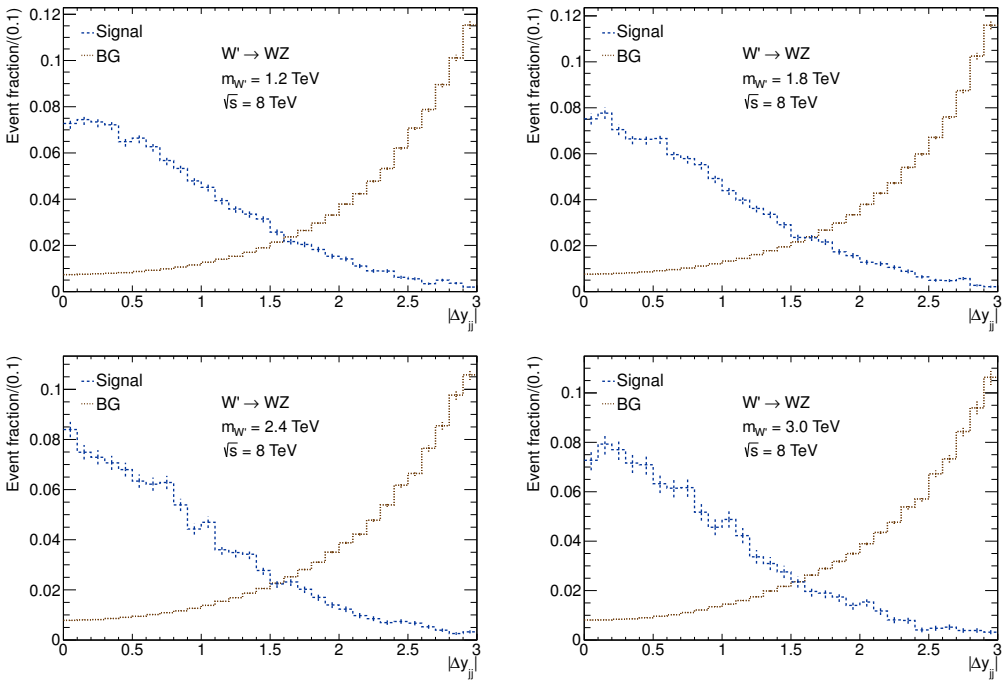

Figure 9.1.: Rapidity difference for the W' signal and the Pythia QCD background for events with $(m_{jj} - m_{W'})/m_{W'} < 10\%$. All histograms are normalized to unit area over the displayed range.

The two jets are required to pass the boson tag, which is summarised in Table 9.1. It first passes the C/A, R=1.2 jet through the splitting/filtering procedure described in section 8.5.1, with the parameters $\mu = 1.00$, $\sqrt{y_{cut}} = 0.2$ and fixes R_{filt} to 0.3, keeping the hardest 3 subjets. It is worth noting that here the mass drop is actually switched off and the value of y_{cut} decreased as it was found that this is more effective in the search for W/Z bosons decaying hadronically. However, the value of $\sqrt{y_f}$ is retained and a harsher cut is made on it later in the tagging process.

Table 9.1.: The boson tag requirements

pass split/filtering with	$\sqrt{y} > 0.2$
	$\mu < 1.00$
	$R_{filt} = 0.3$
	$n_{subjets} = 3$
$60 \leq m < 110$ GeV	
$\sqrt{y_f} \geq 0.45$	
$n_{gtrk} < 30$	

The filtered jet is then required to be in the mass range $60 \leq m < 110$ GeV, chosen to maintain a high signal efficiency, as shown by the distributions in Figure 9.2. These plots once again have the dijet mass requirement from equation 9.1 and additionally have the rapidity difference cut imposed, $|\Delta y_{jj}| < 1.2$.

The jets are then required to have $\sqrt{y_f} \geq 0.45$ where $\sqrt{y_f}$ is the value coming from the filtering process. This cut was chosen based on the signal and background efficiencies calculated from the plots in Figure 9.3. These plots are made using the signal and background MC with the same dijet mass and rapidity gap cuts as for the mass plots above and also have the jet mass requirement $60 \leq m < 110$ GeV imposed.

Lastly there is a cut on the number of ghost associated tracks to the ungroomed jet, $n_{gtrk} < 30$, as described in Section 4.1.3. The distributions in Figure 9.4 clearly shown that the MC modelling of this variable is not very good, hence the value for the cut was chosen using a V+jets spectrum in the data.

A V+jets spectrum is produced in data by taking events which pass the trigger, have $0.56 < p_T < 0.65$ TeV (chosen to give the most visible peak), have a rapidity

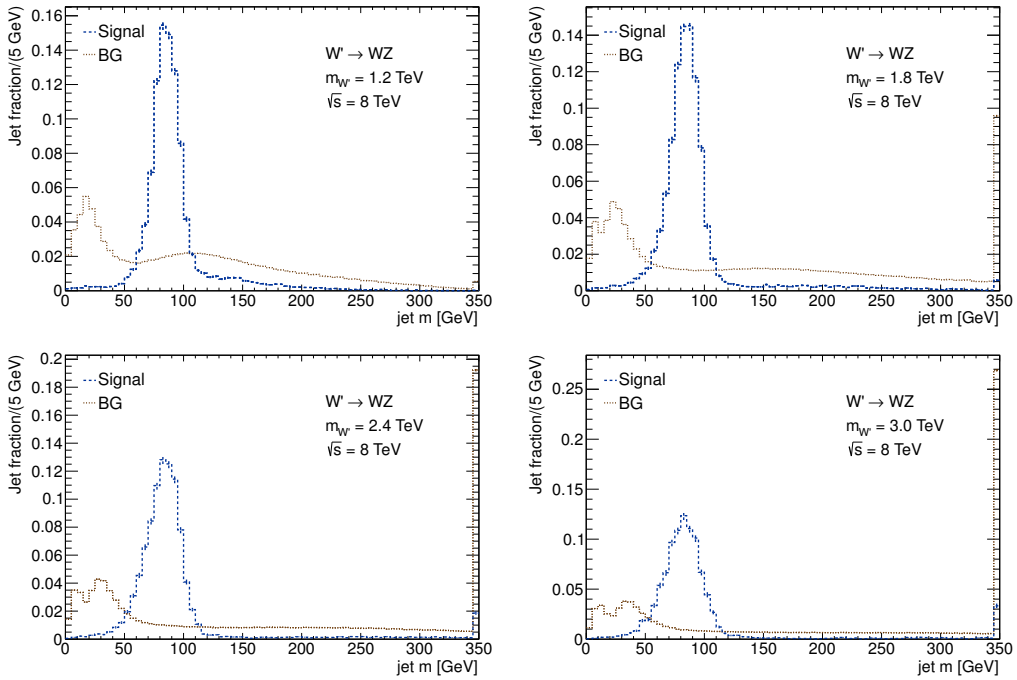

Figure 9.2.: Jet mass for the $W' \to WZ$ signal and Pythia multijet background for events with $(m_{12} - m_{W'})/m_{W'} < 10\%$ and $\Delta y_{12} < 1.2$. Both spectra are normalized to unity. Both leading and subleading jets are included.

difference between the leading and subleading jets $|\Delta y_{12}| < 1.2$ and for which the leading jet passes the momentum balance cut $\sqrt{y_f} > 0.45$. The jet mass distribution after different cuts on the number of ghost associated tracks is shown in Figure 9.5. In order to choose value of the cut this distribution was fitted using a polynomial function for the QCD background and a for the signal a pair of double crystal ball functions [70–72]

$$f_{CB}(x; p_0, p_1, p_2) = p_0 \begin{cases} A_l(B_l - \frac{x-p_1}{p_2})^{-n_l}, & \text{for } \frac{x-p_1}{p_2} < -\alpha \\ exp(-\frac{(x-p_1)^2}{2p_2^2}), & \text{for } -\alpha < \frac{x-p_1}{p_2} < \alpha \\ A_r(B_r - \frac{x-p_1}{p_2})^{-n_r}, & \text{for } \frac{x-p_1}{p_2} > \alpha \end{cases} \tag{9.2}$$

$$A = \left(\frac{n}{\alpha}\right)^n exp\left(-\frac{|\alpha|^2}{2}\right) \tag{9.3}$$

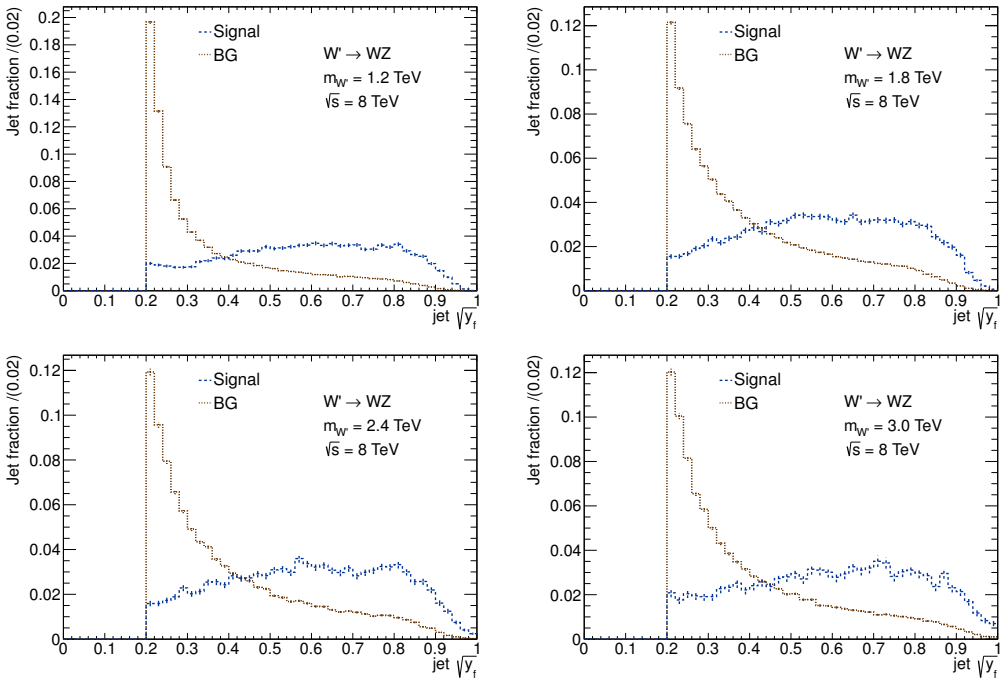

Figure 9.3.: Momentum balance for the $W' \to WZ$ signal and Pythia multijet background for events with $(m_{12} - m_{W'})/m_{W'} < 10\%$ and $\Delta y_{12} < 1.2$ plus the window on jet mass $60 \leq m < 110$ GeV. Both spectra are normalized to unity. Both leading and subleading jets are included.

$$B = \frac{n}{|\alpha|} - |\alpha| \tag{9.4}$$

For the crystal ball functions the ratio of the contributions from W and Z was fixed to the PYTHIA cross section prediction, given by the ratio of the p_0 values for the W and Z crystal ball functions. The ratio of the masses fixed according to their pole masses, given by the appropriate p_1 and the shape, which is adjusted by changing α_l, α_r, n_l, n_r fixed based on the shape obtained from the W' MC samples. The fit was done twice for each cut, first using a fourth degree polynomial for the QCD background and secondly using a third degree polynomial, but only in the mass range $40 < m < 140$ GeV. The cut at 30 was chosen because a sensitivity increase of 10-15% can be achieved while keeping a monotonically falling background spectrum.

The mass window used in the boson tag was adjusted to have two separate regions roughly centered on the nominal W and Z masses (80 and 91 GeV respectively). The window size was then optimised by maximising the statistical significance, which gave window sizes between 10 and 15 GeV for the different signal masses. To keep the

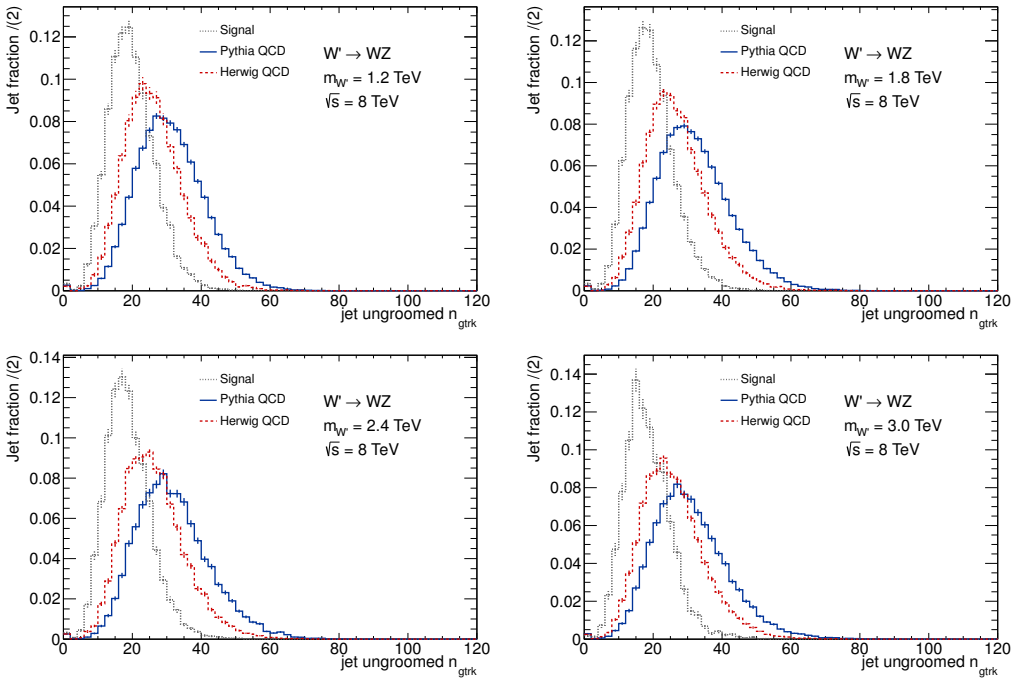

Figure 9.4.: Track multiplicity for the $W' \to WZ$ signal and Pythia and Herwig multijet backgrounds for events with $(m_{12} - m_{W'})/m_{W'} < 10\%$ and $\Delta y_{12} < 1.2$ plus the window on jet mass $60 \leq m < 110$ GeV and momentum balance threshold $y_{\mathrm{f}} \geq 0.45$. All spectra are normalized to unity. Both leading and subleading jets are included.

analysis simple a window size of 13 GeV was chosen for all signal masses, which does not lose much in significance for any of the signal masses compared to the optimum.

The dijet mass requirement, $m_{jj} > 1.0$ TeV, ensures that the trigger is 100% efficient. Lastly a veto on leptons and MET is also placed on the events to ensure that the selection is orthogonal to analyses in the fully- and semi-leptonic channels. The selection for this veto is described in Appendix B. The full event selection is summarised in Table 9.2.

The effect of applying each of these cuts in turn on the dijet mass spectrum in the background MC is shown in Figure 9.6 and for four different signal points in Figure 9.7, with the corresponding efficiencies as a function of the dijet mass also shown.

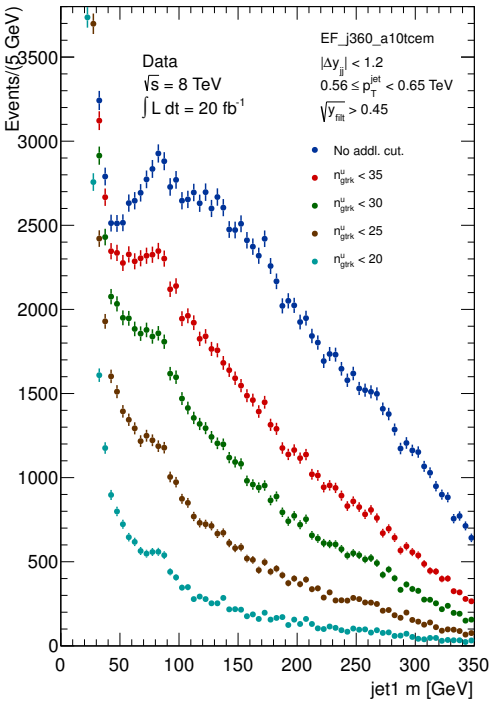

Figure 9.5.: Jet mass spectra for jets in with $0.56 < p_T < 0.65$ TeV, $|\Delta y_{12}| < 1.2$ and the boson tagging criteria $\sqrt{y_f} > 0.45$ applied to the leading jet for a series of thresholds on track multiplicity.

Table 9.2.: The event selection

TRG	Event passes EF_j360_a10tcem trigger
DQC	Event passes the data quality requirements
JET	Event has at least 2 C/A 1.2 jets
FIL	leading two jets survive split/filt process
CEN	$\|\Delta y_{12}\| < 1.2$
ETA	$\|\eta\| < 2.0$
BAL	$B < 0.15$
TAG	jets pass boson tag
TAGm	jets pass mass window selection
DJM	$m_{jj} > 1.1$ TeV

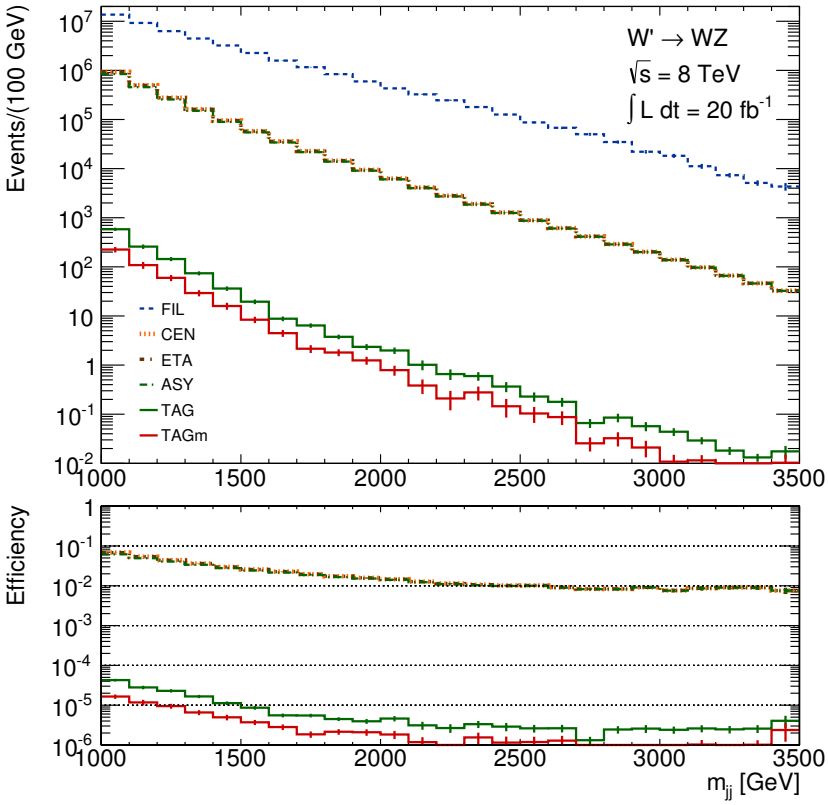

Figure 9.6.: Pythia QCD dijet mass spectrum at various levels of event selection as indicated in the legend and described in Table 9.2. Efficiency is with respect to the FIL selection.

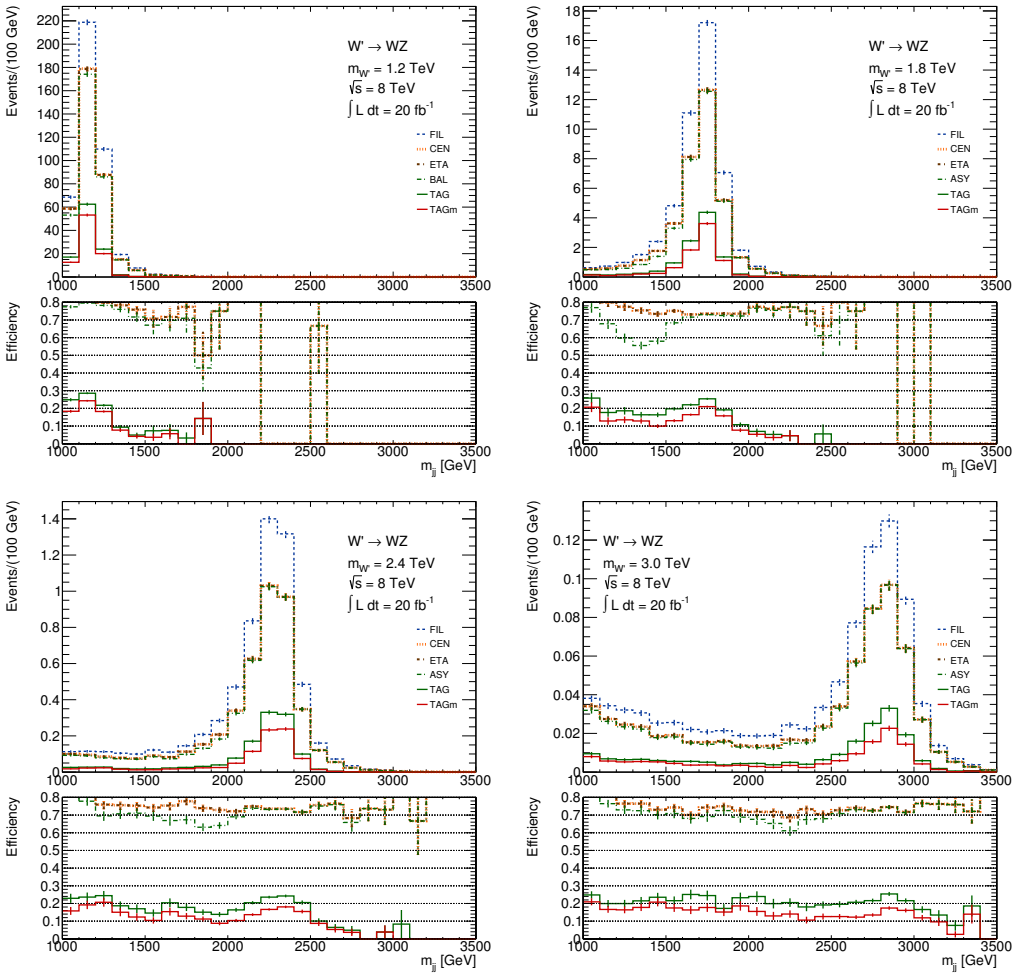

Figure 9.7.: $W' \to WZ$ dijet mass spectra using MC for the four reference values of W' mass at various levels of event selection as indicated in the legends.

9.5. Background Cross Checks

The mass distribution in data and background MC before the tagging cuts in Figure 9.8 shows the background MC doesn't perfectly model the data. Also, the number of ghost associated tracks disagrees between the different MC simulations. The QCD background distribution is extracted from the data, so the QCD MC is not used. However, it is still important to check that the cuts placed on the jets do not affect the shape of the background, such that the dijet mass function used to model it, and hence the limit set, is valid. To do this the efficiency of each of the boson tagging cuts was calculated and applied to a data driven background distribution to check for any distortion of the spectrum.

9.5.1. Efficiencies of the Boson Tagging Cuts

The efficiencies for all of the cuts were calculated for both the leading and the subleading jet from a sample with a single tagged boson for each of the cuts on n_{gtrk} and $\sqrt{y_f}$. The efficiency was calculated as a function of the jet p_T by simply taking the ratio of the number of jets passing the cut compared to those before the jet is made, for example to calculate the efficiency for the n_{gtrk} for the subleading jet the equation is

$$\mathrm{Eff}(n_{gtrk}^{jet2}) = \frac{n_{evt}(60 < m_{jet2} < 110\mathrm{GeV}, n_{gtrk}^{jet2} < 30)}{n_{evt}(60 < m_{jet2} < 110\mathrm{GeV})} \tag{9.5}$$

For both numerator and denominator the events are required to pass all the cuts that aren't part of the boson tagging. The plots of these efficiencies for both the leading and subleading jet, for the n_{gtrk} and $\sqrt{y_f}$ cuts are shown in Figure 9.9. It is worth noting that this is only considering the cuts in the boson tag and uses the wide mass window of $60 < m_{jet} < 110$ GeV.

The efficiency was also calculated for both of the boson tagging cuts after the other has already been applied, for example the efficiency of the cut on n_{gtrk} after the cut on $\sqrt{y_f}$ has already been applied to the jet, again for both the leading and subleading jets as a function of p_T. This was done using a similar formula as above,

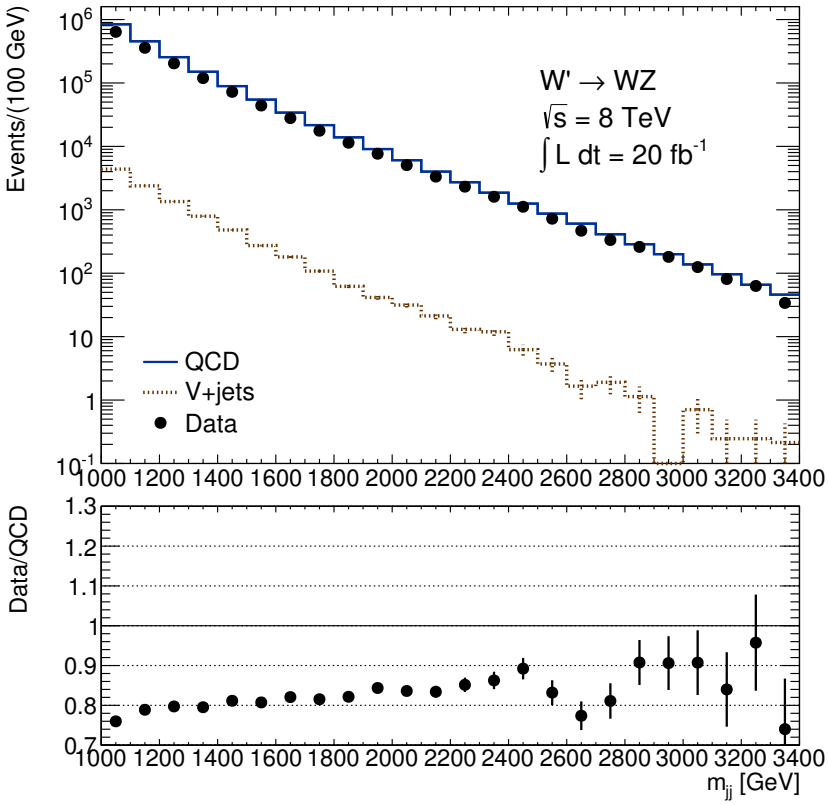

Figure 9.8.: Dijet mass distribution in data and background MC before boson tagging.

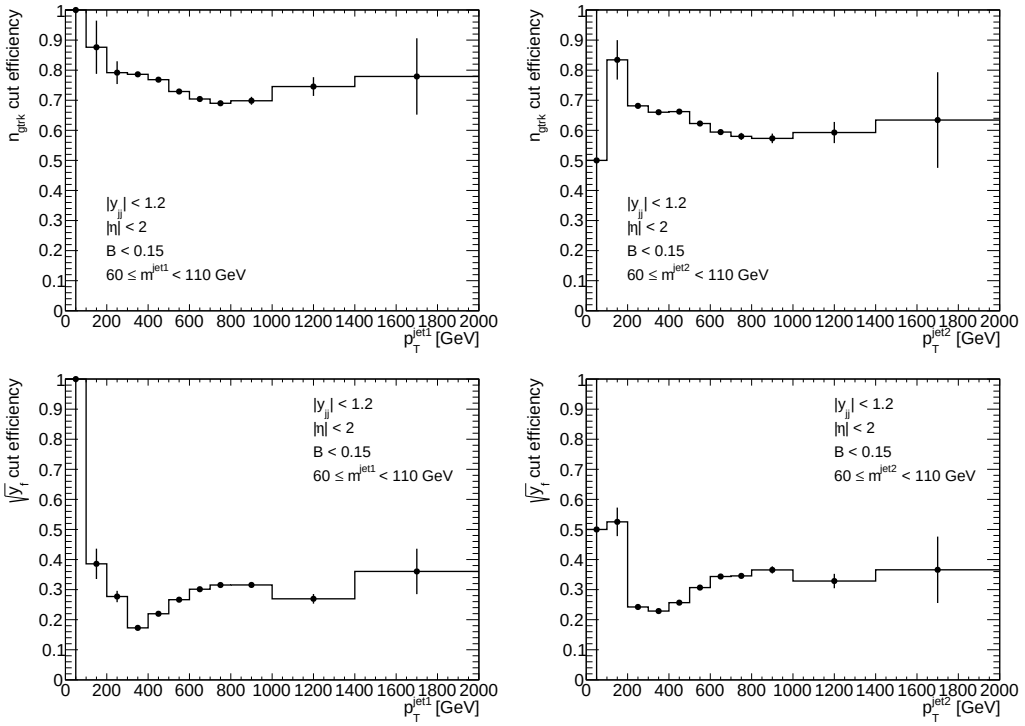

Figure 9.9.: The cut efficiencies for the cut on n_{gtrk} (top) and $\sqrt{y_f}$ (bottom) for the leading (left) and subleading (right) jets.

for example

$$\text{Eff}(n_{gtrk}^{jet2}|\sqrt{y_f^{jet2}} \geq 0.45) = \frac{n_{evt}(60 < m_{jet2} < 110GeV, \sqrt{y_f^{jet2}} \geq 0.45, n_{gtrk}^{jet2} < 30)}{n_{evt}(60 < m_{jet2} < 110GeV, \sqrt{y_f^{jet2}} \geq 0.45)} \tag{9.6}$$

gives the efficiency for jet 2 for the cut on n_{gtrk} after applying the cut on $\sqrt{y_f}$. These efficiencies are shown in Figure 9.10.

The efficiencies are not much affected by whether the other tagging cut has been applied or not, with the plots in the two figures showing very similar distributions. The shapes of the efficiencies as a function of p_T are similar for the two jets although the actual value is slightly different between the two. It is clear that the efficiency of the $\sqrt{y_f}$ cut is much lower than for the cut on n_{gtrk}.

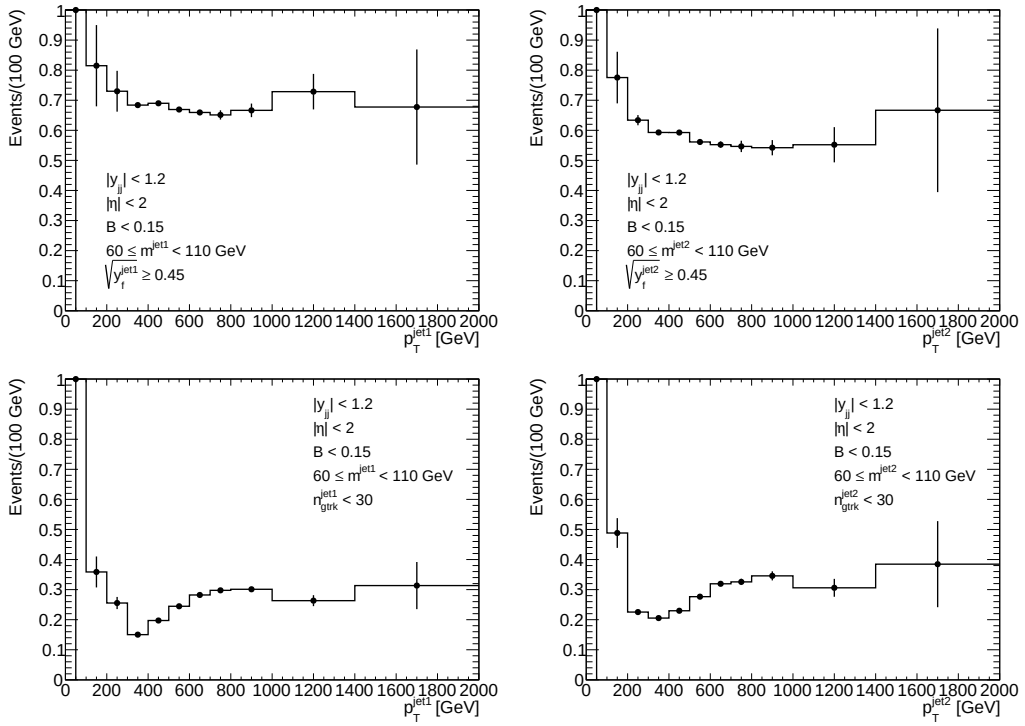

Figure 9.10.: The cut efficiencies for the cut on n_{gtrk} (top) and $\sqrt{y_f}$ (bottom), after the rest of the boson tagging cuts have been made, for the leading (left) and subleading (right) jets.

9.5.2. Applying the Cut Efficiencies to a Data Driven Background Estimate

A sample dijet mass distribution depleted of signal is produced by requiring that one jet passes the boson tagging cuts and the other is in the correct mass window but fails one of the other cuts. The efficiencies above are then applied to this to first generate the distribution after one and then both of the tagging cuts on the other jet are passed (the final selection, but still with the wide mass window). As an example the dijet mass distribution after the leading jet passes the tagging cuts and the subleading jet passes the mass cut but fails the cut on the number of associated ghost tracks (with no requirement on $\sqrt{y_f}$) is produced as a starting point. The efficiency is then applied to each event as a weight, depending on the jet p_T. First the inverse of the track efficiency is applied, then the track efficiency itself is applied, resulting in a total factor of $\text{Eff}(n_{gtrk}^{jet2})/(1 - \text{Eff}(n_{gtrk}^{jet2}))$. This produces the distribution after the leading jet passes the tagging cuts and the subleading jet passes all but the $\sqrt{y_f}$

cut. The $\sqrt{y_f}$ efficiency for the subleading jet is then applied to end up with the fully tagged distribution.

The plots showing the effect the efficiencies have on the distribution is shown in Figure 9.11. It can be seen from these that the background distribution essentially retains the same shape after the efficiencies are applied and the cuts shouldn't cause any distortion to the background distribution. However, at high dijet masses the number of events becomes small, and the fluctutations become large between bins.

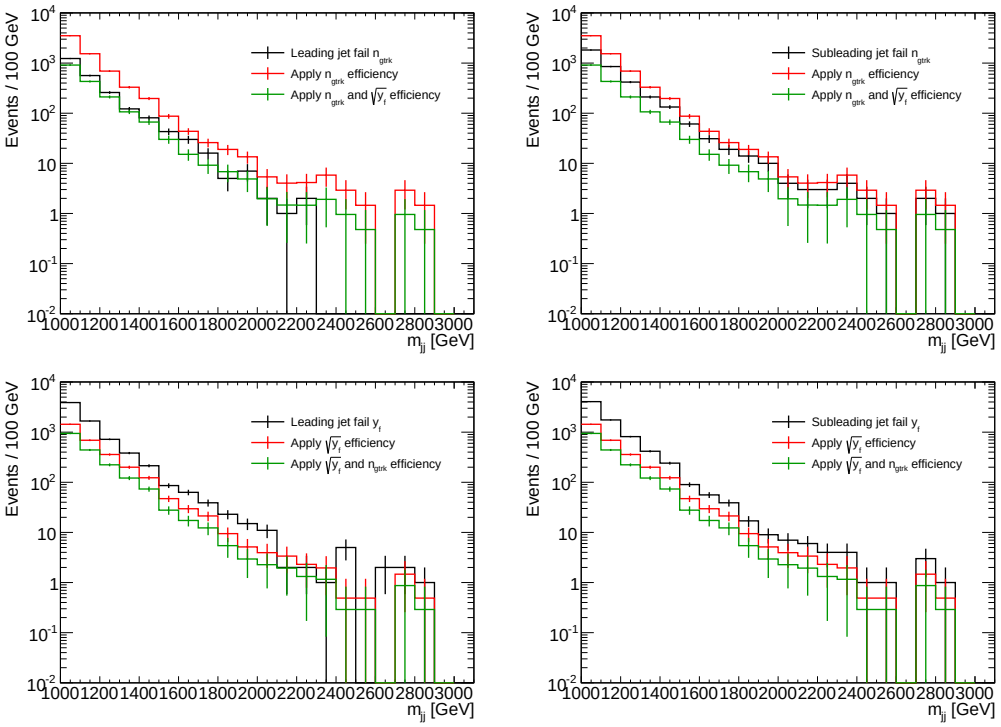

Figure 9.11.: The effect of applying the efficiencies, based on the jet p_T, to the depleted background mass distribution with the comparison to the cuts in the data in the case of first applying the track efficiency (top) and first applying the y_f efficiency (bottom) for the leading jet (left) and the subleading jet (right).

9.5.3. Applying the Cut Efficiencies to a Fitted Data Driven Background Estimate

As a further check, the starting background mass distribution with depleted signal content is fitted with the dijet function and this distribution is used as a starting

point to assess the impact of the cuts on the background distribution. In this case the information about the jet p_T is not available, so a plot of the dijet mass against each jet p_T is made and the average p_T for each dijet mass bin is used, as shown in Figure 9.12. Each bin in the distribution is then simply multiplied by the corresponding efficiency. The plots resulting from this are shown in Figure 9.13 and show that the fitted distribution remains smooth after the efficiencies are applied.

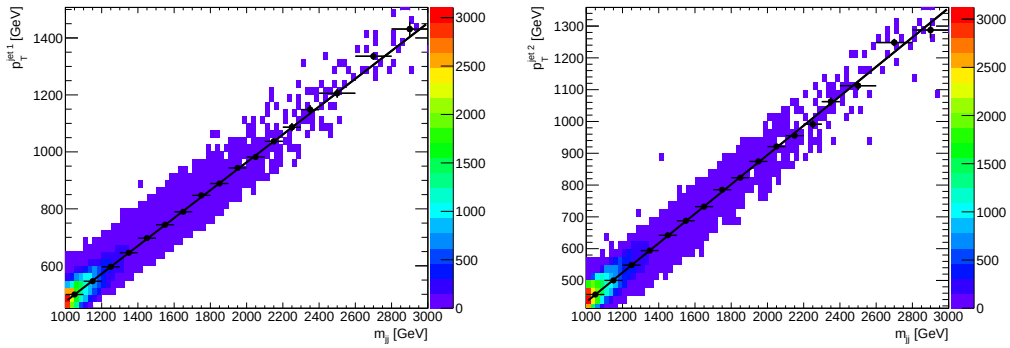

Figure 9.12.: A plot of the dijet mass against the jet p_T for the leading (left) and subleading (right) jets. The average value for each bin is shown and this distribution is fitted with a straight line.

The errors on these distributions due to the uncertainty on the efficiency and jet p_T are also assessed. For the efficiency uncertainty the dijet mass distributions are reproduced as detailed above, first using the efficiency value at the top of its error bar and second using the value at the bottom of its error bar. These distributions are then compared to the nominal distribution and the difference between them considered to be the error due to the efficiency. For the jet p_T uncertainty, the process above is repeated, but the p_T value used to calculate the efficiencies is that associated to first the lowest, and then the highest, dijet mass in the bin being considered, rather than the central value (as was done above). The appropriate p_T values are read off a fit to the m_{jj} against p_T distributions (shown in Figure 9.12). The resulting distributions are shown in Figure 9.14. Changing the p_T has no effect on most of the bins, as the bin the efficiency is taken from stays the same. Changing the efficiency has a larger effect, but is only really noticeable at the higher masses and even then remains small.

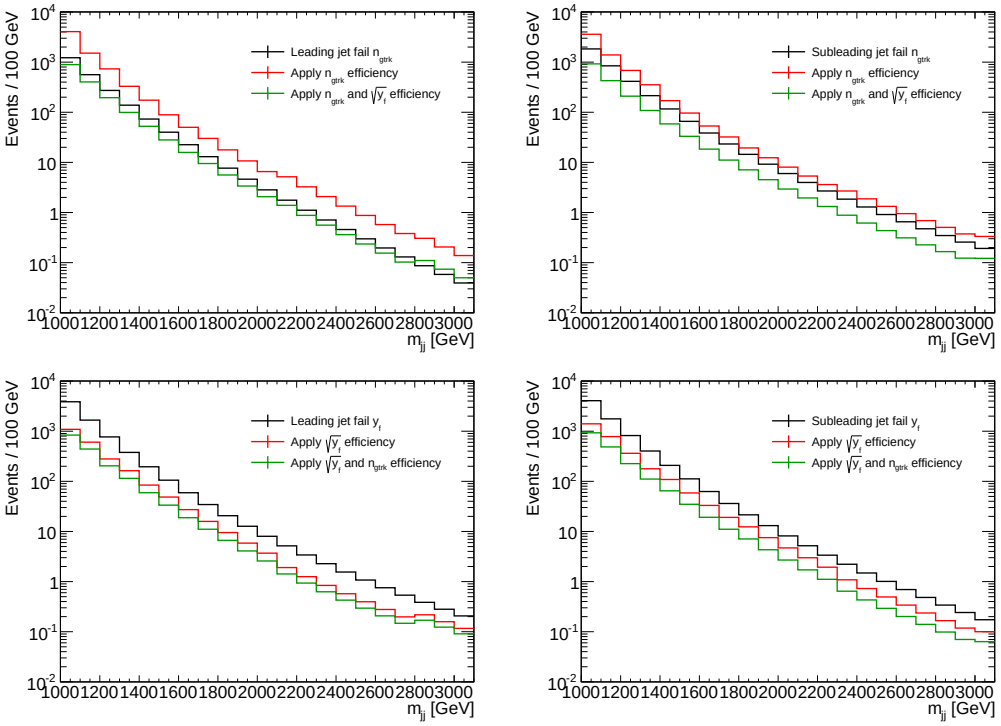

Figure 9.13.: The effect of applying the efficiencies, based on the average jet p_T for the dijet mass bin, to the fitted depleted background mass distribution with the comparison to the cuts in the data in the case of first applying the track efficiency (top) and first applying the y_f efficiency (bottom) for the leading jet (left) and the subleading jet (right).

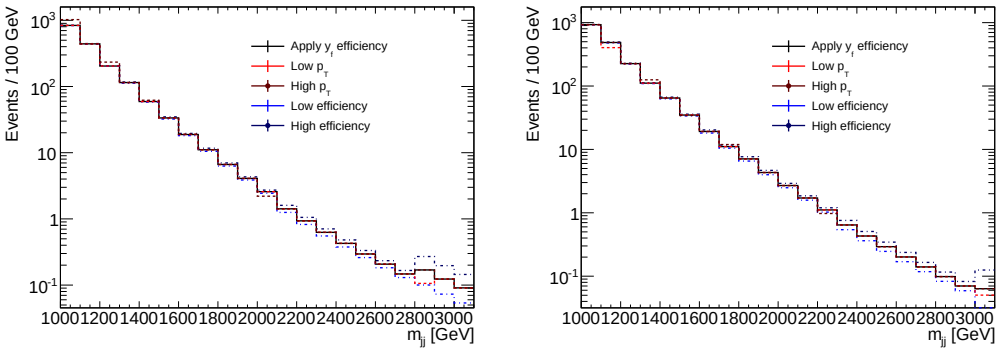

Figure 9.14.: The dijet mass distribution after applying the y_f and n_{gtrk} efficiencies to the fitted depleted background mass distribution (with the jet failing the y_f cut) along with the distributions for the upper and lower bounds of the jet p_T and efficiency.

9.6. Interpolation Between Signal Masses

In order to place limits at 100 GeV intervals, rather than the 200 GeV intervals that the available Monte Carlo samples permit, the signal samples were interpolated

between. The signal distributions obtained after the full selection, normalised using the cross section in the MC to the luminosity in the data (20 fb^{-1}) were taken. Each one was fitted with a single sided "crystal ball" function [70–72], as in equation 9.8 with an exponential to account for the low mass tail, caused by off-mass-shell production, which becomes more evident as the signal mass increases:

$$f_{fit}(x; p_0, p_1, p_2, p_3, p_4) = f_{CB}(x; p_0, p_1, p_2) + p_3 exp(-p_4 x), \tag{9.7}$$

where

$$f_{CB}(x; p_0, p_1, p_2) = p_0 \begin{cases} exp(-\frac{(x-p_1)^2}{2p_2^2}), & \text{for } \frac{x-p_1}{p_2} > -\alpha \\ A_r(B_r - \frac{x-p_1}{p_2})^{-n}, & \text{for } \frac{x-p_1}{p_2} < -\alpha \end{cases} \tag{9.8}$$

$$A = \left(\frac{n}{\alpha}\right)^n exp\left(-\frac{|\alpha|^2}{2}\right) \tag{9.9}$$

$$B = \frac{n}{|\alpha|} - |\alpha| \tag{9.10}$$

n, α and p_4 could be allowed to vary in the fit but in this case they were kept constant: $n = 3.2$, $\alpha = 0.9$, $p_5 = -0.001187$. The four parameters allowed to vary in the fit, p_0, p_1, p_2 and p_3 were found for each of the signal masses available and plotted as a function of the signal mass. The distributions obtained were then themselves fitted, as shown in Figure 9.15. The fit functions used were an exponential of a quadratic polynomial for p_0, a straight line for p_1 and p_2 and an exponential for p_3. The crystal ball parameters for the signal masses at 100 GeV intervals were derived from these fits were then used to produce signal histograms for the masses not provided by the Monte Carlo samples. This procedure was crossed checked by comparing the signal histograms produced this way to those taken straight from the Monte Carlo, as shown in Figure 9.16.

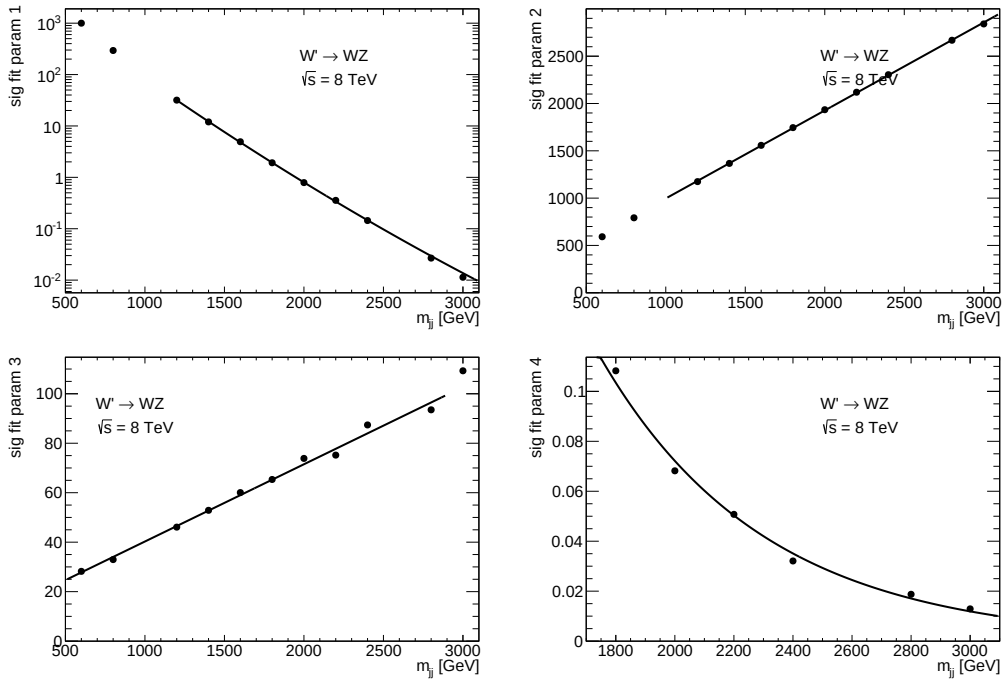

Figure 9.15.: The values of the fit parameters obtained as a function of the dijet mass of the MC signal sample used.

9.7. Statistical Analysis

The presence of a diboson resonance will appear as a peak on the smooth background dijet mass spectrum. A Bayesian analysis is performed on the data observed to determine whether such a peak is observed and to put limits on $W' \to WZ$ production in terms of a cross section times branching ratio, σB

The Bayesian analysis technique starts by calculating the likelihood of getting the observed number of events in data

$$\mathcal{L}(\mathbf{n}_{obs}|\mathbf{n}_{exp}) = \prod_i P_{pois}(n^i_{exp}, n^i_{obs}) \tag{9.11}$$

where $\mathbf{n}_{obs}$ is the number of events in data and $\mathbf{n}_{exp}$ is the number of events expected in each dijet mass bin, n^i_{exp} and n^i_{obs} are the number of events in dijet mass bin i, expected and observed respectively and P_{pois} is the Poisson probability

$$P_{pois}(\lambda, n) = \frac{\lambda^n e^{-\lambda}}{n!} \tag{9.12}$$

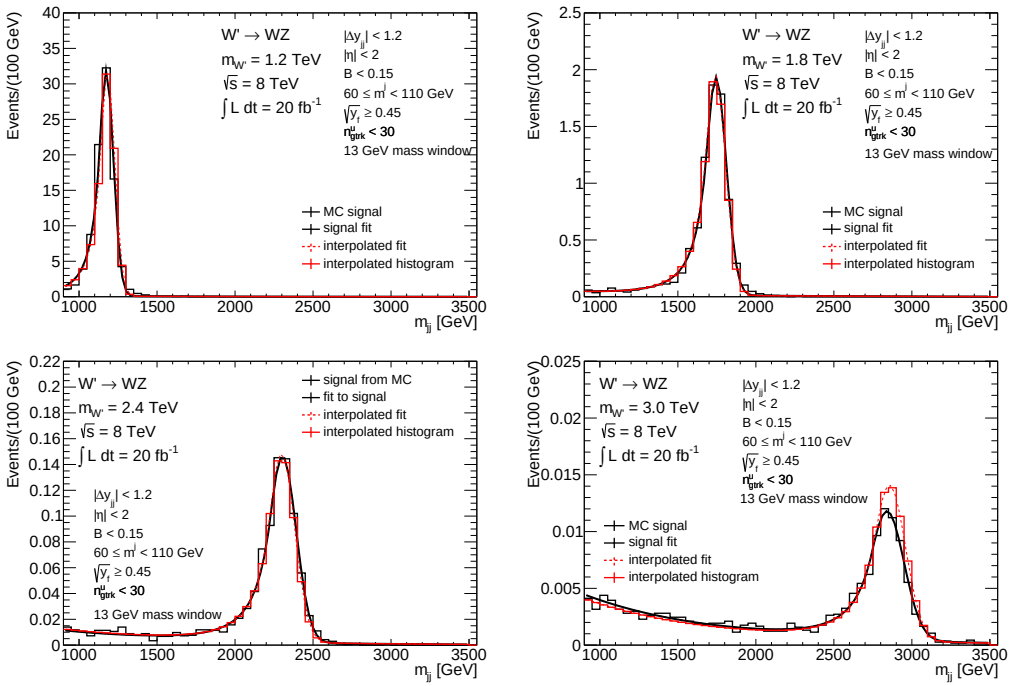

Figure 9.16.: The histograms from the signal MC and the corresponding fit with the interpolated fit and corresponding histogram for four signal masses.

In general, the expected number of events is calculated by adding the numbers of events expected in signal and background

$$\mathbf{n}_{exp} = \mathbf{n}_{sig} + \mathbf{n}_{bkg} \tag{9.13}$$

where the number of signal events is taken from the Monte Carlo with the signal strength allowed to vary

$$\mathbf{n}_{sig} = \mu \times \mathbf{n}_{SSM} \tag{9.14}$$

$\mathbf{n}_{SSM}$ is the expected number of events assuming SSM signal strength and μ is the signal strength, where 1 corresponds to the SSM prediction and 0 is the background only hypothesis, or the SM prediction. Several nuisance parameters are introduced to parameterise the background, $\mathbf{B}_{NP}$, and to account for the signal systematics, $\mathbf{S}_{NP}$, so the likelihood will also be dependent on these, as they are used to calculate $\mathbf{n}_{exp}$

$$\mathbf{T} = \{\mu, \mathbf{B}_{NP}, \mathbf{S}_{NP}\} \tag{9.15}$$

Hence the likelihood can be denoted by $\mathcal{L}(\mathbf{n}_{obs}|\mathbf{T})$. Based on this the posterior probability can be calculated using Bayes theorem

$$P_{post}(\mathbf{T}) = K\mathcal{L}(\mathbf{n}_{obs}|\mathbf{T})P_{prior}(\mathbf{T}) \tag{9.16}$$

This gives the posterior probability for a particular set of values of $\mathbf{T}$, where K is a normalisation factor introduced to ensure that the total probability when integrated over all the parameter values is equal to 1. The prior distributions are taken to be a product of independent priors for each of the parameters and are taken to be flat in the range in which it has a strong contribution to the posterior. What is actually of interest at the end is the probability of a certain signal strength, μ, which can be found by integrating over all the other parameters.

9.8. Background Parameterisation

The background is based on the dijet mass function [73], which has been shown to model dijet mass functions well in previous analyses, adjusted slightly to reduce the correlations between the parameters

$$\frac{dN}{dx} = C(1-x)^{p_2+p_9p_3}x^{p_3} \tag{9.17}$$

where $x = m_{jj}/p_5$ is dimensionless, Therefore, p_5 has dimensions of mass and is fixed to 8 TeV such that the function goes to zero at the kinematic limit and the function is valid in the range $0 < m_{jj} < p_5$. The constant, C, at the front is chosen to be

$$C = \frac{p_1}{(1-(p_6/p_5))^{p_2+p_9p_3}(p_6/p_5)^{p_3}} \tag{9.18}$$

such that $\frac{dN}{dx} = p_1$ at $m_{jj} = p_6$. The requirements $p_2 + p_9p_3 > 0$ and $p_3 < 0$ mean that this is a smoothly falling function from $x = 0$ to $x = 1$ (the kinematic limit) where it goes to zero. Here p_9 and p_6 are adjusted to remove the correlations between p_2 and p_3 and between p_1 and each of p_2 and p_3 respectively. The reduction in the correlations between the parameters caused by this slight modification to the formula means that fewer samples are required to gain the same numerical precision, without affecting the quality of the fit.

In order to evaluate the parameters of the fit the Bayesian analysis technique is used, fixing the signal strength to be 0. The parameters are input as priors and the initial distribution for p_1, p_2 and p_3 is taken to be flat in the range in which it has a strong contribution to the posterior. The Bayesian analysis then outputs posterior probability distributions for these parameters as described in the previous section and the median value of this distribution is taken to be the value of the parameter used for the fit.

The prior distributions and the resulting posterior distributions for each of the parameters are shown in Figure 9.17 and the fit to the dijet mass spectrum in data in Figure 9.18. The quality of the fit is also assessed statisically by calculating the p-value and z-value for each bin. The p-value is the probability that the fit value for the bin would give a value greater than the observed value, based on Poisson statistics. Alternatively the probability of a value greater than or equal to the observed value can be calculated, here the average of the two is used, hence the p-value tends to 0.5 for no observed events as the fit tends to zero. The z-value is the deviation of the data points from the fit in terms of σ for a gaussian distribution corresponding to the same p-value. The plots for these two quantities, for the fit to the data is shown in Figure 9.19.

An excess can be seen in these plots at about 2 TeV which has a corresponding statistical deviation of about 3.4σ at the maximum point. This excess is currently under further investigation to check that it is not caused by a detector effect or some aspect of the event selection cuts.

9.9. Systematic Uncertainties

The systematic uncertainties on the signal shape and normalisation are assessed and input as a probability density function to the statistical analysis. The systematics that only affect the normalisation are simply input as a scaling factor whereas the systematics that affect the shape need to be included at the point where the signal histogram is generated. Systematics due to the luminosity, the jet mass and energy scales and resolutions and each of the cuts being made are considered, as well as the uncertainties due to the Monte Carlo modelling.

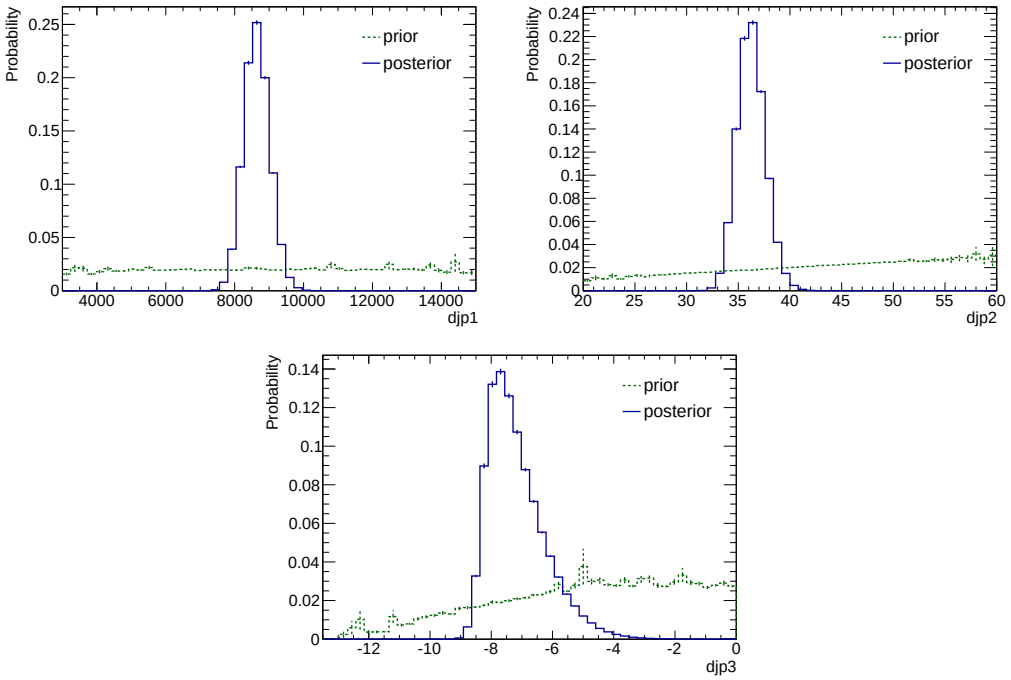

Figure 9.17.: The prior and posterior distributions for the three parameters varied in the background-only fit to the dijet mass spectrum in data after the full selection.

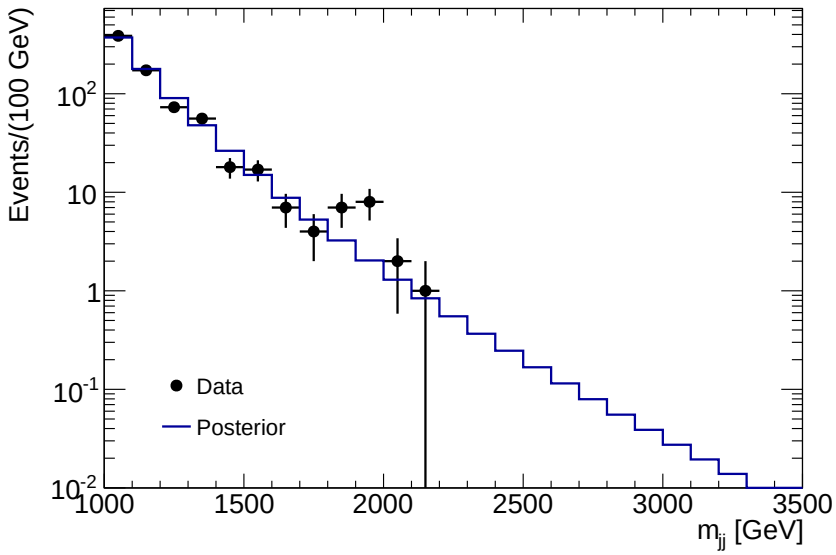

Figure 9.18.: The background-only fit (posterior) to the dijet mass spectrum in data after the full selection.

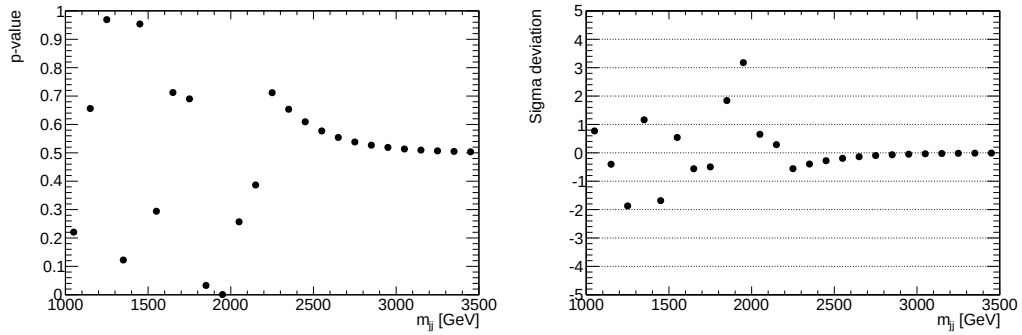

Figure 9.19.: The p-values and z-values corresponding to the background-only fit to the dijet mass spectrum in data after the full selection.

9.9.1. Luminosity Scale

The luminosity for the 2012 data is 20.3 fb^{-1} with an uncertainty of $\pm 2.8\%$. The uncertainty is calculated from the beam-separation scans carried out in November 2012 which were used for preliminary calibration of the luminosity scale [56].

The probability distribution function for the luminosity is taken to be a gaussian with a standard deviation of 0.028 corresponding to the error, scaled by the difference between the measured luminosity of $20.3 fb^{-1}$ and that assumed for the MC normalisation of $20 fb^{-1}$:

$$P(S_{int}) = 1.015 G(L_{int}|1, 0.028) \tag{9.19}$$

where $G(x|\bar{x}, \sigma)$ is the gaussian PDF

$$G(x|\bar{x}, \sigma) = \frac{1}{\sigma\sqrt{2\pi}} e^{-\frac{(x-\bar{x})^2}{2\sigma^2}} \tag{9.20}$$

9.9.2. Jet Energy Scale and Resolution

The jet energy scale is important because any shift in the p_T of a jet translates as a shift in the dijet mass. As the background is a steeply falling function a slight change in position of the peak can affect the number of expected background events by a large amount. The uncertainty is assessed by looking at the ratio between calorimeter and track jets [52, 69], in a similar way to that described for the previous analysis, in Section 8.5.3. The plot of this ratio for the calorimeter jets and the track

jet collection accounting for the track reconstruction is shown in Figure 9.20. From these plots the uncertainty of the p_T scale is taken to be 1 ± 0.02 and hence, as this directly translates to a shift in dijet mass the PDF for the uncertainty is

$$P(\alpha) = G(\alpha|1, 0.02) \tag{9.21}$$

The agreement between data and MC in the dijet p_T asymmetry is very good and so the jet energy resolution appears to be well modelled. Hence the Jet Energy Resolution uncertainty is neglected.

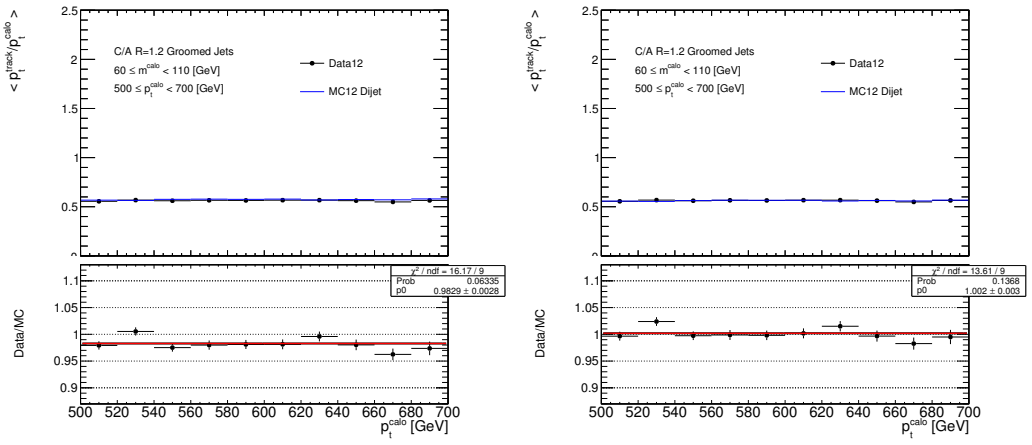

Figure 9.20.: Data-to-simulation track-to-calorimeter mean p_T double ratio as a function of calorimeter jet p_T for the standard simulation (left) and one accounting for the track reconstruction efficiency (right).

9.9.3. Jet Mass Scale and Resolution

The Jet Mass scale is also evaluated using calo-track ratios, as for the Jet Energy Resolution. The double ratio plots are shown in Figure 9.21 and from these a 3% uncertainty on the Jet Mass Scale is taken and the PDF used is

$$P(\alpha_m) = G(\alpha_m|1, 0.03) \tag{9.22}$$

This was cross checked by comparing data and MC in a singly boson tagged sample where a boson peak can be identified. This spectrum is produced by requiring one jet in the p_T region $560 < p_T < 650$ GeV (chosen to give the most clear signal peak) to pass the full boson tagging selection, as shown in Figure 9.22. From fits to the

extracted peak a scale uncertainty of 2% and a resolution uncertainty of 35% was found. The jet mass resolution is taken from this and so a gaussian PDF is used for the uncertainty

$$P(r_m) = G(r_m|0, 2.8\text{GeV}) \tag{9.23}$$

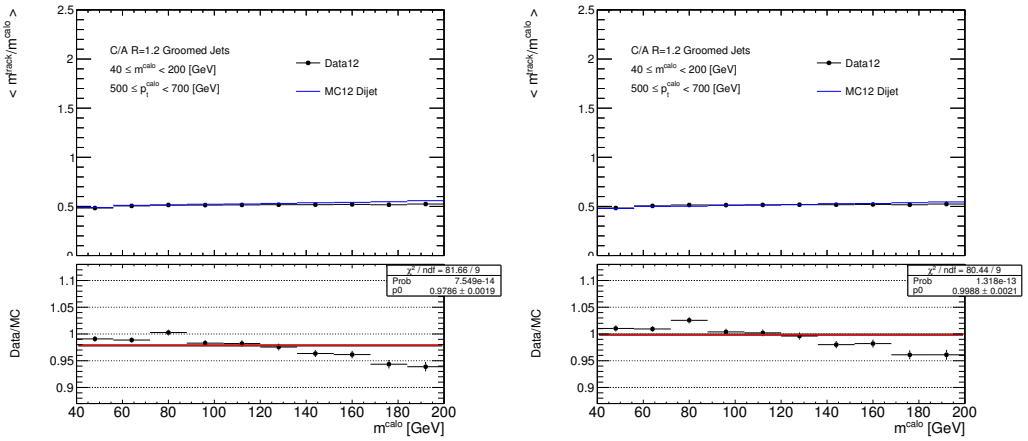

Figure 9.21.: Data-to-simulation track-to-calorimeter mean mass double ratio as a function of calorimeter jet mass for the standard simulation (left) and one where the tracking efficiency has been increased by its uncertainty (right).

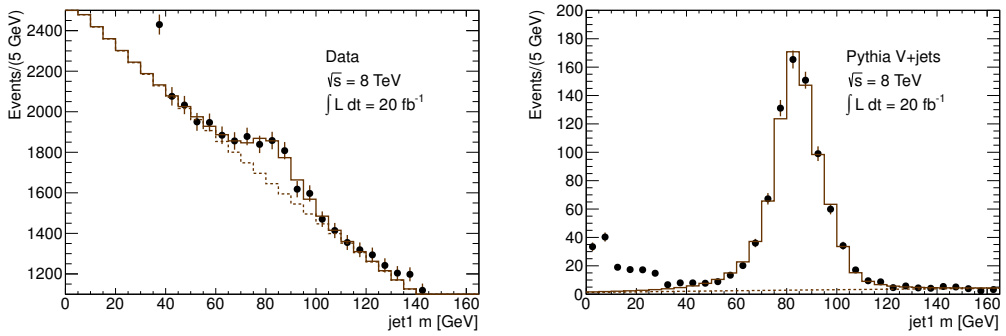

Figure 9.22.: Fits to the jet mass spectrum in V+jets events for data (left) and for simulation (right). Events are required to be accepted by the trigger EF_j360_a10tcem, have two leading jets within $|\eta| < 2.0$ and pass $|\Delta y_j j| < 1.2$. One jet in the event is required to pass the boson tag, $\sqrt{y_f} \geq 0.45$, and $n_{gtrk} < 30$. The p_T of the jets is required to be $0.56TeV < p_T < 0.65TeV$.

9.9.4. Momentum Balance Scale

The momentum balance, $\sqrt{y_f}$, is cut on in the boson tagging process and so its uncertainty must be taken into account. A slight change affects the signal efficiency and so is mostly a scale effect, however, the uncertainty is input as a shape uncertainty for simplicity. The uncertainty is once again calculated using calo-track ratios and the plots are shown in Figure 9.23. The uncertainty varies over the range of $\sqrt{y_f}$, but the uncertainty is taken from around the point of the cut, $\sqrt{y_f} = 0.45$, and based on the ratio plots an uncertainty of 2% is assigned with the pdf

$$P(\alpha_{\sqrt{y_f}}) = G(\alpha_{\sqrt{y_f}}|1, 0.02) \tag{9.24}$$

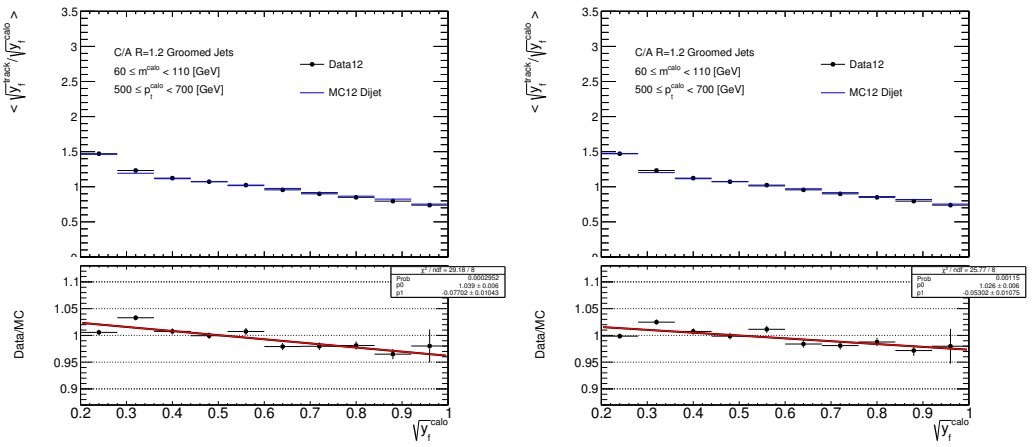

Figure 9.23.: Data-to-simulation track-to-calorimeter mean $\sqrt{y_f}$ double ratio as a function of calorimeter jet $\sqrt{y_f}$ for the standard simulation (left) and one where the tracking efficiency has been increased by its uncertainty. Both are after boson tagging.

9.9.5. Track Multiplicity Scale

As shown in Section 9.4, the track multiplicity is not well modelled in the MC so rather than evaluating the uncertainty using the calo-track ratios, as for the other variables, a data driven technique was used. The jet mass spectra with different values of the number of ghost tracks cut, produced to choose the cut value, in Figure 9.5, were used. These require the trigger to be passed and the leading jet to be in the range $560 \leq p_T < 650$ GeV and have $\sqrt{y_f} \geq 0.45$. The distributions were

fitted, as described in Section 9.4 using the Bayesian technique in the same way as the background fit. Taking the posterior distributions for the fits allows a probability distribution function for the efficiency to be obtained, weighting the contributions from the two fits equally, as shown in Figure 9.24. Comparing this efficiency to PYTHIA MC samples, the efficiency pdf can be scaled to give the scale factor pdf, which can be described by a truncated gaussian

$$G_t(x|x_0,\sigma_x,x_{max}) = \begin{cases} 0 & x < 0 \\ Ke^{-\frac{(x-x_0)^2}{2\sigma_x^2}} & 0 \leq x \leq x_{max} \\ 0 & x > x_{max} \end{cases} \tag{9.25}$$

with parameters $x_0 = 0.893$, $\sigma_x = 0.105$, $x_{max} = 1.056$.

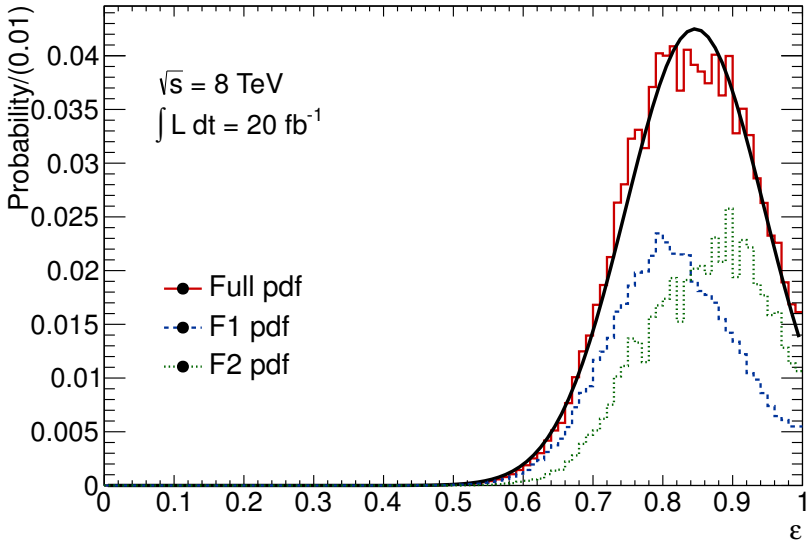

Figure 9.24.: Efficiency pdf for $n_{\text{gtrk}} < 30$.

9.9.6. Parton Shower Systematics

To calculate the systematics due to the parton shower model the signal efficiencies for signal MC samples generated with HERWIG and PYTHIA MCs were compared. The efficiencies after applying successive cuts through the cut flow were compared up to but not including the cut on the number of ghost associated tracks as it is known that the MC modelling of this is not good and the data driven technique is used

to estimate its uncertainty. Table 9.3 shows this signal efficiency cut flow for four different signal masses along with the absolute and fractional differences between the two, with the fractional difference calculated with respect to the PYTHIA sample. The largest difference between the two MC samples is about 4.6% seen for the 2.4 TeV signal mass and a normalisation systematic uncertainty is used with pdf

$$S_{ps} = G(S_{ps}|1, 0.05) \tag{9.26}$$

9.9.7. Summary of Systematic Uncertainties

The pdfs used for each of the sources of systematic uncertainty considered are summarised in Table 9.4. Combining all the scale uncertainties into one pdf produces a distribution with mean 0.794 and RMS 0.17 (21.4%) as shown in Figure 9.25. When the limits are calculated without systematics the mean is used to scale the distributions.

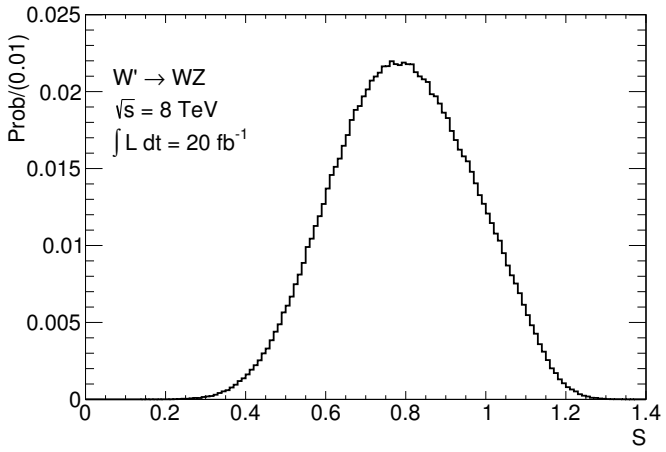

Figure 9.25.: The overall scale factor probability distribution function, after combining all the scale systematics.

Table 9.3.: The cutflow in terms of signal efficiency for the two signal Monte Carlo samples, Pythia and Herwig, along with the absolute and fractional differences between the two.

$m_{W'} = 1200$ GeV				
	pythia	herwig	difference	fractional difference
preselection	1.000	1.000	0.000	0.000
$\|\eta\| < 2.0$	0.948	0.947	0.001	0.001
$\|y_1 - y_2\| < 1.2$	0.709	0.717	-0.008	-0.012
A < 0.15	0.658	0.669	-0.010	-0.015
jet mass window	0.344	0.338	0.007	0.020
$\sqrt{y_f} \geq 0.45$	0.191	0.184	0.007	0.035

$m_{W'} = 1800$ GeV				
	pythia	herwig	difference	fractional difference
preselection	1.000	1.000	0.000	0.000
$\|\eta\| < 2.0$	0.961	0.959	0.002	0.002
$\|y_1 - y_2\| < 1.2$	0.713	0.719	-0.005	-0.007
A < 0.15	0.665	0.673	-0.008	-0.012
jet mass window	0.317	0.315	0.002	0.006
$\sqrt{y_f} \geq 0.45$	0.171	0.169	0.002	0.010

$m_{W'} = 2400$ GeV				
	pythia	herwig	difference	fractional difference
preselection	1.000	1.000	0.000	0.000
$\|\eta\| < 2.0$	0.949	0.945	0.004	0.004
$\|y_1 - y_2\| < 1.2$	0.715	0.711	0.003	0.005
A < 0.15	0.659	0.657	0.002	0.002
jet mass window	0.279	0.270	0.009	0.032
$\sqrt{y_f} \geq 0.45$	0.148	0.141	0.007	0.046

$m_{W'} = 3000$ GeV				
	pythia	herwig	difference	fractional difference
preselection	1.000	1.000	0.000	0.000
$\|\eta\| < 2.0$	0.913	0.907	0.005	0.006
$\|y_1 - y_2\| < 1.2$	0.693	0.683	0.010	0.014
A < 0.15	0.618	0.614	0.004	-0.006
jet mass window	0.249	0.240	0.010	0.039
$\sqrt{y_f} \geq 0.45$	0.134	0.128	0.006	0.046

Table 9.4.: Probability distribution functions used to vary the parameters to account for systematic uncertainties when carrying out the statistical analysis.

Param.	pdf	Meaning
μ	flat	Signal strength relative to SSM
p_1, p_2, p_3	flat	Background parameters
α	$G(\alpha \mid 1, 0.02)$	Jet p_T (m_{jj}) scale
S_{L}	$G(S_{\mathrm{L}} \mid 1, 0.028)$	Integrated luminosity SF
α_m	$G(\alpha_m \mid 1, 0.03)$	Jet mass scale
r_m	$G(r_m \mid 0, 2.8GeV)$	Jet mass resolution
α_y	$G(\alpha_y \mid 1, 0.02)$	Jet momentum balance ($\sqrt{y_{\mathrm{f}}}$) scale
S_{t}	$G_{\mathrm{t}}(S_{\mathrm{t}} \mid 0.893, 0.105, 1.056)$	Track multiplicity SF
S_{ps}	$G(S_{ps} \mid 1.0, 0.05)$	Parton Showering uncertainty SF

9.10. Limits

The limits are evaluated using the procedure described in Section 9.7 with the systematic probability distributions functions outlined in the previous section used as inputs. The resulting limit plot is shown in Figure 9.26, which shows that the limit falls outside the 2σ sensitivity band. It is worth stressing that there are currently many different cross checks being carried out and this result is liable to change.

9.11. Conclusions

A search for a diboson resonance in the all-hadronic channel has been presented, looking for resonances in the range 1 to 3 TeV. An excess in the dijet mass spectrum, corresponding to about 3.4σ local statistical significance, is seen at about 2 TeV. The excess is currently undergoing further checks to investigate potential detector or kinematic effects that could cause such a structure to appear. The events around the peak are also being considered in more detail by looking at events displays, like the one shown in Figure 9.27, and the distributions of the jets and their constituents [1] .

[1] As mentioned in the introduction the nature of working in a large collaboration is that analyses are performed in groups. In this analysis I must mention Attilio Picazio, Enrique Kajomovitz and David Adams especially for the huge amount of work done here

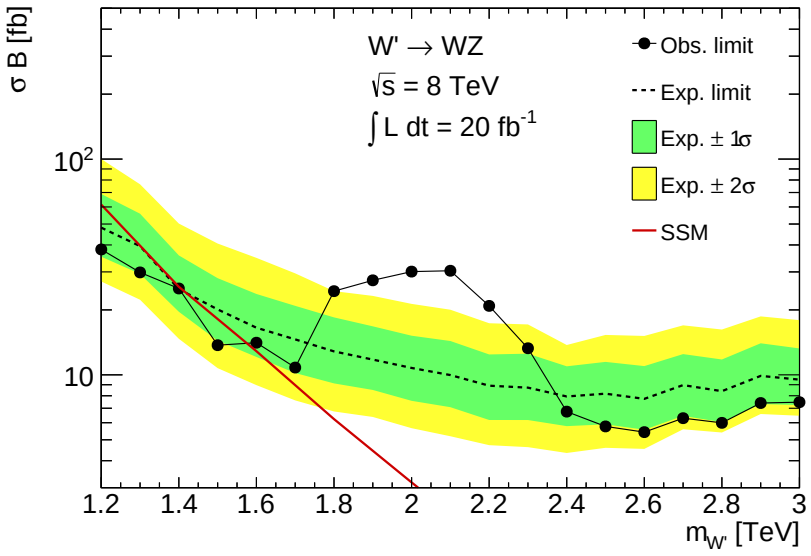

Figure 9.26.: The cross section limits based on the observed data after the full selection calculated using the Bayesian statistical analysis.

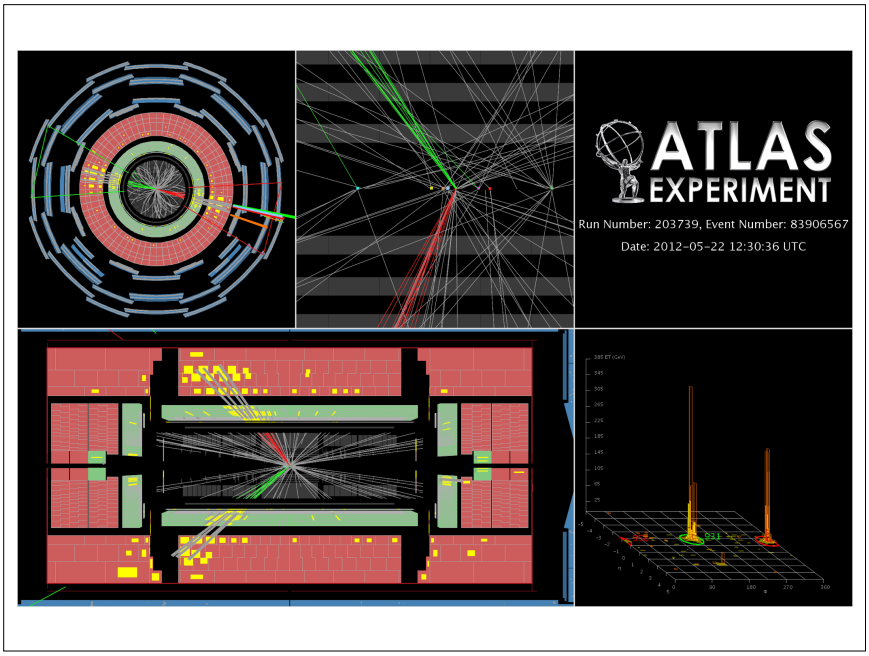

Figure 9.27.: An event display of one of the events passing all the analysis cuts with a dijet mass above 1.8 TeV.

Chapter 10.

Conclusions

The LHC provides a challenging environment to work in and becomes more and more difficult as the centre of mass energy, luminosity and levels of pileup rise. This makes fully hadronic decays of objects increasingly difficult to measure, however, it is useful to be able to exploit these channels as they accounts for 2/3 of W and Z boson decays. This thesis has shown that working in the very high p_T regime where both the decay products are contained within a single jet, it is possible to use these channels to make measurements and performs searches for new physics, relying on jet substructure techniques.

Firstly, some studies looking at the performance of the forward jet trigger in 2011 data were shown. The efficiency plots show the expected behaviour with the 100% efficiency points matching up at each level in the trigger. Applying calibration to the trigger level jets was then demonstrated to be able to offer an improvement in the trigger rates as well as being beneficial in bringing the trigger jets closer to those used in offline analyses. Subsequently calibration of the trigger jets was implement for 2012 running.

The observation of a hadronically decaying boosted W/Z boson was presented making use of a technique using jet shapes in the centre of mass frame. From this a cross section measurement was made, giving the result $\sigma(W^{\pm}/Z^0 \to qq : p_T > 320\text{GeV}, |\eta| < 1.9) = 8.34 \pm 0.78(\text{stat.}) \pm 1.47(\text{syst.})$ pb compared to the theoretical prediction from MCFM of $\sigma(W^{\pm}/Z^0 \to qq : p_T > 320\text{GeV}, |\eta| < 1.9) = 5.1 \pm 0.5\text{pb}$. The observed peak was used to investigate a variety of proposed jet grooming techniques which were assessed in terms of their agreement between data and MC, potential increases in signal to background ratios and the dependence on pileup. It

was seen that the data MC agreement was hardly affected by applying the grooming techniques but some improvement in the signal to background ratio could be made, although the significance remained the same. The most important result was the reduction in the pileup dependence that was clearly apparent for all the methods showing these techniques will become increasingly important with the future running of the machine.

This observation was a prerequisite to performing a search for potential heavy resonances decaying via W and Z bosons to hadronic final states. Such an analysis was described in Chapter 9 designed for a W' signal, although other particles such as a gravition could also be detected with this method. Although the analysis is ongoing, the limits at the time of writing are shown and an excess corresponding to about 3.4 σ is seen for a W' mass of about 2TeV. This is currently under further investigation.

Appendix A.

Systematic uncertainties on the boosted hadronically decaying W/Z boson cross section measurement

A.1. Systematic uncertainties on the signal yield

A.1.1. QCD shape distribution

The function used to model the QCD background in the analysis in Section 8 was validated using two control samples. The first is formed by selecting the jet with the smaller value of the likelihood in events which have more than one signal candidate jet. Studies based on MC show that selecting the jet with the higher value of the likelihood selects the correct signal candidate 98% of the time, hence selecting the smaller value of the likelihood produces a good control sample with very little signal contamination. This distribution is reweighted to account for the different p_T distribution. The QCD background function in equation 8.7 does a good job of fitting this distribution.

The second control sample is formed by placing a cut on the jet p_T balance, an event shape variable very weakly correlated with mass, defined as

$$\alpha = \frac{p_T^{bal}}{M^{dijet}} \tag{A.1}$$

where p_T^{bal} is the transverse momentum of the best balancing jet and M^{dijet} is the invariant mass of the jet-balancing jet system. Placing a cut on this produces a signal depleted sample without affecting the mass distribution. Placing a cut at $\alpha < 0.3$ leaves a signal to background ratio less than 1%. Once again the background PDF does a good job of fitting this shape.

A.1.2. JES Uncertainties

The JES scale was varied up and down by $\pm 1\sigma$ and the fit on data and MC repeated. All these distributions are well described by the background function used and produced a change in the signal yield of 5%. This is less than half of the statistical uncertainty and so is considered to be covered by this, given that the parameters of the fit are free to float. The signal reconstruction efficiencies are affected by this cut but this is considered to be covered because the pole mass is allowed to float and the cross section is determined using the fitted signal yields.

A.1.3. Jet mass scale

In the fit performed the pole masses of the bosons are fixed to the values found in the MC, but there may be a difference between data and MC so the fit is repeated with the pole mass free to float. When this is done a mass scale deviation of $m_s = (-0.45 \pm 0.86) GeV$ is observed, so there is no evidence for a difference between the data and MC in this quantity. This changes the signal yield by 0.86%, which is considered negligible. The fit is also repeated changing the pole mass to that plus and minus the statistical uncertainty on the mass scale. This results in a change in the signal yield of 2.2% and hence this is assigned as a systematic uncertainty due to the jet mass scale.

This uncertainty was studied as a function of the likelihood cut for values between 0.14 and 0.18, where lower cuts are not possible because the signal is too small compared to the background and higher cuts produce a background distribution for which the fit is not valid. The values found all lie within the systematic uncertainty assigned.

This was also checked using a different technique, plotting the double ratio of the mass calculated using calorimeter clusters and that using the tracks in data and MC. This produces an uncertainty of 4%, larger than the one found above. However, varying the mass scale by 4% causes the χ^2 probability falls to 1% suggesting that this uncertainty is too large.

A.1.4. Jet mass resolution

The mass resolution was evaluated using the truth jet information in the MC using the definition

$$m_R = \frac{m_{reco} - m_{truth}}{m_{truth}} \tag{A.2}$$

The difference in this quantity between different MC simulations gives an uncertainty of 4.5%. This was also evaluated using samples accounting for a difference in the amount of dead material in the detector and a different hadronic shower model (Fritiof fragmentation with the Bertini cascade) but the uncertainty from this is smaller than 1%.

The mass resolution uncertainty was cross checked by allowing the W and Z resolutions to vary by a common multiplicative factor, k_{width}. This was found to take the value $k_{width} = 1.063 \pm 0.14$ which results in a change in the signal yield of -9.5%. The large statistical uncertainty on this means it cannot be used as an accurate measure of the uncertainty but is a useful cross check.

This was also cross checked by making variations at the cluster level to account for three main effects. Firstly the dead material is accounted for by discarding low energy (E $<$ 2.5 GeV) clusters if $r \leq \mathcal{P}(E = 0)e^{-2E}$ when r is a random number between 0 and 1 and $\mathcal{P}$ is the probability a particle leaves a track and no energy in the calorimeter, which is measured to be 28% and E is the energy of the cluster. Secondly, the uncertainty on the position of the clusters is accounted for by smearing the values of η and ϕ of the clusters by a gaussian with an RMS of 5 mrad. Lastly the uncertainty on the cluster energy scale is accounted for by varying the transverse

momentum of the clusters up and down according to

$$p'_T = p_T \left[1 \pm 0.05 \left(1 + \frac{1.5GeV}{p_T}\right)\right] \tag{A.3}$$

Varying these things at the same time the analysis is redone and the jet mass resolution calculated resulting in a change of 4.6%

The mass resolution uncertainty is taken to be that from the initial calculation, summing the two contributions in quadrature to obtain a value of 4.7%. Varying the resolution of the signal by this amount results in a change in the signal yield of 12.6% which is taken to be the systematic uncertainty on the signal yield due to the mass resolution.

A.1.5. Signal Distribution

The uncertainty due to the signal probability distribution is evaluated using a toy MC study. A set of background events is generated using the background PDF based on the fit obtained from the data, with the number of events set to be that in data. The signal events are generated based on the signal MC. A fit is then performed on this distribution and this process is repeated 1000 times. The pull on the signal fraction and $W^{\pm}$ fraction is then plotted. This distribution has a width consistent with untiy, showing the statistical uncertainty is estimated correctly but the mean of the distribution is about 0.16 showing a slight bias, corresponding to a shift of 1.9% on the signal yield. The signal yield is corrected accordingly and this full correction assigned as a systematic uncertainty.

This is also repeated with only a background sample, which results in a mean value of the signal fraction centred on 0, showing that that background PDF cannot fake a signal. Lastly this is also repeated using the same background PDF but using signal PDFs generated from the different MC samples. The maximum variation in the signal yields produced by this is 2% which is assigned as an uncertainty due to signal PDF modelling.

A.1.6. QCD background PDF

The uncertainty due to the background PDF is calculated by changing the sigmoid function to a complimentary error function or a hyperbolic tangent and also by removing one of the exponential terms. The largest deviation in the signal yield produced by this is 8.79% which is taken as the uncertainty due to the background PDF.

A.1.7. $t\bar{t}$ background

The $t\bar{t}$ background is taken from the MC which is generated with a cross section $\sigma_{t\bar{t}} = 167^{+17}_{-18} pb$. The fit is repeated varying the cross section within its uncertainty which produces a shift of 1.34% in the signal yield which is taken as the uncertainty due to this background.

A.1.8. Single top background

The signal yield is corrected for the contribution expected from the single top background which is calculated based on the default values of the top cross section and results in an expected $186 \pm 7 \pm 12$ events where the first uncertainty is due to MC statistics and the second due to the cross section uncertainty.

A.1.9. Diboson background

The signal yield also needs to be corrected for the diboson background. In the case of WW, WZ and ZZ events the yield is calculated from MC samples. For $W\gamma$ and $Z\gamma$ the signal yields are calculated using the cross section calculated in MCFM and rescaling the W and Z yields according to the cross section ratio $\sigma(W\gamma)/\sigma(WZ)$ and $\sigma(Z\gamma)/\sigma(WZ)$ assuming the p_T distributions are similar. A 50% uncertainty is assigned for this process. This results in a total of 131 ± 21 $W^{\pm}$ events and 49 ± 8 Z events.

A.2. Systematic uncertainties on the cross section

The systematic uncertainties on the signal yield as calculated already are carried through to the cross section measurement. Several other sources of systematic uncertainty are also considered. Firstly the systematic on the calculated signal efficiency, which is calculated considering the data MC discrpancy, JES uncertainty and JER uncertainty and MC statistics. The data MC discrepancy is evaluated by calculating the efficiency based on the likelihood calculated from all the different MC simulations and taking the averaged variation which gives a 4.4% uncertainty. The calculation is also repeated varying the JES up and down and recalculating the signal efficiencies, producing a 3.6% systematic uncertainty. The jet energy resolution uncertainty is calculated by comparing the resolution in data and in simulated dijet events. The signal efficiency is then recalculated varying the energy resolution within this uncertainty, producing a change in the signal efficiency of about 0.3%. Lastly the finite size of the MC sample gives 0.57% and 0.55% relative systematics on the $W^{\pm}$ and Z^0 cross sections.

The uncertainties on the branching ratios are also taken into account. The values used are $Br(W^{\pm} \to q\bar{q}) = (67.60 \pm 0.27)\%$ and $Br(Z^0 \to q\bar{q}) = (69.91 \pm 0.06)\%$, which results in a systematic uncertainty of 0.4% and 0.1% on the measured cross section. There is also an uncertainty due to the fixing of the ratio between the W and Z ratios in the fit, varying this within the theoretical uncertainty produces a 2.9% uncertainty. Lastly the effect of the luminosity was considered which gives a 1.8% uncertainty. These are summarised in Table 8.5.

Appendix B.

Lepton Veto Requirements for the Diboson Resonance Search

ATLAS performs additional searches for heavy resonant states decaying to bosons in non-fully hadronic final states. To improve the sensitivity to these new resonant states it is possible to combine the results from all the different searches providing the analyses are orthogonal. To achieve this lepton and missing transverse momentum vetoes are placed on the data used in this search. The requirements for a veto muon are summarised in Table B.1 and the requirements for a veto electron in Table B.3.

Table B.1.: Muon veto requirements

staco combined muon, author 6
$p_T > 20GeV$
$\lvert\eta\rvert < 2.5$
pass ID track quality requirements (Table B.2)
$\frac{ptcone20}{p_T} < 0.15$
$\lvert z_0 sin\theta\rvert < 2.0mm$
$\left\lvert\frac{d_0}{\sigma(d_0)}\right\rvert < 3.5$
$\left\lvert\left(\frac{q}{p}\right)_{MS} - \left(\frac{q}{p}\right)_{ID}\right\rvert < 5\sigma$

Table B.2.: ID track quality requirements for the veto muon

number of B layer hits ≥ 1
number of pixel hits or crossed dead pixel sensors ≥ 1
number of SCT hits or crossed dead SCT sensors ≥ 5
number of pixel holes + number of SCT holes < 3
if $0.1 < \eta < 1.9$: $n_{TRT} \geq 6$ and $n_{TRT}^{outliers} < 0.9 n_{TRT}$
if $\eta \geq 1.9$ and $n_{TRT} \geq 6$: $n_{TRT}^{outliers} < 0.9 n_{TRT}$

Table B.3.: Electron veto requirements

author 1 or 3
medium++ quality requirement
$p_T > 20GeV$
$\lvert\eta\rvert < 2.47$ excluding the crack region: $1.37 < \lvert\eta\rvert < 1.52$
$\left\lvert \frac{d_0}{\sigma(d_0)} \right\rvert < 6$
$\lvert z_0 sin\theta \rvert < 2.0mm$
$\frac{etcone20}{E_T} < 0.15$

Colophon

This thesis was made in LaTeX 2_ε using the "hepthesis" class [74].

Bibliography

[1] M. Cacciari, G. P. Salam, and G. Soyez, *The anti-kt jet clustering algorithm*, JHEP **04** (2008) 063, arXiv:0802.1189 [hep-ph].

[2] CERN, *CERN's Accelerator Complex*, http://cds.cern.ch/record/1621583, 2013. OPEN-PHO-CHART-2013-001.

[3] ATLAS Collaboration, G. Aad et al., *The ATLAS Experiment at the CERN Large Hadron Collider*, J. Instrum. **3** (2008) S08003.

[4] ATLAS Collaboration, *Observation of a new particle in the search for the Standard Model Higgs boson with the ATLAS detector at the LHC*, Phys.Lett. **B716** (2012) 1–29, arXiv:1207.7214 [hep-ex].

[5] CMS Collaboration, *Observation of a new boson at a mass of 125 GeV with the CMS experiment at the LHC*, Phys.Lett. **B716** (2012) 30, arXiv:1207.7235 [hep-ex].

[6] V. N. Gribov and L. N. Lipatov, *Deep inelastic ep scattering in perturbation theory*, Sov. J. Nucl. Phys. **15** (1972) 438–450.

[7] G. Altarelli and G. Parisi, *Asymptotic Freedom in Parton Language*, Nucl. Phys. **B126** (1977) 298.

[8] Y. L. Dokshitzer, *Calculation of the Structure Functions for Deep Inelastic Scattering and e^+e^- Annihilation by Perturbation Theory in Quantum Chromodynamics*, Sov. Phys. JETP **46** (1977) 641–653.

[9] SLAC-MIT Collaboration Collaboration, G. Miller et al., *Inelastic Electron-Proton Scattering at Large Momentum Transfers and the Inelastic Structure Functions of the Proton*, Phys. Rev. **D5** (1972) 528.

[10] BCDMS Collaboration Collaboration, A. Benvenuti et al., *A High Statistics*

Measurement of the Proton Structure Functions from Deep Inelastic Muon Scattering at High Q^2, Phys. Lett. **B223** (1989) 485.

[11] H1 Collaboration Collaboration, G. Miller et al., *A Measurement of the Proton Structure Function*, Nucl. Phys. **B439** (1995) 471.

[12] G. P. Salam and G. Soyez, *A practical Seedless Infrared-Safe Cone jet algorithm*, JHEP **05** (2007) 086, `arXiv:0704.0292 [hep-ph]`.

[13] Y. Dokshitzer, G. Leder, S. Moretti, and B. Webber, *Better jet clustering algorithms*, JHEP **08** (1997) 001, `arXiv:9707323 [hep-ph]`.

[14] S. Catani, Y. L. Dokshitzer, M. H. Seymour, and B. R. Webber, *Longitudinally invariant K(t) clustering algorithms for hadron-hadron collisions*, Nucl. Phys. **B406** (1993) 187–224.

[15] P. W. Higgs, *Broken Symmetries and the masses of gauge bosons*, Phys.Rev.Lett **13** (1964) 508.

[16] F. Englert and R. Brout, *Broken Symmetries and the mass of gauge vector mesons*, Phys.Rev.Lett **13** (1964) 321.

[17] G. S. Guralnik, C. R. Hagen, and T. W. B. Kibble, *Global Conservation laws and massless particles*, Phys.Rev.Lett **13** (1964) 585.

[18] J. Wess and B. Zumino, *Supergauge transformations in four dimensions*, Nucl. Phys. **B70** (1974) 39.

[19] G. Altarelli, B. Mele, and M. Ruiz-Altaba, *Searching for new heavy vector bosons in $p\bar{p}$ colliders*, Z.Phys.C **45** (1989) 109.

[20] GEANT4 Collaboration, S. Agostinelli et al., *GEANT4: A simulation toolkit*, Nucl. Instrum. Meth. **A506** (2003) 250–303.

[21] T. Sjöstrand, S. Mrenna, and P. Z. Skands, *PYTHIA 6.4 Physics and Manual*, JHEP **0605** (2006) 026, `arXiv:0603175 [hep-ph]`.

[22] T. Sjöstrand, S. Mrenna, and P. Z. Skands, *A brief introduction to PYTHIA 8.1*, Comput.Phys.Commun. **178** (2008) 852–867, `arXiv:0719.3820 [hep-ph]`.

[23] T. Sjostrand, *PYTHIA 8 Status Report*, `arXiv:0809.0303 [hep-ph]`.

[24] G. Corcella et al., *HERWIG 6.5: an event generator for Hadron Emission Reactions With Interfering Gluons (including supersymmetric processes)*, JHEP **01** (2001) 010, arXiv:0011363 [hep-ph].

[25] M. Bahr et al., *Herwig++ Physics and Manual*, Eur. Phys. J. **C58** (2008) 639–707, arXiv:0803.0883 [hep-ph].

[26] P. Nason, *A new method for combining NLO QCD with shower Monte Carlo algorithms*, JHEP **11** (2004) 040, arXiv:0409146 [hep-ph].

[27] S. Frixione, P. Nason, and C. Oleari, *Matching NLO QCD computations with Parton Shower simulations: the POWHEG method*, JHEP **11** (2007) 070, arXiv:0709.2092 [hep-ph].

[28] S. Alioli, P. Nason, C. Oleari, and E. Re, *A general framework for implementing NLO calculations in shower Monte Carlo programs: the POWHEG BOX*, JHEP **1006** (2010) 043, arXiv:1002.2581 [hep-ph].

[29] P. Z. Skands, *Tuning Monte Carlo Generators: The Perugia Tunes*, Phys. Rev. **D82** (2010) 074018, arXiv:1005.3457 [hep-ph].

[30] ATLAS Collaboration, *Charged-particle multiplicities in pp interactions measured with the ATLAS detector at the LHC*, New J.Phys. **13** (2011) 053033, arXiv:1012.5104 [hep-ex].

[31] A. D. Martin, R. Roberts, W. J. Stirling, and R. Thorne, *Scheme dependence, leading order and higher twist studies of MRST partons*, Phys.Lett. **B443** (1998) 301–307, arXiv:hep-ph/9808371 [hep-ph].

[32] A. Sherstnev and R. Thorne, *Different PDF approximations useful for LO Monte Carlo generators*, arXiv:0807.2132 [hep-ph].

[33] A. D. Martin, W. J. Stirling, R. S. Thorne, and G. Watt, *Parton distributions for the LHC*, Eur. Phys. J. **C63** (2009) 189–285, arXiv:0901.0002 [hep-ph].

[34] ATLAS Collaboration, *ATLAS tunes of PYTHIA6 and PYTHIA8 for MC11*, Tech. Rep. ATL-PHYS-PUB-2011-009, CERN, Geneva, 2011.

[35] J. Pumplin, D. Stump, J. Huston, H. Lai, P. M. Nadolsky, et al., *New generation of parton distributions with uncertainties from global QCD analysis*, JHEP **0207** (2002) 012, arXiv:hep-ph/0201195 [hep-ph].

[36] J. M. Butterworth and J. R. Forshaw, *Photoproduction of multi-jet events at HERA*, J. Phys. **G19** (1993) 1657, 9601371.

[37] J. M. Butterworth, J. R. Forshaw, and M. H. Seymour, *Multiparton interactions in photoproduction at HERA*, Z. Phys. **C72** (1996) 637–646, arXiv:9601371 [hep-ph].

[38] O. S. Brüning et al., *LHC Design Report*, Tech. Rep. CERN-2004-003-V-1, CERN, Geneva, 2004.

[39] ATLAS Collaboration, W. Lampl et al., *Calorimeter Clustering Algorithms : Description and Performance*, Tech. Rep. ATL-COM-LARG-2008-002., CERN, Geneva, April, 2008.

[40] G. S. M. Cacciari and G. Soyez, *FastJet user manaual (for version 3.01)*, CERN-PH-TH/2011-297 (2011) . http://arxiv.org/abs/1111.6097.

[41] ATLAS Collaboration, *Single hadron response measurement and calorimeter jet energy scale uncertainty with the ATLAS detector at the LHC*, Eur.Phys.J. **C73** (2013) 2305, arXiv:1203.1302 [hep-ex].

[42] ATLAS Collaboration, *Jet energy scale and its systematic uncertainty in proton-proton collisions at $\sqrt{s} = 7$ TeV with ATLAS 2011 data*, ATLAS-CONF-2013-004, CERN, Geneva, 2013.

[43] ATLAS Collaboration, T. Barillari et al., *Local Hadronic Calibration*, Tech. Rep. ATL-LARG-PUB-2009-001-2. ATL-COM-LARG-2008-006. ATL-LARG-PUB-2009-001, CERN, Geneva, Jun, 2008.

[44] ATLAS Collaboration, *Data-Quality Requirements and Event Cleaning for Jets and Missing Transverse Energy Reconstruction with the ATLAS Detector in Proton-Proton Collisions at a Center of Mass Energy $\sqrt{s} = 7$ TeV*, Tech. Rep. ATLAS-CONF-2010-038, CERN, Geneva, 2010.

[45] J. Butterworth, B. Cox, and J. R. Forshaw, *WW scattering at the CERN LHC*, Phys.Rev. **D65** (2002) 096014, arXiv:hep-ph/0201098 [hep-ph].

[46] L. G. Almeida, S. J. Lee, G. Perez, G. F. Sterman, I. Sung, et al., *Substructure of high p_{T} Jets at the LHC*, Phys.Rev. **D79** (2009) 074017, arXiv:0807.0234 [hep-ph].

[47] S. D. Ellis, C. K. Vermilion, and J. R. Walsh, *Techniques for improved heavy particle searches with jet substructure*, Phys.Rev. **D80** (2009) 051501, arXiv:0903.5081 [hep-ph].

[48] A. Katz, M. Son, and B. Tweedie, *Jet Substructure and the Search for Neutral Spin-One Resonances in Electroweak Boson Channels*, JHEP **1103** (2011) 011, arXiv:1010.5253 [hep-ph].

[49] J. Thaler and K. Van Tilburg, *Identifying Boosted Objects with N-subjettiness*, JHEP **1103** (2011) 015, arXiv:1011.2268 [hep-ph].

[50] C. Chen, *New approach to identifying boosted hadronically-decaying particle using jet substructure in its center-of-mass frame*, Phys.Rev. **D85** (2012) 034007, arXiv:1112.2567 [hep-ph].

[51] ATLAS Collaboration, *Jet mass and substructure of inclusive jets in sqrt(s) = 7 TeV pp collisions with the ATLAS experiment*, arXiv:1203.4606 [hep-ex].

[52] ATLAS Collaboration Collaboration, G. Aad et al., *Performance of jet substructure techniques for large-R jets in proton-proton collisions at $\sqrt{s}$ = 7 TeV using the ATLAS detector*, JHEP **1309** (2013) 076, arXiv:1306.4945 [hep-ex].

[53] CMS Collaboration, *Search for anomalous $t\bar{t}$ production in the highly-boosted all-hadronic final state*, JHEP **1209** (2012) 029, arXiv:1204.2488 [hep-ex].

[54] ATLAS Collaboration, *Studies of the impact and mitigation of pile-up on large-R and groomed jets in ATLAS at $\sqrt{s}$ =7 TeV*, Tech. Rep. ATL-COM-CONF-2012-097., CERN, Geneva, July, 2012.

[55] J. M. Campbell and R. K. Ellis, *An Update on vector boson pair production at hadron colliders*, Phys.Rev. **D60** (1999) 113006, arXiv:hep-ph/9905386 [hep-ph].

[56] ATLAS Collaboration Collaboration, *Improved luminosity determination in pp collisions at $\sqrt{s} = 7$ TeV using the ATLAS detector at the LHC*, Eur.Phys.J. **C73** (2013) 2518, arXiv:1302.4393 [hep-ex].

[57] A. Abdesselam et al., *Boosted objects: a probe of beyond the standard model physics*, arXiv:hep-ph/1012.5412 [hep-ph].

[58] P. F. Harrison, H. R. Quinn, and *et al.*, *BaBar Physics Book*, SLAC-R504 (1998) .

[59] J. Bjorken and S. J. Brodsky, *Statistical Model for electron-Positron Annihilation Into Hadrons*, Phys.Rev. **D1** (1970) 1416–1420.

[60] S. Brandt, C. Peyrou, R. Sosnowski, and A. Wroblewski, *The Principal axis of jets. An Attempt to analyze high-energy collisions as two-body processes*, Phys.Lett. **12** (1964) 57–61.

[61] E. Farhi, *A QCD Test for Jets*, Phys.Rev.Lett. **39** (1977) 1587–1588.

[62] G. C. Fox and S. Wolfram, *Event Shapes in e+ e- Annihilation*, Nucl.Phys. **B149** (1979) 413.

[63] Particle Data Group Collaboration, J. Beringer et al., *Review of Particle Physics (RPP)*, Phys.Rev. **D86** (2012) 010001.

[64] J. M. Butterworth, A. R. Davison, M. Rubin, and G. P. Salam, *Jet substructure as a new Higgs search channel at the LHC*, Phys.Rev.Lett. **100** (2008) 242001, `arXiv:0802.2470 [hep-ph]`.

[65] S. D. Ellis, C. K. Vermilion, and J. R. Walsh, *Recombination Algorithms and Jet Substructure: Pruning as a Tool for Heavy Particle Searches*, Phys.Rev. **D81** (2010) 094023, `arXiv:0912.0033 [hep-ph]`.

[66] D. Krohn, J. Thaler, and L.-T. Wang, *Jet Trimming*, JHEP **1002** (2010) 084, `arXiv:0912.1342 [hep-ph]`.

[67] M. Cacciari and G. P. Salam, *Pileup subtraction using jet areas*, Physics Letters B **659** (2008) 119–126, `arXiv:0707.1378 [hep-ph]`.

[68] M. Cacciari, G. P. Salam, and G. Soyez, *The catchment area of jets*, JHEP **04** (2008) 005, `arXiv:0802.1188 [hep-ph]`.

[69] ATLAS, *Jet energy measurement with the ATLAS detector in proton-proton collisions at* $\sqrt{s} = 7\ TeV$, Eur. Phys. J. C **73** (2013) 2304, `arXiv:1112.6426`.

[70] M. J. Oreglia, *A study of the reactions* $\psi' \to \gamma\gamma\psi$*, Ph.D. dissertation*, SLAC-R-236 (1980) Appendix D. `http://www.slac.stanford.edu/pubs/slacreports/slac-r-236.html`.

[71] J. E. Gaiser, *Charmonium spectroscopy from the radiative decays of the J/ψ and ψ', Ph.D. dissertation*, SLAC-R-255 (1982) Appendix F. `http://www.slac.stanford.edu/cgi-wrap/getdoc/slac-r-255.pdf`.

[72] T. Swarnicki, *A study of the radiative cascade transitions between the Υ' and Υ resonances, Ph.D. dissertation*, DESY-F31-86-02 (1986) Appendix E. `http://inspirehep.net/record/230779/files/f31-86-02.pdf`.

[73] Robert M. Harris and Konstantinos Kousouris, *Searches for dijet resonances at hadron colliders*, Int. J. Mod. Phys. **A26** (2011) 5005–5055, `arXiv:1110.5302`.

[74] A. Buckley, *A class for typesetting academic theses*, 2010.